

AD-A105 197

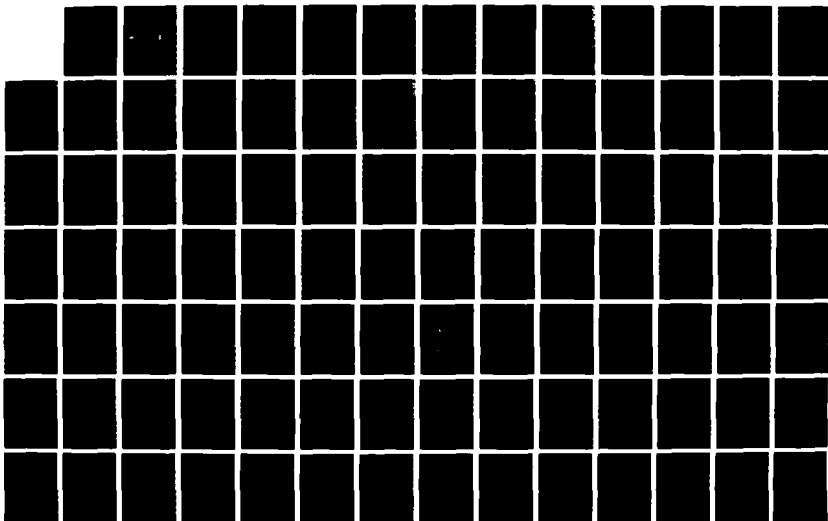
EXTREME ULTRAVIOLET BEAM-FOIL SPECTROSCOPY OF HIGHLY
IONIZED NEON AND ARGON(U) AIR FORCE WEAPONS LAB
KIRTLAND AFB NM J A DEMAREST JUN 87 AFML-TR-87-26

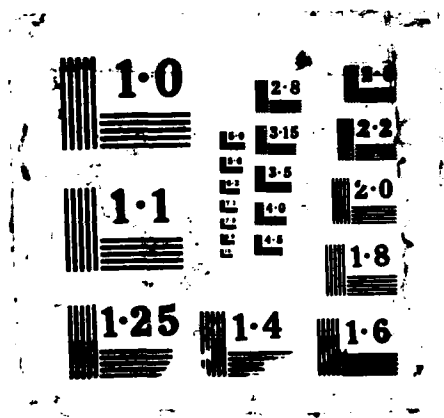
1/2

UNCLASSIFIED

F/G 20/7

NL





DTIC FILE COPY

2

AD-A185 197

**EXTREME ULTRAVIOLET BEAM-FOIL
SPECTROSCOPY OF HIGHLY IONIZED NEON
AND ARGON**

J. A. Demarest

June 1987

Final Report

DTIC
ELECTE
SEP 29 1987
S *ad* D

Approved for public release; distribution unlimited

AIR FORCE WEAPONS LABORATORY
Air Force Systems Command
Kirtland Air Force Base, NM 87117-6008

87 9 23 249

This final report was prepared by the Air Force Weapons Laboratory, Kirtland Air Force Base, New Mexico, under Job Order 57971901. Lieutenant Colonel John A. Demarest (AWP) was the Laboratory Project Officer-in-Charge.

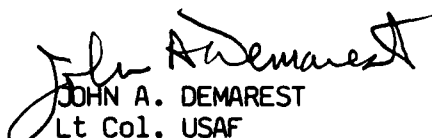
When Government drawings, specifications, or other data are used for any purpose other than in connection with a definitely Government-related procurement, the United States Government incurs no responsibility or any obligation whatsoever. The fact that the Government may have formulated or in any way supplied the said drawings, specifications, or other data, is not to be regarded by implication, or otherwise in any manner construed, as licensing the holder, or any other person or corporation; or as conveying any rights or permission to manufacture, use, or sell any patented invention that may in any way be related thereto.

This report has been authored by an employee of the United States Government. Accordingly, the United States Government retains a nonexclusive, royalty-free license to publish or reproduce the material contained herein, or allow others to do so, for the United States Government purposes.

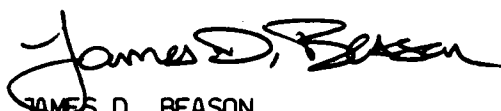
This report has been reviewed by the Public Affairs Office and is releasable to the National Technical Information Service (NTIS). At NTIS, it will be available to the general public, including foreign nationals.

If your address has changed, if you wish to be removed from our mailing list, or if your organization no longer employs the addressee, please notify AFWL/AWP, Kirtland AFB, NM 87117-6008 to help us maintain a current mailing list.

This report has been reviewed and is approved for publication.


JOHN A. DEMAREST
Lt Col, USAF
Project Officer

FOR THE COMMANDER


JAMES D. BEASON
Capt, USAF
Chief, Plasma Physics Branch


WILLIAM L. BAKER
Chief, Advanced Technology Division

DO NOT RETURN COPIES OF THIS REPORT UNLESS CONTRACTUAL OBLIGATIONS OR NOTICE ON A SPECIFIC DOCUMENT REQUIRES THAT IT BE RETURNED.

REPORT DOCUMENTATION PAGE

1a. REPORT SECURITY CLASSIFICATION Unclassified			1b. RESTRICTIVE MARKINGS		
2a. SECURITY CLASSIFICATION AUTHORITY			3. DISTRIBUTION / AVAILABILITY OF REPORT Approved for public release; distribution unlimited.		
2b. DECLASSIFICATION / DOWNGRADING SCHEDULE					
4. PERFORMING ORGANIZATION REPORT NUMBER(S) AFWL-TR-87-26			5. MONITORING ORGANIZATION REPORT NUMBER(S)		
6a. NAME OF PERFORMING ORGANIZATION Air Force Weapons Laboratory		6b. OFFICE SYMBOL (If applicable) AWP		7a. NAME OF MONITORING ORGANIZATION	
6c. ADDRESS (City, State, and ZIP Code) Kirtland AFB, NM 87117-6008			7b. ADDRESS (City, State, and ZIP Code)		
8a. NAME OF FUNDING / SPONSORING ORGANIZATION		8b. OFFICE SYMBOL (If applicable)		9. PROCUREMENT INSTRUMENT IDENTIFICATION NUMBER	
8c. ADDRESS (City, State, and ZIP Code)			10. SOURCE OF FUNDING NUMBERS		
			PROGRAM ELEMENT NO. 62601F	PROJECT NO. 5797	TASK NO. 19
			WORK UNIT ACCESSION NO. 01		
11. TITLE (Include Security Classification) EXTREME ULTRAVIOLET BEAM-FOIL SPECTROSCOPY OF HIGHLY IONIZED NEON AND ARGON					
12. PERSONAL AUTHOR(S) Demarest, J. A.					
13a. TYPE OF REPORT Final		13b. TIME COVERED FROM TO		14. DATE OF REPORT (Year, Month, Day) 1987, June	
				15. PAGE COUNT 190	
16. SUPPLEMENTARY NOTATION Dissertation					
17. COSATI CODES			18. SUBJECT TERMS (Continue on reverse if necessary and identify by block number)		
FIELD 20	GROUP 07	SUB-GROUP	extreme ultraviolet relative intensity calibration beam foil spectroscopy position-sensitive microchannel soft Xrays plate (over)		
19. ABSTRACT (Continue on reverse if necessary and identify by block number) A study of the extreme ultraviolet radiation emitted by ion beams of highly ionized neon and argon after passage through thin foils was conducted at the variable energy cyclotron at Texas A&M University. A grazing incidence spectrometer was equipped with a position sensitive microchannel plate (MCP) detector which improved the detection efficiency by two orders of magnitude. The position information of the MCP was determined to be linear over 90% of the 50-mm-wide detector. Spectra spanning regions of over 100 \AA were accumulated at a resolution of less than 1 \AA . A wavelength calibration based on a second-order equation of spectrometer position was found to result in an accuracy of $\pm 0.1 \text{\AA}$. Over 40 transitions of Ne VIII, Ne IX, and Ne X were observed in the wavelength region from 350-30 \AA from n=2-3,4,5; n=3-4,5,6,7,8; n=4-6,7; and n=5-9. An intensity calibration of the detection system allowed the determination of the relative populations of n=3 states of (over)					
20. DISTRIBUTION / AVAILABILITY OF ABSTRACT <input checked="" type="checkbox"/> UNCLASSIFIED/UNLIMITED <input type="checkbox"/> SAME AS RPT <input type="checkbox"/> DTIC USERS			21. ABSTRACT SECURITY CLASSIFICATION Unclassified		
22a. NAME OF RESPONSIBLE INDIVIDUAL Lt Col John A. Demarest			22b. TELEPHONE (Include Area Code) (505) 844-8616		22c. OFFICE SYMBOL AWP

19. ABSTRACT (Continued)

Ne VIII and Ne IX. An overpopulation of states with low orbital angular momenta support electron capture predictions by the first-order Born approximation.

The argon beam-foil data confirmed the wavelength predictions of 30 previously unobserved transitions in the wavelength region from 355 to 25 Å from $n=2-2$; $n=3-4$; $n=4-5,6,7$; $n=5-6,7$; and $n=6-8$. Lifetime determinations were made by the simultaneous measurement of 26 argon lines in the spectral region from 295-180 Å. Many of the $n=2-2$ transitions agreed well with theory.

18. SUBJECT TERMS (Continued)

two- and three-electron neon

three-, four-, and five-electron argon

Accession For	
NTIS CRA&I	<input checked="checked" type="checkbox"/>
DTIC TAB	<input type="checkbox"/>
Unannounced	<input type="checkbox"/>
Justification	
By	
Distribution/	
Availability Codes	
Dist	Avail and/or Special
A-1	



ACKNOWLEDGMENTS

I wish to acknowledge the guidance and support of the many individuals without whose help this research and dissertation would not have been possible.

I would like to express my sincere appreciation to Dr. Rand L. Watson for introducing me into the international community of atomic physicists and for providing me the opportunity to undertake a most challenging research project. His patience and insight helped me overcome many experimental obstacles.

My research colleagues, Dr. Josef Palinkas, Rick Maurer, Bryan Bandong, and Cathy Fulton, deserve special thanks for their help with experiments and computational support.

Thanks are also due to the cyclotron staff. I am indebted to Larry St. John for his assistance in electronic fabrication, to Walter Chapman for his influence in building much experimental hardware, and to Ranell Williams for printing the final draft of this document.

I appreciate the help of the following researchers from other laboratories: Dr. Brant Johnson for the timely loan of a channeltron detector, Dr. A. E. Livingston for the copy of his lifetime program, and Dr. E. Trabert for his guidance on grazing incidence spectroscopy. I owe the greatest debt to my wife, Teddy, and my children, Tina and Stephen, for bearing with me throughout my doctoral program.

TABLE OF CONTENTS

CHAPTER		Page
I	INTRODUCTION.....	1
	A. Background.....	1
	B. Features of Grazing Incidence Spectroscopy.	4
	C. Introduction to Beam-foil Spectroscopy....	6
	D. Foil Effects.....	9
	E. Doppler Effects.....	11
	F. Ion-Beam Charge State Considerations.....	13
	G. Beam-foil Method.....	15
	H. Related Research.....	20
II	EXPERIMENTAL METHODS.....	24
	A. Operating Principles for Grazing Incidence Spectroscopy.....	24
	B. Spectrometer System Adaptation.....	38
	C. Soft X-Ray Source.....	39
	D. Vacuum System.....	41
	E. Detectors -- Proportional Counter.....	44
	F. Detectors -- Channel Electron Multiplier (CEM).....	45
	G. Detectors -- Position Sensitive Microchannel Plate (MCP).....	49
III	ONE-, TWO-, AND THREE- ELECTRON NEON EUV MEASUREMENTS.....	72
	A. Background.....	72
	B. Comparison of Spectra Obtained with Channeltron and Microchannel Plate Detectors.....	73
	C. Neon Line Identification.....	81
	D. Neon Lifetime Measurements.....	89
	1. General considerations.....	89
	2. Sources of error.....	90
	3. Lifetimes of excited states of 40 MeV neon from 109 to 65 Å.....	91
	4. Discussion of results for carbon-foil-excitation.....	93
	E. Characteristics of Spectra Obtained with Other Exciter Foils.....	97
	1. Background.....	97
	2. Comparison of Spectra Taken Immediately Behind the Foil.....	98
	3. Foil effects on the cascade population of n=2-3 Li-, He- and H-like neon.....	101

CHAPTER		Page
	F. Spectrometer Relative Efficiency Determination.....	103
	G. Relative Populations of n=2-3 Li- and He-Like Neon.....	108
IV	EUV MEASUREMENTS OF 80 MEV ARGON.....	113
	A. Isoelectronic Trends.....	113
	B. Comparison of Argon Spectra Obtained with the Channeltron and Microchannel Plate..	115
	C. Argon Line Identification.....	118
	D. Lifetimes of Transitions in the 292 to 185 Å region.....	133
	E. Discussion of Lifetime Results.....	138
V	CONCLUSION.....	143
	A. Characterization of the Performance of a Position Sensitive Microchannel Plate in the EUV.....	143
	B. Beam-foil Study of Few-electron Neon Ions.....	145
	C. Beam-foil Study of Few-electron Argon Ions.....	147
	D. Possible Future Developments.....	148
	REFERENCES.....	149
	APPENDIX.....	155
	VITA.....	175

LIST OF TABLES

TABLE	Page
1. Foil scattering effects.....	11
2. Average beam charge and distribution widths.....	14
3. Vacuum ultraviolet beam-foil studies of neon at less than 1000 Å.....	20
4. Vacuum ultraviolet beam-foil studies of argon at less than 1000 Å.....	21
5. Optimum width for a 1-meter radius 1200 l/mm grating.....	28
6. Plate factor and reciprocal dispersion.....	30
7. Resolving powers for 1200 l/mm and 133.6 l/mm gratings.....	32
8. Comparison of theoretical and experimental resolution.....	33
9. Soft x-ray lines, spectrometer positions, wavelengths, energies, and widths measured with 100 μ m slits.....	41
10. Outgassing rates for vacuum system components.....	43
11. Wavelength range (+/-) for values of X and angle 2.....	62
12. Sensitivity of the MCP angle at spectrometer position X=5.200 and 100 μ m slit.....	66
13. 40 MeV Ne VIII line assignments.....	82
14. 40 MeV Ne IX line assignments.....	83
15. 40 MeV Ne X line assignments.....	84
16. New identifications in Ne IX.....	87
17. Sources of error in beam-foil lifetime measurements.....	90
18. Lifetimes of excited states of Ne VIII, Ne IX and Ne X.....	92
19. Replenishment ratios for carbon, silver and gold excited neon.....	102
20. Transition pairs used for a relative efficiency calibration.....	108
21. 80 MeV Ar XIII line assignments.....	121

TABLE	Page
22. 80 MeV Ar XIV line assignments.....	122
23. 80 MeV Ar XV line assignments.....	123
24. 80 MeV Ar XVI line assignments.....	125
25. Comparison of experimental and theoretical wavelengths (Å) for n=2-2 Ar XVI and Ar XV.....	130
26. Observed line blends in the 295-185 Å region.....	131
27. Unassigned lines in 80 MeV Ar.....	132
28. Lifetimes of Ar XVI, Ar XV, and Ar XIV.....	135
29. Comparison of selected Ar XV and Ar XIV experimentally determined branching ratios with theoretical values.....	139

LIST OF FIGURES

FIGURE	Page
1. Spectral region spanning the vacuum ultraviolet to x-rays.....	3
2. Beam-foil geometry. The grating size and angles ϕ and θ are exaggerated for illustration.....	7
3. Examples of decay schemes.....	18
4. Grazing incidence geometry.....	25
5. Spectral region sampled by the Minuteman 310GM spectrometer with a 3° grazing angle of incidence and a 1200 l/mm grating.....	27
6. Plate factor (dashed line) and reciprocal dispersion (circles) in Å/mil versus the spectrometer position in inches for the 1200 l/mm grating.....	31
7. Soft x-ray spectrum of solid LiF obtained with a 1200 l/mm grating, channel electron multiplier detector, and 100 micron slit widths.....	36
8. Soft x-ray spectrum of solid carbon obtained with a 133.6 l/mm grating, channel electron multiplier detector, and 100 micron slit widths.....	37
9. Top and aft views of the in-beam grazing incidence spectrometer system.....	40
10. Schematic diagram of the electronic configuration for the channel electron multiplier (channeltron) detector.....	47
11. Cut-away view of the microchannel plate detector on a sliding mount above an adjustable slit and x-ray source....	50
12. Schematic diagram of the electronic configuration for the microchannel plate detector.....	52
13. Comparison of two methods in electronically determining photon position on the microchannel plate.....	54
14. Least squares linear fit of MCP (CEMA) position versus peak position.....	55
15. Position scan as in Fig. 13 (b) but with carbon K x-rays and through a 50 micron slit.....	56

FIGURE

Page

16. Microchannel plate configuration for the grazing incidence spectrometer.....57
17. Geometry of the microchannel plate with respect to the grating and the photon beam defined by the entrance slit...59
18. Comparison of the geometrical prediction of wavelength versus channel number (heavy line) by equations (2.15)-(2.21) and the quadratic fit from a spectrum of peaks of known wavelength (light line).....64
19. MCP spectra of BeO at various values of angle θ at a spectrometer position 5.200 and a 100 μm entrance slit.....65
20. Intensity response of MCP to the movement of the Zr M α x-ray peak across the plate.....68
21. Linear fit (solid line) of Zr M α peak centroid (circles) versus spectrometer position.....69
22. Comparison of a SrO M α spectrum acquired with a CEM detector over 70 minutes (upper spectrum) with a composite of two MCP spectra of 7 minutes each (lower spectrum).....71
23. Composite microchannel plate spectrum₂ of 40 MeV neon excited by passage through a 20 $\mu\text{g}/\text{cm}^2$ carbon foil.....75
24. Microchannel plate spectra of 40 MeV neon taken at spectrometer odometer settings of 10.500, 9.500 and 8.000 from top to bottom, respectively.....77
25. Microchannel plate spectra of 40 MeV neon taken at spectrometer odometer settings of 6.800, 5.800 and 5.000 from top to bottom, respectively.....78
26. Spectrometer calibration fit to a second order polynomial for the center spectrum in Fig. 25.....80
27. Partial level diagram for singly excited Ne IX. The energy levels are drawn to scale and observed transitions are shown by solid lines marked with the observed wavelengths in \AA88
28. Spectra of 40 MeV neon on carbon taken at several foil positions.....94
29. Spectral comparison of 40 MeV neon passing through 150 $\mu\text{g}/\text{cm}^2$ gold (solid line) with 40 MeV neon passing through 20 $\mu\text{g}/\text{cm}^2$ carbon (dotted line).....100

FIGURE

Page

30.	Relative efficiency curve for the 1200 l/mm grating and microchannel plate detector.....	107
31.	Relative populations of the n=3 levels in Ne VIII and Ne IX for states of different orbital angular momenta.....	110
32.	Relative population of Ne VIII and Ne IX n=3 levels compared to statistical population.....	111
33.	Composite microchannel plate spectrum of foil excited argon.....	116
34.	Microchannel plate spectra of 80 MeV argon taken at spectrometer odometer settings of 11.300, 10.000, and 8.800 from top to bottom, respectively.....	119
35.	Microchannel plate spectra of 80 MeV argon taken at spectrometer odometer settings of 6.800, 5.800, and 4.800 from top to bottom, respectively.....	120
36.	Partial energy level diagram of Ar XIII. Wavelengths are given in Angstroms.....	126
37.	Partial energy level diagram of Ar XIV. Wavelengths are given in Angstroms.....	127
38.	Partial energy level diagram of Ar XV. Wavelengths are given in Angstroms.....	128
39.	Example of argon spectra taken at different foil positions representing delay times from top to bottom of: 0 psec, 39 psec, 220 psec, and 428 psec.....	134

CHAPTER I

INTRODUCTION

A. Background

Since the development of fine ruled gratings in 1882 by H. A. Rowland, chemists and astrophysicists have used their diffractive properties to study optical radiation from outer-shell transitions at wavelengths greater than 500 Angstroms (\AA). Similarly, since the inception of Bragg crystal spectrometers in 1913, spectroscopists have used crystals to study inner-shell transitions in the x-ray region of the electromagnetic spectrum from 0.1 to 30 \AA . Only within the last 20 years have ion-beam spectroscopists begun to examine the soft x-ray/extreme ultraviolet (EUV) spectral region at wavelengths from 30 to 500 \AA , where grating spectrometers operating at grazing incidence are required. Much of the recent interest in examining this rich spectral region comes from advances in fusion research where highly ionized plasmas radiate in the EUV, from the current space program which is conducting measurements of soft x-ray solar and interstellar phenomena, and from the intensifying effort to develop a soft x-ray laser. This latter effort involves a detailed understanding of excited atomic energy levels, excitation rates and mechanisms, transition probabilities, and predictions of gain caused by population inversions of excited levels¹.

The citations in this dissertation follow the format of the Physical Review A.

Two distinct areas of EUV spectroscopy have developed over the years: (1) the soft x-ray emission from chemical compounds or solid targets excited by electron bombardment, and more recently, (2) the radiative decay of highly ionized atoms as in plasmas or ion-beams. The soft x-ray region provides a means for critically testing band structure calculations of the solid state while providing insight into the bonding character of chemical compounds. Most of the work accomplished in this area has been by electron or photon excitation and an excellent review is provided in reference 2. However, since the research covered in this study is in the second of the two mentioned areas, the subject of soft x-ray emission from solid targets will not be addressed beyond explaining in Chapter II how soft x-rays were used to test and calibrate the grazing incidence spectrometer.

Nearly all studies of EUV radiation resulting from ion-atom collisions have emphasized the deexcitation of highly ionized atoms. EUV measurements below 300 Å and some even as high as 1000 Å have been accomplished with grazing incidence spectrometers. The first to report using a grazing incidence spectrometer for ion-atom spectroscopy was Bashkin *et al.*³, in 1964, with a preliminary study of Ne projectile EUV radiation.

Shown in Fig. 1 is a portion of the electromagnetic spectrum that spans the vacuum ultraviolet to x-ray region with the region served by grazing incidence spectroscopy shown in the center. Soft x-rays from various solids examined in the grazing incidence calibration tests are indicated in the upper part of the figure. The projectile EUV radiation that forms the basis of this research is delineated in the lower portion of the figure.

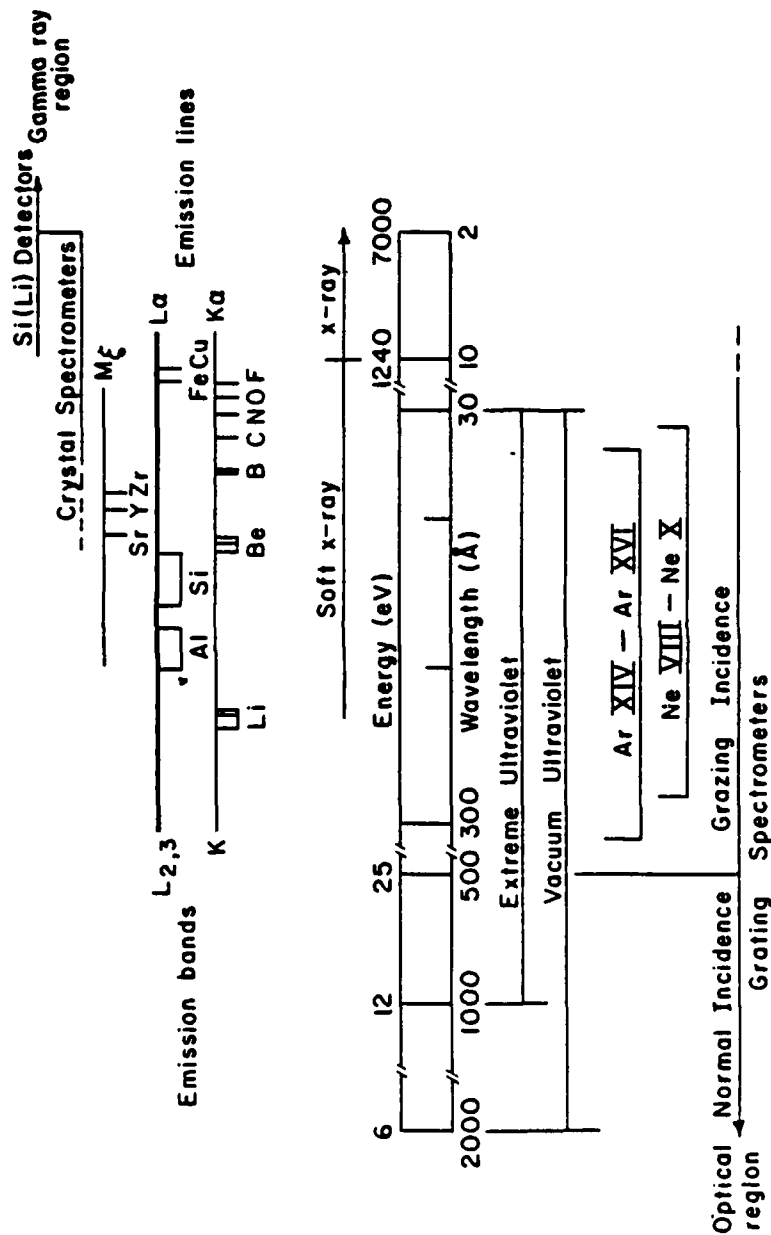


Fig. 1. Spectral region spanning the vacuum ultraviolet to x-rays.

B. Features of Grazing Incidence Spectroscopy

One of the major reasons that EUV studies are not as extensive as either optical or x-ray studies is that neither conventional grating monochrometers nor crystal spectrometers operate effectively in this spectral region. Crystal spectroscopy suffers from attenuation of long wavelength radiation as well as from lattice aberrations and temperature effects associated with the use of organo-metallic or pseudo crystals with large lattice spacings. Concave gratings suffer from a drastic loss of intensity when attempting to disperse light beyond a given critical angle of reflection⁴. This limitation forces the reflection of short wavelength emissions at very large angles of incidence (near 90 degrees), or when expressed by the complement, very small angles of grazing incidence.

To better understand why a grazing angle of incidence is necessary to reflect short wavelength radiation, a brief description of how the critical angle of reflection depends upon both the grazing angle of incidence and the refractive index of materials is given. Specifically, the refractive index, u , for any material reflecting x-rays is less than unity and is expressed by:⁵

$$u = 1 - Ne^2\lambda^2/2\pi mc^2, \quad (1.1)$$

where N is the electron density, λ is the incident wavelength, and e and m are the charge and mass of the electron. In addition, Snell's law states that for a and b angles of incidence and refraction

$$u = \sin a / \sin b . \quad (1.2)$$

Then, by use of Snell's law and a trigonometric identity,

$$\sin a_c = \lambda (e^2 N / mc^2 \pi)^{1/2} , \quad (1.3)$$

where total reflection of a photon of a given wavelength may occur at grazing angles up to a maximum angle, a_c , after which the reflection drops off rapidly. In a similar manner, the minimum wavelength which can be reflected at these small angles of incidence is given by⁴

$$\lambda_{\min} = 3.33 \times 10^{14} N^{-1/2} \sin a . \quad (1.4)$$

As an example, the minimum wavelength reflected from gold at an angle of incidence of three degrees is 8.06 Å. Yet, at the same angle of incidence, reflection off an oil-coated surface results in a minimum wavelength of 33.5 Å.

The historical condition of the surface of a grating under a normal experimental environment is largely unknown. However, when the reflection efficiency of wavelengths near the short wavelength cutoff is noticeably reduced, a surface contamination problem with the grating is a likely cause. Although grazing incidence spectrometers are inherently inefficient due to astigmatism, spherical aberration, and small solid angle acceptance (these features to be discussed more thoroughly in Chapter II), recent advances in grating manufacture and electronic detection efficiency compensate for these limitations and

still allow worthwhile measurements by techniques such as the beam-foil method⁶.

C. Introduction to Beam-foil Spectroscopy

The beam-foil method is illustrated in Fig. 2. A monoenergetic beam from the cyclotron is magnetically analyzed for the correct charge-to-mass ratio and focused to pass through a thin foil target. The beam interacts with the atoms of the foil through a number of mechanisms. These include direct ionization, electron loss and capture, and Coulomb excitation. At MeV/amu energies, the beam reaches charge-state-equilibrium after passing through a target thickness of approximately $10 - 20$ micrograms/cm² and then exits the foil in a highly ionized state⁷. Since the deexcitation in the form of radiative transitions of foil-excited ions then occurs in the vacuum downstream from the foil, there is the distinct advantage that the resulting spectra are essentially free from an intense bremsstrahlung radiation background. As shown in Fig. 2, the radiation is diffracted by the 1-meter radius grating (drawn larger than scale for illustrative purposes) with the grazing incidence spectrometer set at 90 degrees to the beam axis. The entrance slit, exit slit and grating are all positioned on the Rowland circle. A suitable detector for the soft x-radiation such as a windowless channel electron multiplier (CEM) is mounted directly behind the exit slit.

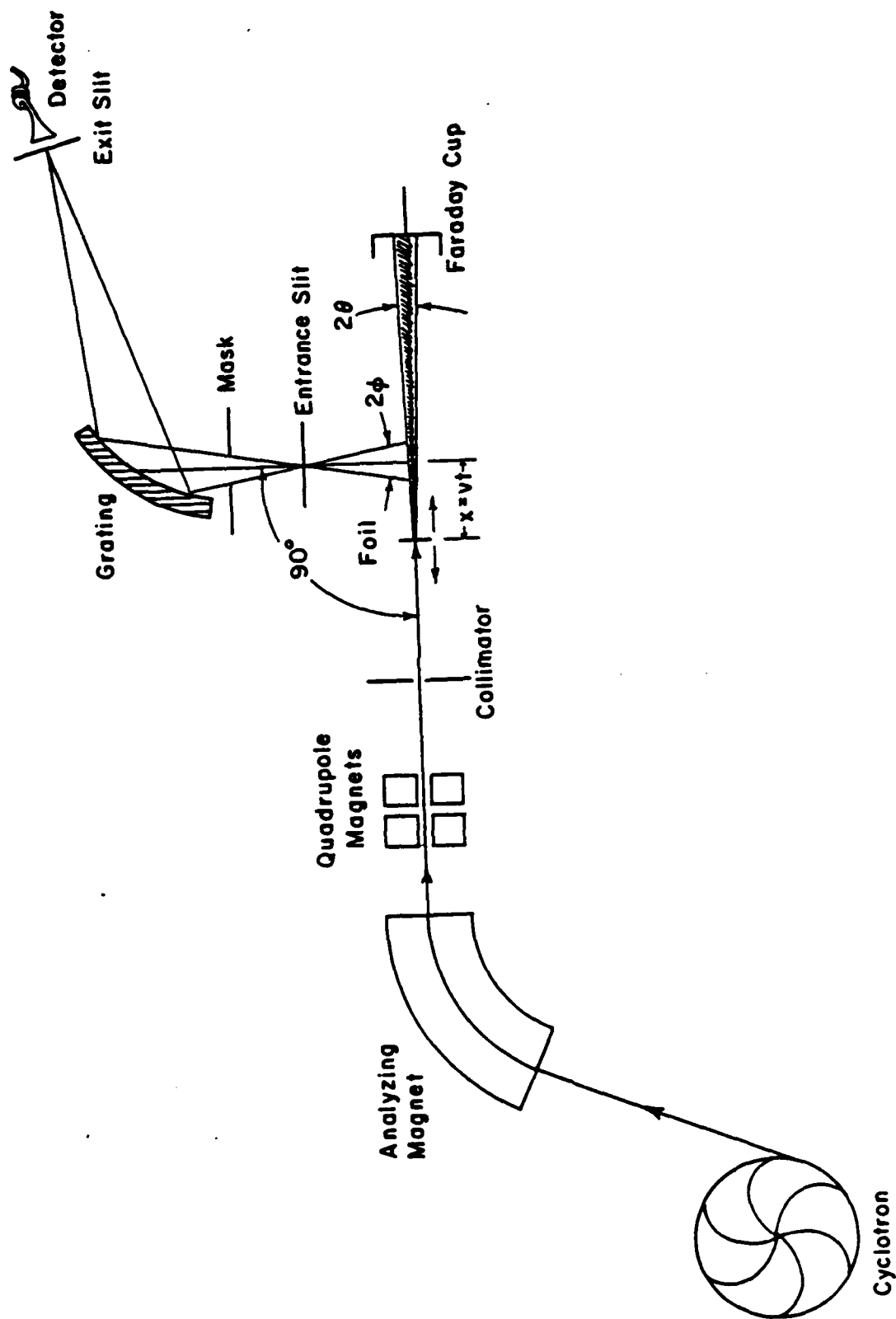


Fig. 2. Beam-foil geometry. The grating size and angles ϕ and θ are exaggerated for illustration.

The beam-foil source has a number of advantages over other light sources. Some of these features will be discussed separately in more detail but are briefly mentioned here:

- (1) The beam can be made chemically and isotopically pure.
- (2) Foil-excited ion beams have a narrow distribution of charge states that depend directly upon the beam energy. Thus, the judicious choice of beam energy will allow a particular ionization state to be optimized.
- (3) The beam-foil source is highly efficient in producing multiply excited states of high principal quantum number, n , and high angular momentum, l .
- (4) The low particle density of the beam (on the order of 10^5 particles/cm³) allows radiation unperturbed by the collisional deexcitation and severe Stark mixing effects characteristic of relatively high density (on the order of 10^{14} - 10^{19} particles/cm³) plasma sources⁸.
- (5) The sudden and coherent nature of the excitation, where the beam passes through the thin foil experiencing multiple collisions on the time scale of 10^{-15} seconds, allows for the measurement of fine and hyper-fine structure by the quantum beat method.
- (6) Yet, the greatest advantage of the beam-foil source is the excellent time resolution of the detected radiation. This is obtained by measuring the intensity of the light emitted from the highly stripped ions of known velocity as a function of distance from the foil as is illustrated in Fig. 2. The upstream distance of the foil x is equal to the product of

the beam velocity v and the time elapsed from beam excitation to detection.

A disadvantage of the beam foil source is that its intensity is rather weak. Thus, any improvement of the detection efficiency would allow more efficient use of available beam time.

D. Foil Effects

A number of factors must be considered in choosing the type and thickness of the exciting foil. In most cases thin carbon foils are used because of their ease of manufacture and their resistance to breakage by the high velocity beam. In addition, the stopping power (slowing of the ion beam) and large-angle Rutherford scattering both increase the greater the nuclear charge of the target foil. The foil thickness is chosen to be thin enough to minimize beam energy loss and multiple scattering but thick enough to produce charge-state-equilibrium and prevent undue breakage in handling.

Curtis et al.⁹ and Kay¹⁰ calculated the errors introduced into mean lives by both energy straggling and beam spreading and found these effects to be negligible for thin foils ($5-10 \mu\text{g}/\text{cm}^2$) even for low beam velocities. Due to the statistical nature of the beam undergoing multiple collisions within the foil, the beam experiences an average energy loss ΔE with a finite width δE , the energy straggling. A simple model of energy straggling proposed by Andra¹¹ equates δE to the ratio of ΔE to the square root of the number of atomic layers, N , in the foil:

$$\delta E = \Delta E/N^{1/2} . \quad (1.5)$$

For the present measurements, a carbon foil thickness of approximately $25 \mu\text{g}/\text{cm}^2$ results in a 0.2 MeV energy loss by a 41 MeV Ne beam passing through it based upon the stopping power predictions given by Northcliffe and Schilling¹². The energy straggling for this approximate 625 atomic layer foil then amounts to only 4% of ΔE (0.008 MeV) and can be neglected.

The angular spread (shown by 2θ - in Fig. 2), which results from the momentum transfer between the target and the beam, is also generally negligible for high energy heavy ion beams passing through low Z foils. The calculation of this mean scattering angle of the beam due to multiple collisions within the foil was accomplished by two different methods. In the first method, Stoner and Radziemski¹³ derived an expression for the mean squared scattering angle $\bar{\theta}^2$ for ions experiencing multiple collisions while passing through a thin foil:

$$\bar{\theta}^2 = (2\pi N x Z^2 z^2 e^4 / E^2) \ln[a_0 E / Z^{4/3} e^2 z] , \quad (1.6)$$

where N - foil atom density, x - foil thickness, Z - target foil atomic number, z - ion projectile atomic number, e - electronic charge, E - incident ion laboratory energy, and a_0 - first Bohr radius. For high energy beams θ varies as $1/E$. In the second method, Marion and Zimmerman¹⁴ derived a set of expressions and accompanying graph based on multiple scattering theory that gives mean scattering angles that closely match experimental results for MeV/amu velocity beams through moderate thickness foils.

The scattering angle also has a finite effect on the width of a spectral line where the width at $1/e$ maximum height is given by¹³:

$$d\lambda_{1/e} = 2 \lambda_0 (v/c) \theta \quad , \quad (1.7)$$

where λ_0 = wavelength emitted in the ion's rest frame, v = beam velocity, and c = speed of light. Since v/c is proportional to $E^{1/2}$ and θ is proportional to $1/E$, the scattering contribution to the line width is then proportional to $E^{-1/2}$. The following table summarizes the mean scattering angles calculated by both above methods and the effect on linewidths for combinations of 2 MeV/amu Ne and Ar ions on various foils.

TABLE 1. Foil scattering effects.

Ion Beam	Foil ₂ ($\mu\text{g}/\text{cm}^2$)	θ (degrees) ^a		Scattering ^b Width (\AA)
		Method 1	Method 2	
Ne	C (20)	0.09	0.06	0.06 @ 300 \AA
Ne	Ag (80)	0.41	0.36	0.09 @ 100 \AA
Ne	Au (150)	0.66	0.62	0.15 @ 100 \AA
Ar	C (25)	0.10	0.45	0.31 @ 300 \AA

^a Method 1 from ref. 13 and Method 2 from ref. 14.

^b Line width contribution due to multiple scattering based on the larger of the two predicted angles and at the longest wavelength of interest as shown in this study.

E. Doppler Effects

Doppler effects must also be considered when measuring radiation emitted from fast moving ions. The wavelength of the radiation will be

Doppler shifted in the laboratory frame as well as Doppler broadened. The magnitude of the first-order shift depends upon the beam velocity and the viewing angle with respect to the beam direction. Depending on observation angle, this shift $\Delta\lambda/\lambda$ can be either red-shifted or blue-shifted and is given approximately by:

$$\Delta\lambda/\lambda = \beta \cos \theta , \quad (1.8)$$

for a beam velocity v , where $\beta = v/c$ and θ is the observation angle. For example, a 2 MeV/amu beam gives a 0.23 Å red shift to a 200 Å line when viewed at 89.0°. However, even at $\theta = 90^\circ$, the line will be shifted due to the second order Doppler shift. This shift which is independent of observation angle is given approximately by⁶

$$\Delta\lambda/\lambda = 1/2 \beta^2 , \quad (1.9)$$

and results in a 0.43 Å blue shift for the same 200 Å line. Thus at a certain angle, a line may not appear to shift significantly from its rest frame wavelength due to the compensating effects of the first order Doppler shift in a direction opposite to the second order Doppler shift.

Doppler broadening depends upon the beam velocity and the acceptance angle ϕ of the spectrometer (see Fig. 2). The acceptance angle is determined by the size of the mask placed in front of the grating as shown. The choice of mask size is determined by the optimum illuminated grating width (see Chapter II) which corresponds to the best spectral wavelength resolution and intensity for a given line.

The mask also determines the temporal resolution. In the present application, the use of a 0.56 mm mask with a 15.7 mrad angle of acceptance resulted in a Doppler broadening $\Delta\lambda$ of approximately¹¹:

$$\Delta\lambda = \lambda_0 \beta \phi . \quad (1.10)$$

At $\beta = 0.0655$, $\phi = 15.7$ mrad and $\lambda_0 = 200$ Å, the Doppler broadening amounts to 0.21 Å, approximately 25% of the 0.8 Å instrumental resolution obtained with 100 micron slit widths.

This acceptance angle Doppler broadening contribution to line width has a $E^{1/2}$ energy dependency so that in combination with the scattering angle contribution to line width that has a $E^{-1/2}$ dependence, the overall effect is an energy-independent resolution response. However, for the work reported here with lines of a wavelength less than 300 Å and with a modest resolution of approximately 1 Å, these two line width contributions are not a limitation.

F. Ion-Beam Charge State Considerations

At charge-state-equilibrium, the average charge state \bar{q} of the exiting ion beam is given to good approximation by the semi-empirical equation developed by Nikolaev and Dmitriev¹⁵

$$\bar{q} = [1 + (Z^{-a} v/v')^{-1/k}]^{-k} Z , \quad (1.11)$$

where Z = nuclear charge of the ion beam, $a = 0.45$, $k = 0.6$, and $v' = 1.65 v_0 = 3.61 \times 10^8$ cm/sec. The various charge states form a Gaussian distribution about this average value. The width d associated with this distribution is given closely by

$$d = 0.5 (\bar{q}[(1 - \bar{q}/Z)^{1.67}])^{1/2} \quad (1.12)$$

This results in \bar{q} and d values for 2 MeV/amu neon and argon as shown in Table 2.

TABLE 2. Average beam charge and distribution widths.

Beam	Energy (MeV)	\bar{q}	d
Ne	40	8.4	± 0.31
Ar	80	14.0	± 0.53

Thus, the charge-state distributions are predicted to be quite narrow, and only three charge states are expected to provide intense transitions at these energies.

Small target foil effects have been reported where higher Z target foils are noted to cause a full one unit decrease of the equilibrium-charge-state value¹⁶. This effect is presumably due to the reduced electron capture cross sections in low Z targets. Other small effects have been measured where it was concluded that surface contamination can account for changes of a few percent in charge-state distributions¹⁷.

A final foil property to be discussed is the choice of a foil thickness that will produce an equilibrium charge-state-distribution. With extremely thin foils and fast beams, charge-state-equilibrium of the beam exciting the foil may not have been reached. Small accumulations of carbon during a lifetime measurement would then introduce errors to the analysis if the charge state fractions of the beam continually change during the measurement. Foil thickening due to carbon build-up on the target with beam exposure is pronounced for low energy beams and can amount to tens of ng/cm^2 with sub-MeV incident energy beams at current densities of $\mu\text{A/cm}^2$. For charge-state-equilibrated beams, this foil thickening would not change the charge state fractions and add error to the lifetime determination. A very rough but useful approximation for the charge-state equilibrium thickness X_e is given by the empirical relation¹⁶

$$X_e = 8 E/A [\mu\text{g/cm}^2] , \quad (1.13)$$

determined from a simple eye-fit to a display of data obtained for carbon targets with ion beams $6 \leq Z_1 \leq 36$ for a energy to atomic mass ratio E/A in MeV/amu from 0.5 to 10. Thus, for 2 MeV/amu beams, an X value of approximately $20\text{-}25 \mu\text{g/cm}^2$ should be sufficient to produce charge-state equilibrium.

G. Beam-foil Method

As mentioned previously, the application of beam-foil spectroscopy for the measurement of atomic lifetimes results from its straight

forward method of relating line intensity with foil position. As illustrated in Fig. 2, the temporal position of the foil is directly related to its spatial position along the beam path. Beam-foil lifetimes can be measured without estimates of detection efficiency or assumptions about the density of the radiating particles, quantities that are necessary in alternative lifetime methods. Accurate lifetimes are critical for astrophysical abundance determinations, plasma diagnostics and laser excitation processes¹⁸. The beam-foil method was first applied to heavy-ion accelerators in 1963 by Kay¹⁹ and the first application for lifetime measurements were initiated in 1964 by Bashkin³.

If the initial population of a state i due to collisions in the foil is $N_i(t)$, this state will decay to states j with a decay rate given by

$$dN_i/dt = (-\sum_j A_{ij}) N_i = -N_i/\tau \quad , \quad (1.14)$$

where i decays to j with the transition probability A_{ij} and τ is the lifetime of state i . If the population of $N_i(t)$ is given only by the number of atoms excited to levels i during the collision, $N_i(t)$ will decay to each lower state j by an exponential decay given by

$$N_{ij} = N_{ij}(0) \exp(-t/\tau_i) \quad . \quad (1.15)$$

If however, the collision process populates a great number of higher levels of a given ion, the population $N_i(t)$ is due both to its initial population and to the repopulation or cascade contribution by

higher levels, N_k , that decay to this level during time t . The decay rate of the initial state which now includes cascade feeding is given by

$$dN_i/dt = - \sum_j (A_{ij}) N_i + \sum_k A_{ki} N_k, \quad (1.16)$$

which forms a set of coupled differential equations. These can be solved as a sum of exponentials for the primary decay time and cascade decay times if all initial populations of the respective levels are known such that

$$N_i(t) = N_i(0) \exp(-t/\tau_i) + \sum_{k1} f(k1 \rightarrow i) + \sum_{k2k1} f(k2 \rightarrow k1 \rightarrow i) + \dots, \quad (1.17)$$

where the first term on the right-hand side is the primary decay and the second and succeeding terms are first and higher order cascades⁷. The mean life τ_i and its inverse α_i are related to the transition probabilities from initial to final states by:

$$1/\tau_i = \alpha_i = \sum_j A_{ij}. \quad (1.18)$$

Three simple decay schemes presented in a review by Martinson and Gaupp²⁰ which illustrate the types of decay commonly encountered in beam-foil spectroscopy are shown in Fig. 3. The decay of the Be II ($2p^2$) 3P state in (a) is well represented by a single exponential. The slope of the exponential directly yields the lifetime. The decay curve of C II ($3p$) 2P in (b) is the less common case of a "growing-in"

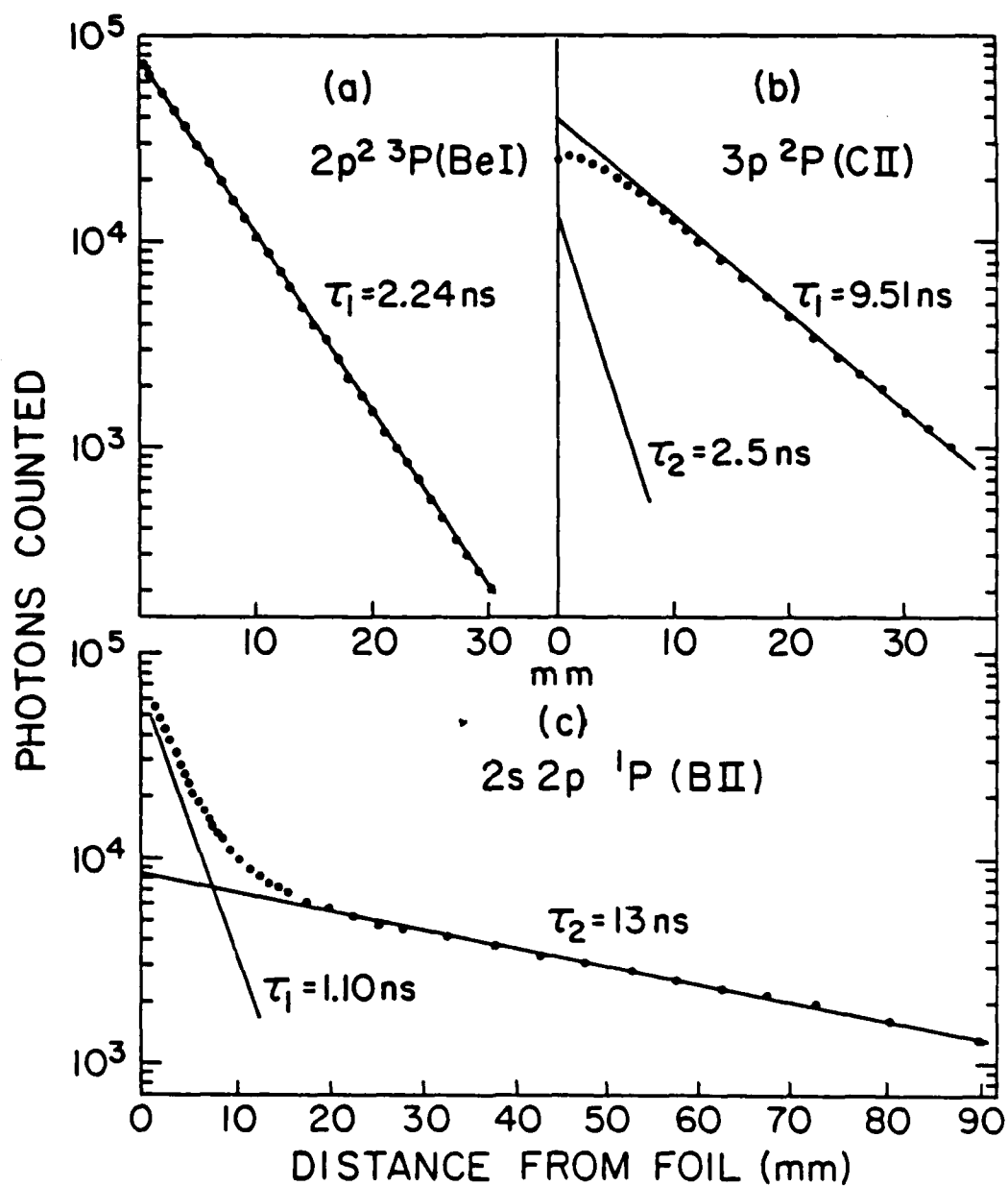


Fig. 3. Examples of decay schemes

cascade from a shorter-lived higher level. The decay is then a difference between two exponentials. Often for such an effect to be measurable, the higher level must be the principal feeding branch. A separate measurement of the higher level should yield the lifetime of this feeding branch directly. The most common decay case is shown in (c) where the decay curve of the B II $(2s2p) \ ^1P$ state is composed of two exponentials, the first of which is the prompt decay of the $\ ^1P$ level and the second of which is the feeding from the relatively long-lived $(2p^2) \ ^1P$ upper level.

Measured lifetimes of one element are often compared with the results of other elemental measurements as well as with theoretical predictions along isoelectronic sequences. A particularly useful comparison is made along the smooth trends of oscillator strengths since these properties scale with varying nuclear charge. The oscillator strength f is a dimensionless quantity that is related to the transition probability, A_{ij} by

$$f = mc/8\pi e^2 (\lambda_{ij}^{-2}) (g_j/g_i) A_{ik} , \quad (1.19)$$

where λ_{ij} is the wavelength of the transition i to j , m and e are the electron mass and charge, and c is the speed of light. These constants combine to give 1.499×10^{-16} when λ is expressed in Angstroms and A_{ij} in sec^{-1} . The g_i and g_j terms are the statistical weights of the initial and final levels given by $2J + 1$.

H. Related Research

Within the last fifteen years, spectroscopists have studied many transitions of low Z elements and have refined the techniques for making lifetime measurements. A wealth of data has been accumulated on energy levels and wavelengths, but the present data base of the spectra of the elements is far from complete. As pointed out in a recent review by Martinson²¹, even in systems which were considered reasonably complete such as Cr II, hundreds of new lines have been recently discovered.

The number of studies of high energy noble elements, such as neon and argon, have been limited by the availability of accelerators capable of producing high charge state ions of sufficient intensity. An overview of vacuum ultraviolet beam-foil measurements at wavelengths of less than 1000 Å of neon and argon ions are shown in Tables 3 and 4.

TABLE 3. Vacuum ultraviolet beam-foil studies of neon at less than 1000 Å.

Reference	Beam Energy (MeV)	Ions	Wavelength Range (Å)	Levels	Lifetime Range (psec)
Irwin 1973 ²²⁻²⁴	0.2-1.6	Ne I-VII	209-1200	n=2-2	53-26,000
Buchet 1975 ²⁵	1-2	Ne III-VII	80-350	n=2-3,4,5	12-170
Bashkin 1966 ²⁶	5.1	Ne II-VII	250-1300	n=2-2,3,4	72-240
Livingston 1984 ²⁷	7	Ne VIII	720-735	n=2-2	50-540
" "				n=5-7	
Hardis 1984 ²⁸	8.2	Ne VII	510-565	n=2-2	90
Barrette 1973 ²⁹	3-14	Ne VII-VIII	50-150	n=2-3,4,5,6,7	17-43
Barrette 1974 ^{30,31}	13	Ne VII-VIII	75-300	n=2-3,4,5	5-50
" "				n=3-4,5	
Buchet 1973 ³²	23	Ne VII-X	30-300	n=2-3,4	10-200
" "				n=3-4,5	

TABLE 3. Continued

Reference	Beam Energy (MeV)	Ions	Wavelength Range (Å)	Levels	Lifetime Range (psec)
Buchet 1973			300-1200	n=4-5	---
" "				n=5-6,7	
Buchet 1976 ³³	23	Ne VIII-X	12-300	n=2-3,4,5	---
" "				n=3-5,6	
Demarest 1986 ^a	41	Ne VIII-X	45-330	n=2-3,4,5	9-1100
" "				n=3-4,5,6,7,8	
" "				n=4-6,7	
" "				n=5-9	

^a This work.

TABLE 4. Vacuum ultraviolet beam-foil studies of argon at less than 1000 Å.

Reference	Beam Energy (MeV)	Ions	Wavelength Range (Å)	Levels	Lifetime Range (psec)
Livingston 1981 ³⁴	0.2-1.8	Ar V-VIII	400-1500	n=3-3	30-4000
" "				n=4-5	
" "				n=5-6	
" "				n=6-7	
Berry 1976 ³⁵⁻³⁷	1-3	Ar VI-VIII	48-800	n=2-3	5-1200
" "				n=3-3,4,5,6	
" "				n=4-5,6	
Buchet-Poulizac 1983 ³⁸	2.5	Ar IX	450-900	n=3-3	100-700
Buchet 1974 ³⁹	46	Ar X-XV	150-300	n=2-2	---
" "			300-1300	n=3-3	---
" "				n=5-6	---
" "				n=6-7	---
" "				n=7-8	---
Demarest 1986 ^a	81	Ar XII-XVI	60-355	n=2-2	10-740
" "				n=3-4	
" "				n=4-5,6,7	
" "				n=5-6,7	
" "				n=6-8	

^a This work.

Beam-foil spectra may also provide information on the mechanism of excitation and the distribution of excited states with respect to the principal quantum number n and the angular momentum quantum number l of ions emerging from the foil. Experimental findings to date are limited and not well understood. Independent studies of fast ions (>3.5 MeV/amu) of oxygen and sulfur inferred an overpopulation of states of low l for oxygen and high l for sulfur⁴⁰. The relative population of $n=4-5$ transitions in B III were found to favor s and p levels⁴¹. Also a recent study of titanium ions⁴² using composite foils of carbon and other materials found that the foil material had little to no influence on the relative populations of low-lying $n=4$ states. Additional investigation of relative population mechanisms appears warranted. It was the purpose of this research to:

- (1) construct an enhanced efficiency multichannel detection system for a grazing incidence spectrometer.
- (2) examine the deexcitation of highly ionized beams of 41 MeV neon and 81 MeV argon in the EUV wavelength region to classify by beam-foil spectroscopy previously unreported lines.
- (3) measure lifetimes of Ar XIV and Ar XV $n = 2$, $\Delta n = 0$ transitions and compare them along isoelectronic sequences.
- (4) examine the influence of different Z foils on the lifetimes and intensity distributions of neon transitions to the $n = 2$ shell.

In Chapter II the experimental aspects of the adaptation of the grazing incidence spectrometer into an off-line testing configuration and an on-line operating system are discussed. The beam-foil

measurements of 41 MeV neon are presented in Chapter III with a discussion of the spectral influence of the target foil material. The improvement in the efficiency of data collection with the new multichannel detector is provided. The results of the beam-foil measurements of 81 MeV argon are presented in Chapter IV. The lifetimes of the Ar $n=2-2$ transitions are compared to predictions along isoelectronic sequences. New Ar lines are compared to theoretical calculations and given assignments. Conclusions and suggestions for additional research are given in Chapter V.

CHAPTER II

EXPERIMENTAL METHODS

A. Operating Principles for Grazing Incidence Spectroscopy

The successful operation of a grazing incidence spectrometer requires a working knowledge of grating optics, consideration of vacuum technology, and insight into the choice and development of an optimum detector. These topics are covered in sequence in this chapter.

To understand grazing incidence optics, it is useful to begin by examining the physical geometry involved. Fig. 4 shows a common geometry of the grazing incidence condition. A fixed entrance slit, a fixed grating of radius R , and a movable exit slit/detector all lie on the arc of the Rowland circle of diameter R . Photons enter the entrance slit at a fixed angle of incidence α , measured from a normal to the grating at its center. Constructive reinforcement of all diffracted rays occurs when the grating equation is satisfied:

$$m \lambda = \sigma (\sin \alpha - \sin \beta) \quad , \quad (2.1)$$

where m is the order of reflection and λ is the wavelength of the photon. When λ is expressed in \AA , σ , the grating spacing, is given by the quotient of 10^7 to the number of lines per mm or 8333.33 \AA for a 1200 l/mm grating. Angles α and β are as shown in Fig. 4. The term $\sin \alpha$ is constant, whereas $\sin \beta$ varies as the detector changes position along the Rowland circle.

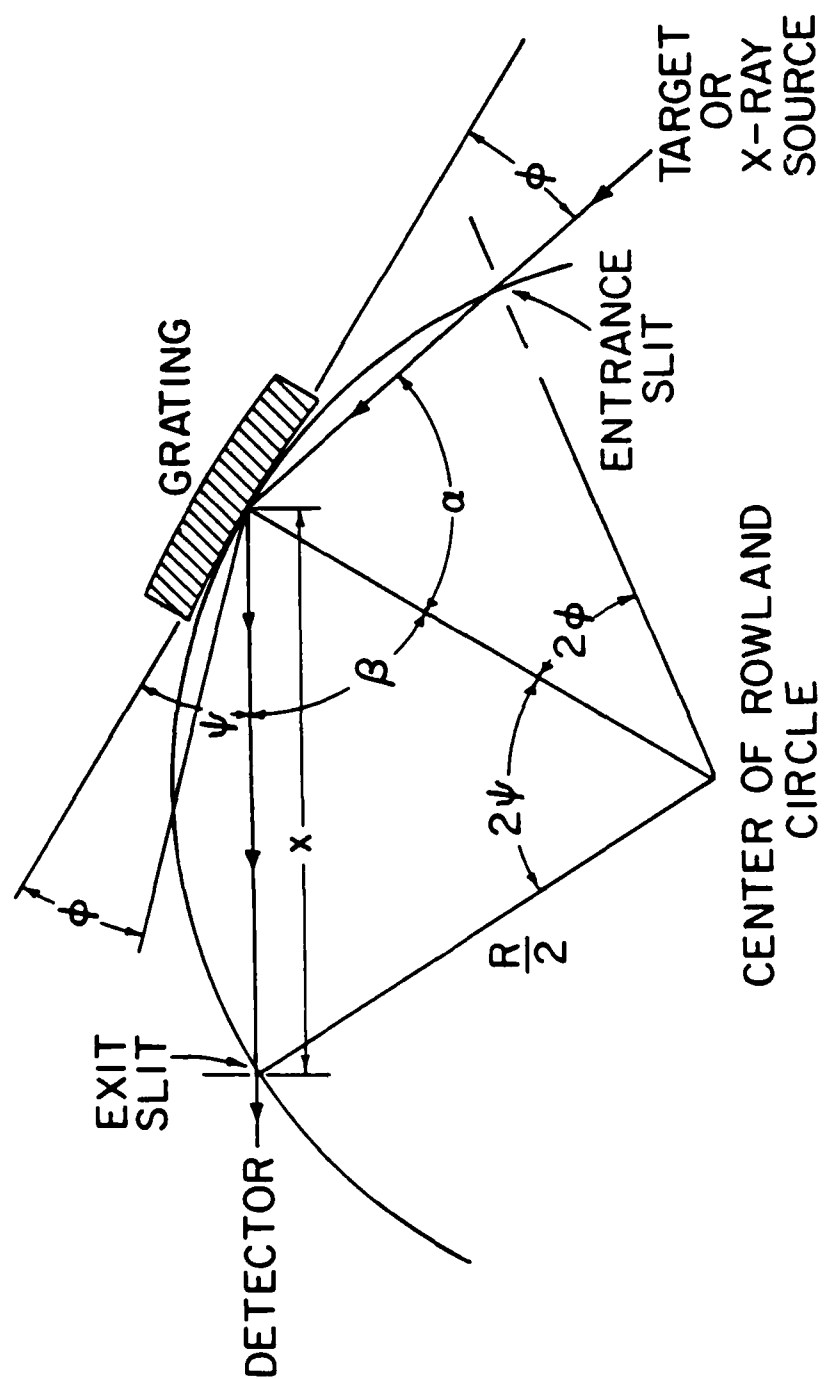


Fig. 4. Grazing incidence geometry.

For this research a Minuteman Model 310GM⁴³ one-meter grazing incidence monochrometer was used. The exit slit and detector combination move along a precisely machined track. The position of the exit slit is given by a counter reading corresponding to the chord length X of the arc defined by 2ψ as shown in Fig. 4. A convenient expression for the diffraction angle β is obtained from the equation of a chord where $X = R \sin \psi$, which is the same as $X = R \sin (90^\circ - \beta)$, so that $X/R = \cos \beta$. Substituting this expression of $\cos \beta$ into the identity $\sin^2 \beta = 1 - \cos^2 \beta$, Eq. (2.1) can be rewritten as

$$m\lambda = \sigma \sin \alpha - \sigma [1 - (X/R)^2]^{1/2} \quad (2.2)$$

The spectrometer five digit counter displays the chordal distance inches and is accurate to within $\pm 1 \times 10^{-3}$ inches. The Minuteman spectrometer incorporates a precision screw, driven by a 200 step per revolution DC stepping motor, that steps the exit slit/assembly in even increments of chordal distance. The minimum and maximum values for X are 2.000 and 11.250, which correspond to ψ values of 2.92° and 16.62° or β_{\min} and β_{\max} of 87.08° and 73.38° , respectively. Incidentally, these angles are easily obtained from the relation $\psi = \sin^{-1} (X/R)$. A plot of the energy/wavelength region accessed by a 1200 l/mm grating is given in Fig. 5.

The energy of a diffracted soft x-ray changes rapidly in a nearly hyperbolic manner with decreasing chord length. By contrast, the wavelength of a diffracted soft x-ray changes in a more gradual manner and is very nearly given by a quadratic expression of chord length. This behavior follows from Eq. (2.2), since at small angles the

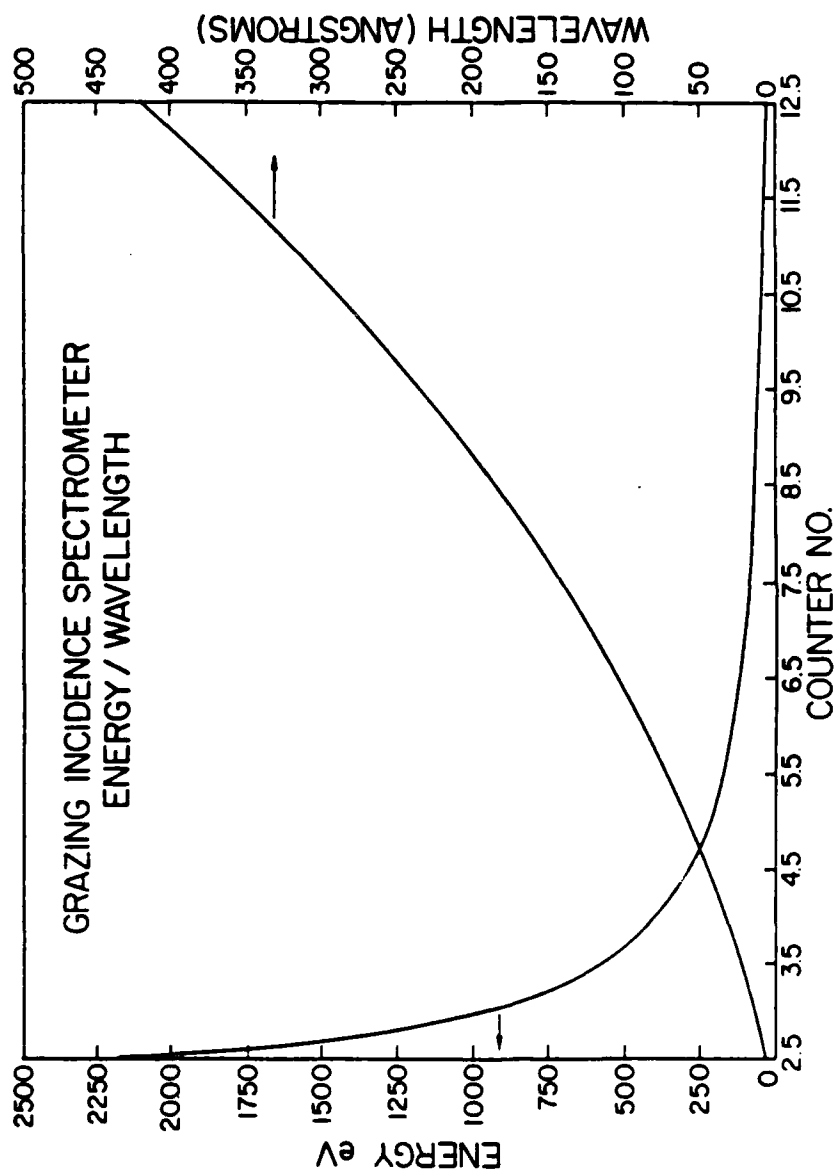


Fig. 5. Spectral region sampled by the Minuteman 310GM spectrometer with a 3° grazing angle of incidence and a 1200 1/mm grating.

trigonometric functions can be approximated by a series expansion retaining up to second order terms⁴⁴

$$m \lambda = c (d + 1/2 d^2) , \quad (2.3)$$

where c is a constant and d is an angular increment.

The theory of concave gratings has developed over the years since Rowland's contributions in 1883⁴⁵. References 4 and 46-50 give comprehensive discussions of the various optical parameters involved. The most critical condition is that which pertains to focusing, because at grazing incidence the chordal distance is a rapidly varying function of angle⁴⁴. Also, the inherent aberrations in concave grating reflections impose a practical limit on the maximum size grating that can be used without a noticeable loss of resolution. This optimum width w_{opt} , as derived by Mack, Stehn and Edlen⁴⁶ is given by

$$w_{opt} = 2.51 [R^3 \lambda (\cos \alpha \cos \beta / \sin^2 \alpha \cos \beta + \sin^2 \beta \cos \alpha)]^{1/4}. \quad (2.4)$$

Values of w_{opt} for a 1200 l/mm grating at a number of wavelengths are given in Table 5.

TABLE 5. Optimum width for a 1-meter radius 1200 l/mm grating.

β (deg)	X (in)	λ (Å)	w_{opt} (mm)
73.0	11.497	352.7	15.9
77.0	8.846	202.2	13.6
80.0	6.828	115.2	11.7
83.0	4.792	50.7	9.3
85.0	3.427	20.3	7.2

The maximum width of the grating can be limited to the desired size by placing a grating mask between the grating and the entrance slits, as shown in Fig. 2, Chapter I. Mask widths of 0.559 mm and 0.279 mm result in illuminated grating widths of 16.0 mm and 7.8 mm, respectively. The larger mask was used throughout this work to achieve greater intensity.

Dispersion and resolving power are two closely related spectral properties of concave gratings. Dispersion determines the separation of two wavelengths, while resolving power determines whether these two lines can be distinguished. A common way of expressing dispersion is in terms of the plate factor. The plate factor $\Delta\lambda/\Delta l$ is the reciprocal of the "linear dispersion" or increment of Rowland circle circumference per unit of wavelength and can be determined from the diffraction geometry given in Fig. 4, Chapter I and from the grating equation, Eq. (2.1) by a series of expressions presented in Ref. 4 to give

$$d\lambda/dl = (d\lambda/d\Psi) (1/R) = \sigma \cos \beta / (m R) = \sigma \sin \Psi / (m R) . \quad (2.5)$$

At large angles of incidence or small grazing angles, the plate factor is small and dispersion large. From Eq. (2.5), it is found that dispersion can be increased by using gratings with larger numbers of lines per mm, i.e. smaller σ values.

Another way of expressing this reciprocal dispersion in terms of units of wavelength per increment of chord length is by taking the derivative of Eq. (2.2)

$$d\lambda/dX = \sigma X / (MR^2 [1 - (X/R)^2]^{1/2}) . \quad (2.6)$$

For small values of X , Eq. (2.6) is nearly linear. Equations (2.5) and (2.6) give very similar values for a 1-meter spectrometer with a 1200 1/mm grating, as is indicated in Table 6.

TABLE 6. Plate factor and reciprocal dispersion.

X (in)	β (deg)	λ (Å)	$d\lambda/dl$ (Å/mil)	$d\lambda/dX$ (Å/mil)
3.427	85.0	20.3	0.0185	0.0185
4.792	83.0	50.7	0.0258	0.0260
6.828	80.0	115.2	0.0368	0.0378
8.846	77.0	202.2	0.0477	0.0489
11.497	73.0	352.7	0.0620	0.0648

The linearity of both dispersion relations when plotted against the spectrometer position (chord length) is shown in Fig. 6. The curves are nearly superimposed over the lower half of the spectrometer range. Fits to straight line approximations of the curves give

$$d\lambda/dl = 5.39 \times 10^{-3} X \quad (2.7)$$

$$\text{and } d\lambda/dX = 5.68 \times 10^{-3} X - 1.17 \times 10^{-3} \quad (2.8)$$

Resolving power, R' , is based upon the criterion⁴⁹ that two lines of equal intensity are resolved when their wavelength difference $\Delta\lambda$ is such that the fraction of the intensity at the midpoint between the lines is $8/\pi^2$, i.e. 0.81 of the intensity of the lines at their peak. Two factors influence R' : Grating-limited resolving power, R'_g , and slit-limited resolving power, R'_s , where R' is defined as

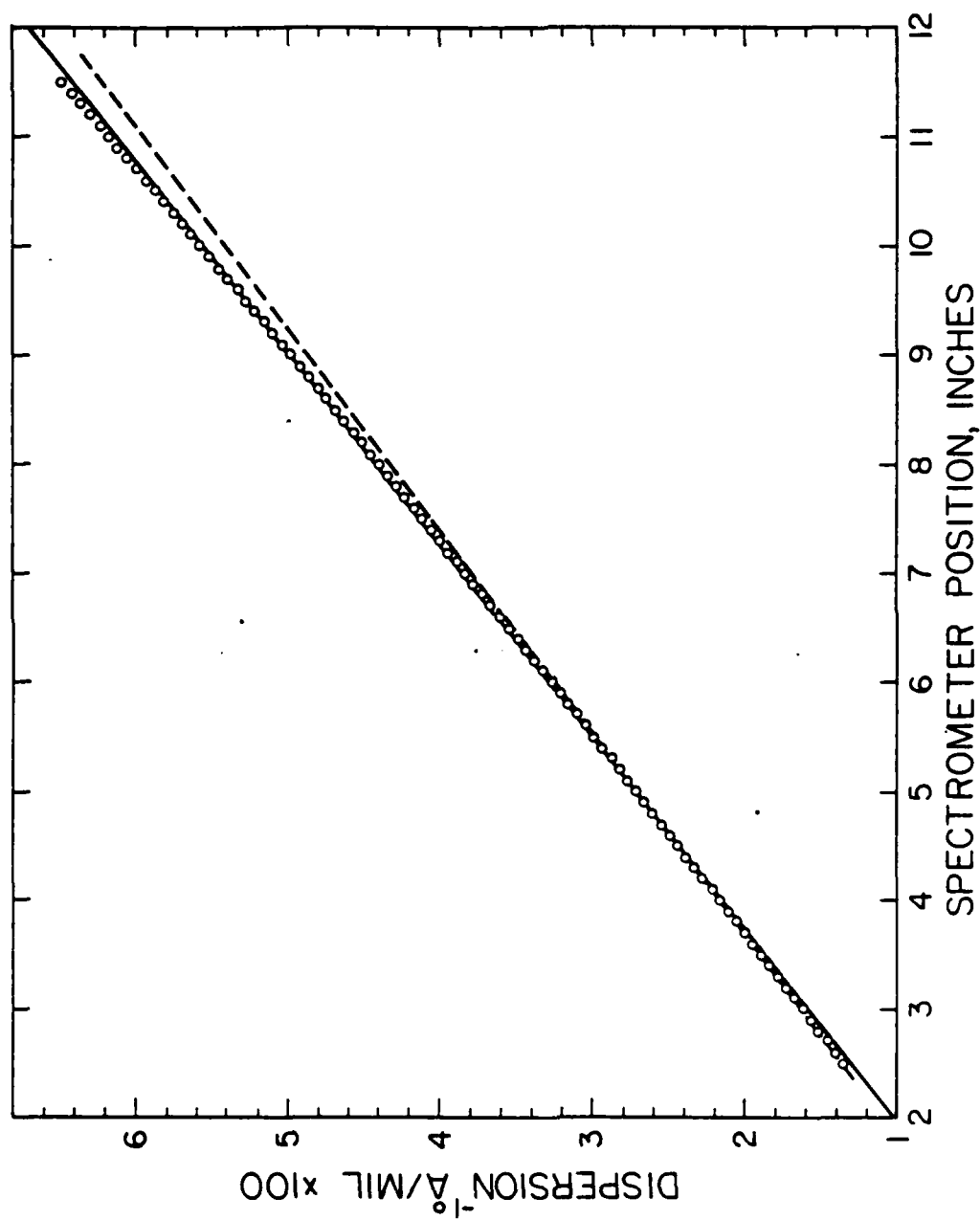


Fig. 6. Plate factor (dashed line) and reciprocal dispersion (circles) in Å/mil versus the spectrometer position in inches for the 1200 1/mm grating.

$$R' = \lambda / \Delta \lambda \quad (2.9)$$

Larger values of R' yield better resolution. $R'g$ is given by

$$R'g = 0.92 (2 w_{\text{opt}})^m / \sigma \quad (2.10)$$

and $R's$ is given by

$$R's = 0.91 \lambda R m / (S \sigma) \quad (2.11)$$

where S is the slit width. The resolution of the spectrometer is determined by the smaller of the two values. Shown in Table 7 are typical values for a 1-meter spectrometer with 1200 1/mm and 133.6 1/mm gratings.

TABLE 7. Resolving powers for 1200 1/mm and 133.6 1/mm gratings.

Wavelength (Å)	grating (1/mm)	$R'g$	$R's$ (100 μm slits)	$R's$ (50 μm slits)	$R's$ (10 μm slits)
50	1200	20,300	54.5	109	542
100	"	24,700	109	218	1090
200	"	30,000	218	436	2180
300	"	33,600	327	654	3270
200	133.6	6540	24.3	48.6	243
400	"	7960	48.6	97.1	486
1000	"	10,280	121	243	1214

In all cases the slit widths determine the resolution. The slits of the spectrometer are micrometer adjustable from 500 to 10 μm . The best intensity/resolution combination is achieved with matched entrance and

exit slit widths. Eliminating λ from both sides of Eq. (2.11) indicates that the resolution $\Delta\lambda$ is independent of wavelength or is simply

$$\Delta\lambda = S \sigma / (0.91 R m) . \quad (2.12)$$

The measured instrumental resolution as a function of spectrometer slit width is compared to that given by Eq. (2.12) in Table 8. The experimental values are for oxygen K x-rays from MgO, which have a natural width of 0.11 \AA^{51} . The details of the experimental procedure are presented in section C of this chapter.

TABLE 8. Comparison of theoretical and experimental resolution.

Slit Width (μm)	$\Delta\lambda$ (\AA , measured)	$\Delta\lambda$ (\AA , Eq. (2.12))
200	1.78	1.83
140	1.18	1.28
100	0.93	0.92
50	0.45	0.46
20	0.24	0.18
15	0.18	0.14

Both the predicted values of dispersion and resolution are used to determine the stepping interval for the spectrometer when an exit slit assembly is employed. For example, when observing a 100 \AA line at 0.9 \AA resolution, the spectrometer can be stepped in increments of 5 mils per channel, since $d\lambda/dX$ at $X=6.400$ is 0.035 \AA/mil , then $\Delta\lambda/(d\lambda/dX)$ equals 25.7 mils, so that 5 mil increments will result in a peak width

of 5 channels. Experience has shown that a FWHM of a minimum of 3 channels is necessary for a meaningful fit⁵².

In addition to the remarks about reflectivity in Chapter I, additional concave grating properties of astigmatism and blaze angle must be addressed. Astigmatism is the major aberration of a concave grating and is most severe at grazing angles of incidence⁴. Astigmatism results in a point source located on the entrance slit being imaged into a vertical line. Since the vertical image is parallel to both slits and ruled lines on the grating, astigmatism, fortunately, does not degrade the resolution of the spectrometer but does cause a significant loss of intensity in the spectral image.

The length of the astigmatic image z is given by⁴

$$z = (l \cos \beta / \cos \alpha) + L (\sin^2 \beta + \sin \alpha \tan \alpha \cos \beta) \quad , \quad (2.13)$$

where l is the vertical length of the object slit, and L is the length of the ruled lines illuminated. For the present application, l was set to 10 mm, and the 14.2 mm grating mask limited L to 16.2 mm. A plot of z versus X resulted in a near linear relationship with $z = 12.76 X + 16.65$. The value of z varied from 47.1 mm at $X = 2.40$ to 163.3 mm at $X = 11.50$. These values are in fair agreement with the prediction given in figure 7 from reference 47 where z is shown to vary from approximately $2L$ to $10L$ when $\alpha = 87^\circ$.

The advantage of a blazed grating is that it concentrates specular reflection from the nonusable zeroth order into the first order diffraction pattern. This feature enhances the absolute efficiency of the grating for wavelengths reflected at or close to this blaze angle.

The wavelength corresponding to the maximum intensity is approximated by Eq. (2.1) when $\beta = 90^\circ - \psi$ and $\psi = \phi + 2\theta_b$ where θ_b is the blaze angle. The relative intensity of a blazed grating falls off to one-half its peak intensity at approximately two-thirds the blaze wavelength at short wavelengths and at approximately twice the blaze wavelength at longer wavelengths⁴⁹. Another significant advantage of a blazed grating is its ability to reduce higher order reflections⁵³. This is especially true when the incident radiation falls at a wavelength greater than the blaze wavelength. The higher order reflections of fluorine and oxygen K x-rays are shown in a spectrum of hydrated LiF in Fig. 7. This figure is a typical soft x-ray test spectrum obtained with a 1200 l/mm grating, 100 μ m matched slit widths, and a channel electron multiplier (CEM) detector. The blaze wavelength at 20.3 Å is also shown.

The measurements led to two conclusions about the ratio of high order to first order reflections. For wavelengths less than the blaze wavelength, this ratio was greater than 0.1. For wavelengths greater than the blaze wavelength, the ratio was considerably less than 0.1. In fact, second order reflections of lines off the 1200 l/mm grating for wavelengths greater than 50 Å were rarely detected. The significance of this feature is that second order reflections had no detrimental effect on the beam-foil data of interest.

An entirely different diffraction pattern is given by the 133.6 l/mm grating. Shown in Fig. 8 is a C K x-ray spectrum where the first through twelfth order reflections are significant. The blaze wavelength under these conditions is predicted to fall at 482 Å, although the diffraction pattern appears to peak between 350 to 400 Å.

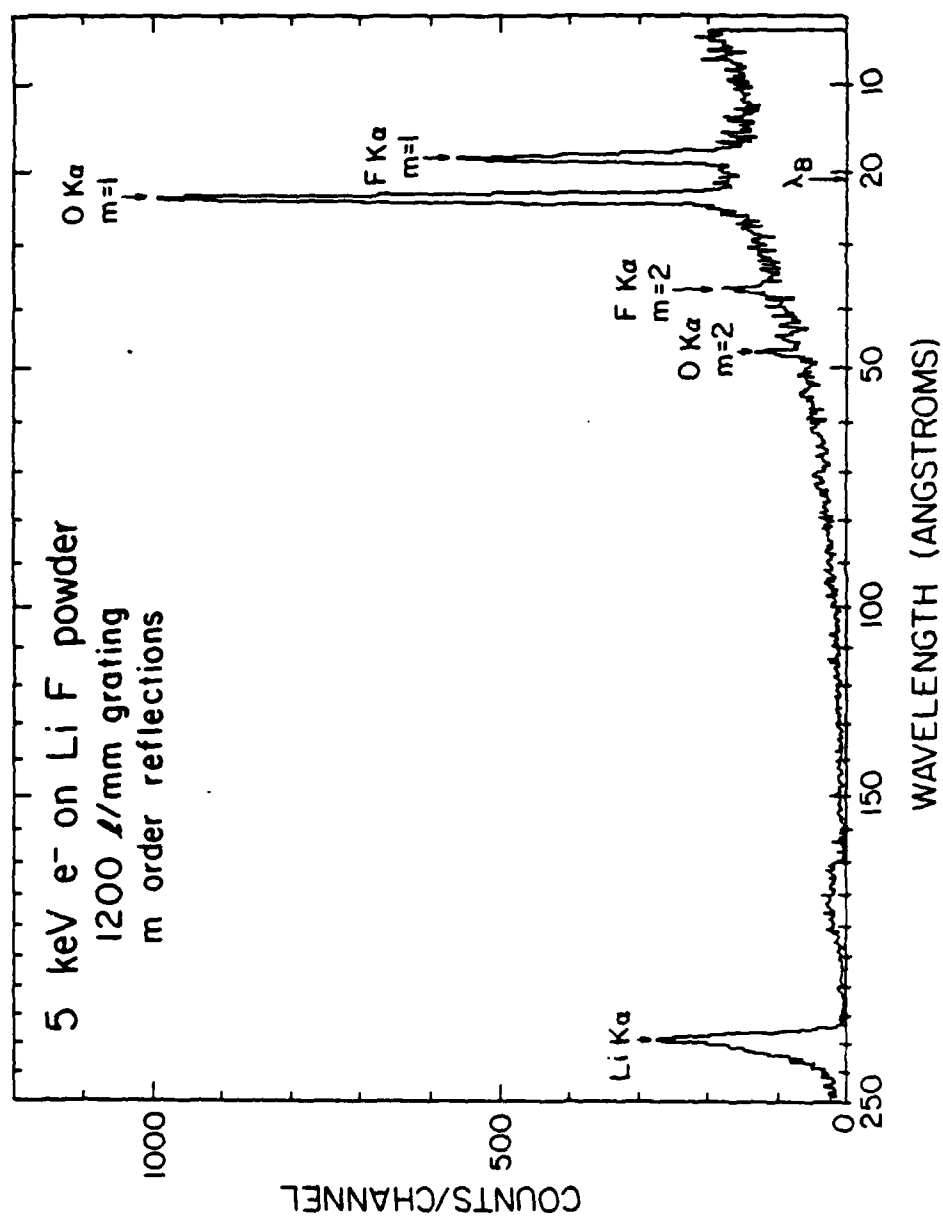


Fig. 7. Soft x-ray spectrum of solid LiF obtained with a 1200 $\text{\AA}/\text{mm}$ grating, channel electron multiplier detector, and 100 micron slit widths.

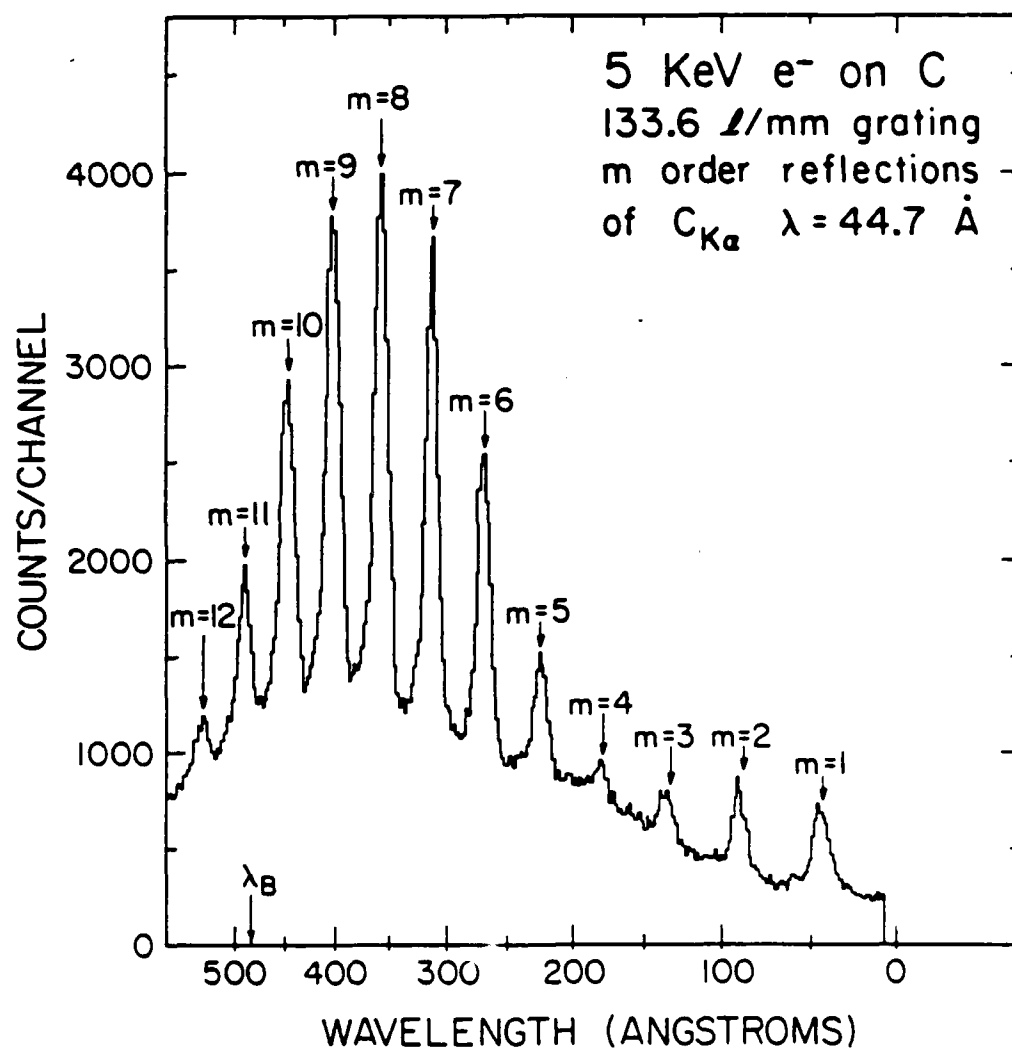


Fig. 8. Soft x-ray spectrum of solid carbon obtained with a 133.6 $\text{\AA}/\text{mm}$ grating, channel electron multiplier detector, and 100 micron slit widths.

Overlapping multiple orders of low wavelength lines seriously degrades use of this grating at wavelengths below the blaze wavelength unless other measures, such as filters, are used. For this reason, the 1200 l/mm grating was used almost exclusively throughout this work.

B. Spectrometer System Adaptation

The Minuteman Model 310GM one-meter grazing incidence spectrometer was adapted for in-beam use by mating it to a multipurpose vacuum chamber and to a Leybold-Heraeus Turbovac 150 turbo molecular pump. Fig. 9 displays the top and aft views of the essential components of the system. All chambers, valves, and bellows were made from stainless steel. The flanges for the multiple ports were made from aluminum or brass to accommodate electrical feed-throughs, target assembly rods, vacuum gauges, etc. A large glass port in the target chamber lid allowed the observation of the ion beam on a phosphorescent ZnS coated aluminum foil during the focussing process. The target chamber was designed to keep the target close to the entrance of the spectrometer at a position 50.8 mm from the entrance slit.

Ultra high vacuum copper metal seals were used to couple the turbo pump to the spectrometer and target chamber. Shut-off valves between the target chamber and spectrometer allowed the target chamber to be brought up to atmospheric pressure without disturbing the vacuum in the spectrometer. A flange clamp design was used to attach the O ring type flanges.

C. Soft X-Ray Source

Alignment and calibration of the spectrometer was accomplished off-line with a Manson Ultra-Soft X-Ray Source⁵³. To provide the x-ray anode a direct view of the entrance slit as shown in Fig. 9, the source was mounted on a port oriented 45° with respect to the spectrometer vertical. This situated the x-ray anode 76.2 mm from the entrance slit. The x-ray gun was supplied with a number of anodes of Al, Mg, O, C, and B to give x-rays with photon fluxes of the order of 10^{10} - 10^{11} photons per second per steradian. A number of additional anodes were fabricated from metals such as copper and iron. A versatile anode was made to hold thin metal foils, such as Be and Zr. In addition, many elements could be excited with electron bombardment of dry films made from chemical powders. The best films were made of a milk of magnesia slow-drying slurry. Other films were either water based or amyl acetate based, as suggested by J. E. Manson⁵³. In this way, LiF, NaF, Al_2B_3 , AlN, SiC, Si_3N_4 , B, Be, SrF, SrO, and YO were examined.

All soft x-ray tests were made with an anode potential of +5000 volts. This high a potential may seem to be excessive in exciting photons of 50 - 200 eV, but as pointed out in references 49 and 54, the use of a lower electron energy would result in a shallower electron penetration depth with a corresponding reduction in x-ray intensity. Spectrometer parameters associated with a number of soft x-ray calibration lines are given in Table 9.

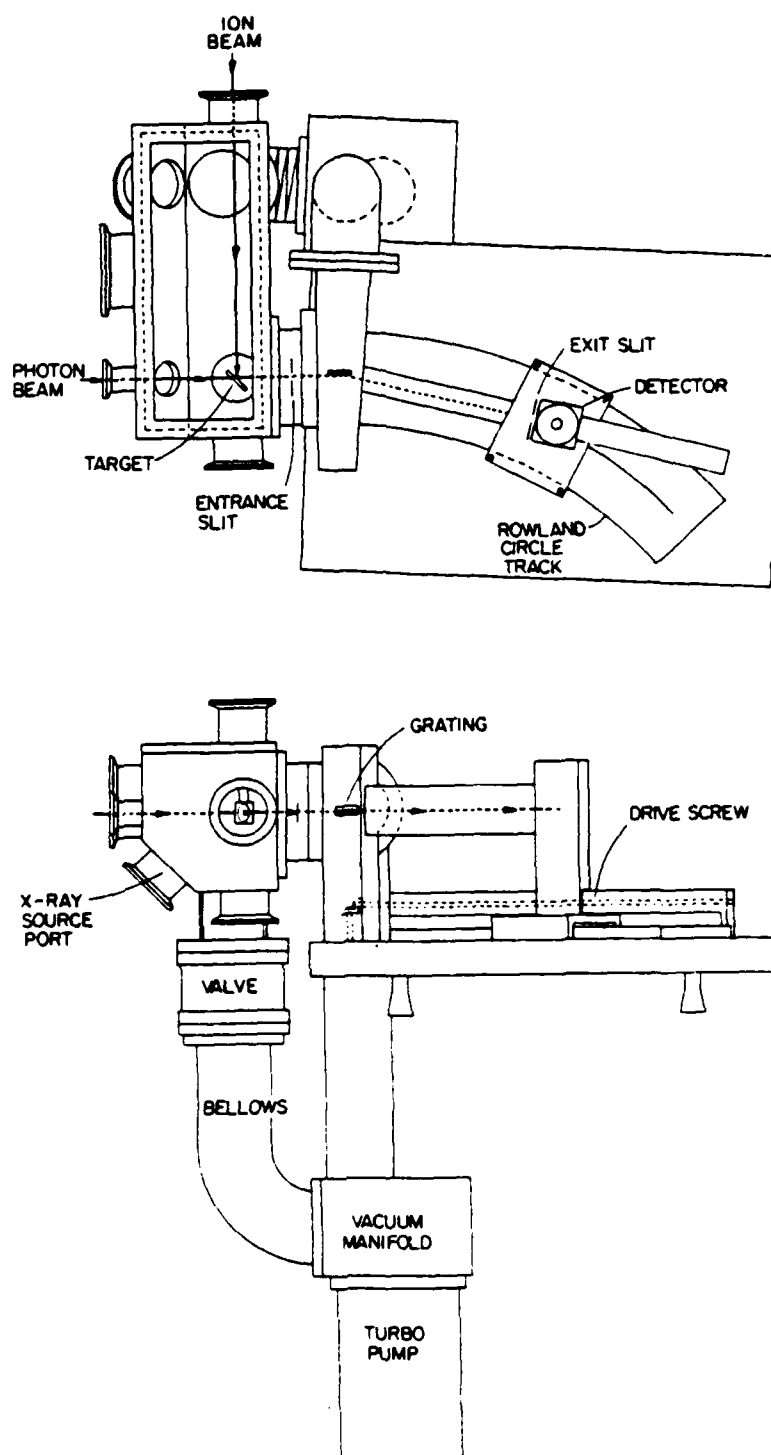


Fig. 9. Top and aft views of the in-beam grazing incidence spectrometer system.

TABLE 9. Soft x-ray lines, spectrometer positions, wavelengths, energies, and widths measured with 100 μm slits.

Element/line	X (in.)	Wavelength (\AA)	E (eV)	FWHM (\AA)
Al $K\alpha$	2.706	8.34	1487	0.9
Mg $K\alpha$	2.810	9.89	1254	0.9
Na $K\alpha$	2.940	11.91	1041	0.9
Cu $L\alpha$	3.029	13.34	929	0.9
Fe $L\alpha$	3.278	17.59	705	0.9
F $K\alpha$	3.319	18.32	677	0.9
Cr $L\alpha$	3.499	21.64	573	0.9
O $K\alpha^*$	3.602	23.62	525	0.9
Cu $L\alpha^*$	3.757	(2x13.34)	-	0.8
N $K\alpha^*$	3.991	31.6	392	0.9
Fe $L\alpha^*$	4.154	(2x17.59)	-	0.8
F $K\alpha^*$	4.215	(2x18.32)	-	0.8
C $K\alpha^*$	4.556	44.7	277	1.3
O $K\alpha^*$	4.657	(2x23.62)	-	0.8
B $K\alpha$	5.402	67.6	183	1.5
Zr $M\zeta$	5.875	82.1	151	1.3
Y $M\zeta$	6.217	93.4	133	2.5
Sr $M\zeta$	6.661	109	114	2.5
Be $K\alpha$	6.797	114	109	4.9
Li $K\alpha$	9.364	228.3	54.3	5.2

*Second order reflections.

D. Vacuum System

The vacuum system was designed to operate in the low 10^{-6} torr region. A vacuum of 10^{-6} torr provides for the safe and clean operation of the soft x-ray source. The cathode filament easily burns out at vacuum levels higher than 10^{-5} torr, and carbon contamination limits the use of the anode and the safe operation of channel electron multipliers or microchannel plate detectors, as described in the next section. This vacuum is necessary to prevent damaging ion-feedback when operating these detectors at high voltage. Oil contamination of the grating surface and detectors must also be avoided and is best

accomplished by the choice of a liquid nitrogen trapped diffusion pump, a cryo pump, or a turbo molecular pump. A 140 l/sec turbomolecular pump was available and chosen for this system due to its compact size and trouble-free mode of continuous operation. Air cooling achieved by a small fan mounted to the bearing housing allowed operation without cumbersome cooling water.

It soon became apparent that prudent handling techniques would have to be followed to achieve the vacuum system goal (i.e. 10^{-6} torr) with such a small pump. Excellent vacuum guidance is given in reference 55. The size of the pump required depends upon the ultimate vacuum desired, P , and the outgassing load of its components, Q_i . This is expressed by the equation

$$S = \sum Q_i A_i / P \quad (2.14)$$

where S is pumping speed in a leak tight system, and A_i represents the respective surface area of its components. For the 12 liter system shown in Fig. 9, the two main components are the 7000 cm^2 metal surface area of the chambers and the 200 cm^2 exposed O ring surface area. As the surfaces clean up, the outgassing rates⁵⁶ fortunately decrease with time. These rates are shown in Table 10.

TABLE 10. Outgassing rates for vacuum system components.

Surface	Qi (mbar l s ⁻¹ cm ⁻²)		
	1 hr	3 hrs	5 hrs
Buna O rings	3x10 ⁻⁶	1.5x10 ⁻⁶	1.0x10 ⁻⁶
Viton O rings	4x10 ⁻⁷	2.0x10 ⁻⁷	1.5x10 ⁻⁷
Stainless Steel	9x10 ⁻⁸	3.5x10 ⁻⁸	2.5x10 ⁻⁸
Aluminum	6x10 ⁻⁹	--	--

Use of Eq. (2.14) with the outgassing loads given in Table 7 convinced us to use Viton O rings and to expect greater than 5 hours initial pumpdown to achieve low 10^{-6} torr. Once this vacuum was achieved, it was found that subsequent pumpdowns to low 10^{-6} torr could be accomplished within one hour if the system was brought to atmospheric pressure with dry nitrogen for a time of less than one hour and roughed back down with a LN₂ trapped backing pump.

To minimize the pumping load on the turbo pump when the system was connected to the cyclotron beam line, a water cooled Alcatel 700 l/sec diffusion pump was mounted just upstream from the target chamber. All beam-foil measurements were made with this configuration and the valve from the target chamber to the turbo pump was kept closed. The target chamber was evacuated by the upstream diffusion pump, and the only exposure of the spectrometer to the target chamber was through the entrance slits while a spectrum was being accumulated. In this way, the spectrometer was maintained at low 10^{-6} torr vacuum by the turbo pump while the target chamber pressure varied from high 10^{-6} to low 10^{-5} torr.

E. Detectors -- Proportional Counter

Initial tests of the soft x-ray source and grazing incidence spectrometer response were made with a small gas flow proportional counter. The proportional counter, with a $65 \mu\text{g}/\text{cm}^2$ window of thin stretched polypropylene, held a 1.5 cm^3 volume of P-10 gas (90% Argon-10% Methane) at atmospheric pressure. Although other proportional counter refinements could be made to achieve better results in detecting soft x-rays, such as operating at subatmospheric pressures with different gases and windows, these refinements were not used since we later replaced the proportional counter with a low-noise channel electron multiplier.

This proportional counter proved adequate for observing soft x-radiation from the C K (44.7 \AA) line up to the short wavelength limit of the spectrometer at the Al K (8.34 \AA) line. During these initial tests, it was found that the reproducibility of line position was achieved only when the spectrometer was scanned in the same direction. As a result of this, a convention was adopted whereby all data was taken in increments of increasing energy or decreasing values of wavelength.

The reproducibility of the exit slit position was determined by repeated scans. The position was verified by a depth gauge measurement from the end of the exit slit/drive screw housing. The exit slit position was reproducible within 0.5 mils. However, a backlash error of 2.5 to 3.0 mils would occur if the spectrometer was not stepped approximately 5 to 10 mils beyond the starting position and brought

back to the starting position in the same direction of the next scan, due to the contact tolerance of the worm gear drive mechanism.

A least-squares peak fitting analysis using the program Facelift⁵⁷ (employing Voigt functions) was used to fit the soft x-ray data. It was found that the peak position of Cu $L\alpha$ could be reproduced to within a wavelength uncertainty corresponding to a 0.6 mil chord variation.

The efficiency of a proportional counter depends upon two variables: the energy dependent transmission through the thin foil entrance window and the absorption in the counter gas. When operated at one atmosphere, 100% of the soft x-rays are absorbed so that the efficiency is determined entirely by the transmission through the window. For carbon, the K shell absorption edge occurs at 43.7 Å. The resulting transmission efficiency for a thin 1 μ m polypropylene window is less than 10% for photon wavelengths between 43.7 Å and 30 Å. The transmission efficiency is also less than 10% for photon wavelengths greater than 115 Å as the absorption of soft x-rays increases exponentially with decreasing energy.

F. Detectors -- Channel Electron Multiplier (CEM)

The common choice of detector for beam-foil spectroscopy in the EUV and soft x-ray regions is a windowless low noise channel electron multiplier (CEM) operated in a pulse saturated, pulse-counting mode. The detection efficiency for CEM's have been measured by a number of workers⁵⁸⁻⁶². These values generally vary from 3% to 12% in the wavelength range from 44 Å to 400 Å. The spectra shown in figures 7 and 8 were taken with a Galileo Model CEM-4039 mounted behind a 100

micron exit slit. Both spectral scans were made with a chordal increment of 10 mils per wavelength interval (channel). The LiF and Carbon spectra took 58 and 50 minutes, respectively, to accumulate.

The electronic signal processing was accomplished in the following manner. The CEM was operated at a negative bias of 2700 volts. Fig. 10 shows a schematic configuration for the electronic arrangement. Signals from the CEM were shaped and amplified by a Canberra 2006E charge sensitive preamp and an Ortec 571 spectroscopy amplifier set with a 2 μ sec time constant. The shaped signals sent to an Ortec 551 timing single channel analyzer (TSCA), where a wide energy window was set about the pulse saturated signal. The output of the TSCA was directed to a spectrometer control system and from there the counting signals were sent to either a Multichannel Pulse Height Analyzer or through a CAMAC interface into the VAX 11/780 computer. Current digitized monitor signals, from either the electron excited target emission current or, for beam-foil excited ions, the charge collected in a shielded Faraday cup located 20 cm downstream, were sent to the monitor portion of the spectrometer control system. When the manually preset number of monitor counts were collected, the spectrometer was automatically advanced a preset number of steps to the next counting position and the analyzer/CAMAC multiscalers reset. By using a real time data acquisition program, XBASE, a continually updated multichannel spectrum was displayed on a Tektronix graphics terminal during on-line operation. A Hewlett Packard xy plotter was used to monitor the features of spectra in off-line operation.

As stated earlier, the grazing incidence spectrometer is inherently inefficient. The extent of this inefficiency can be tested

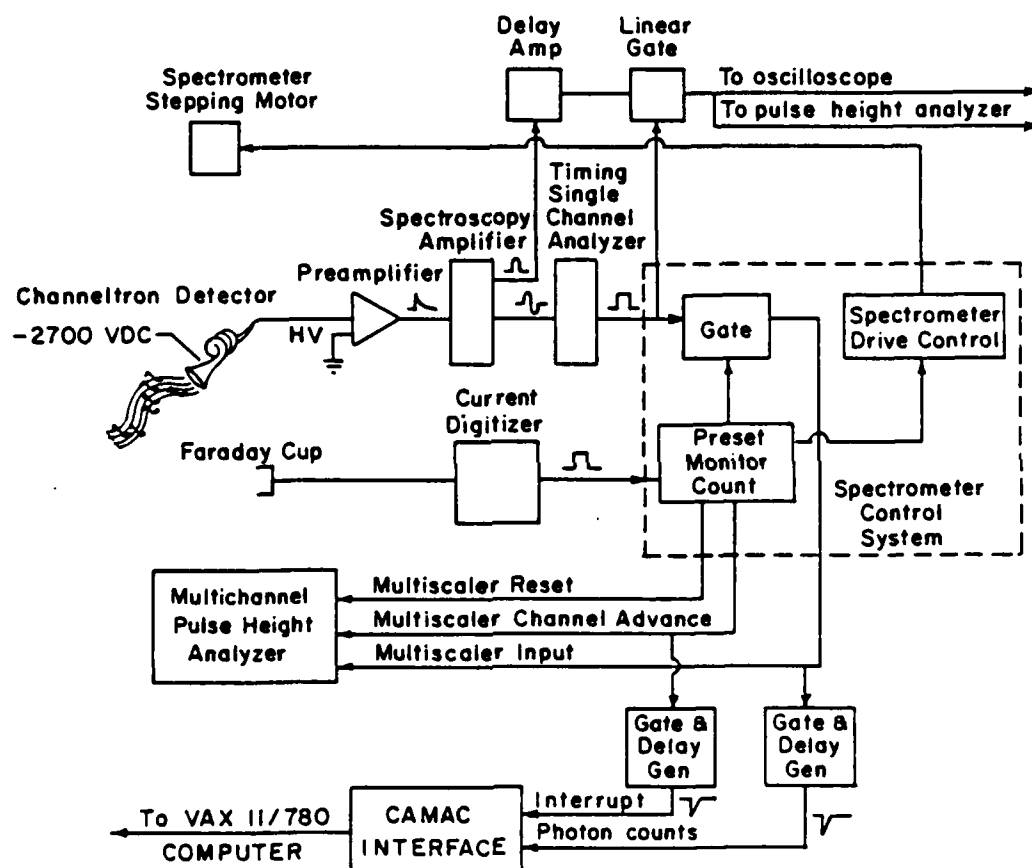


Fig. 10. Schematic diagram of the electronic configuration for the channel electron multiplier (channeltron) detector.

by observing a calibrated source with a detector of known efficiency. The Manson soft x-ray source provides a stable calibrated source of Carbon K x-rays of a specified photon rate R_x , which compares favorably with theoretical estimates for given electron excitation conditions. The observed photon counting rate N_x , which is a sensitive function of wavelength, is then given by

$$N_x = R_x (\Omega / 4\pi) (\text{Eff}_{gr} \text{Eff}_{CEM} \text{Ast}) , \quad (2.15)$$

where Ω is the detection solid angle, Eff_{gr} is the efficiency of the grating, Eff_{CEM} is the efficiency of the CEM, and Ast is the loss in efficiency due to astigmatism. When the x-ray source is operated at 5 KV and 100 μA emission current, R_x is reportedly 1.5×10^{12} photons/sec⁵³.

By substituting the following approximate values in Eq. (2.15), where $\text{Eff}_{gr} = 0.09^{14}$, $\text{Eff}_{CEM} = 0.03^{15}$, $\Omega/4\pi = 1.7 \times 10^{-4}$, and Ast = 0.01, a predicted counting rate of approximately 7000 counts per second is obtained. The above assumptions do not take into account the time dependent loss of efficiency of the grating due to surface conditions. The best experimental rate for carbon for the given conditions was 2000 counts per second at the C K x-ray peak position. This was somewhat less than that predicted by Eq. (2.15), but was of the same order of magnitude. Initial beam-foil experiments performed with the CEM detector indicated that the beam-foil light source was approximately three orders of magnitude less intense than the soft x-ray source at obtainable beam currents ($\sim 1 \mu\text{A}$). Therefore, it was deemed advisable to explore ways of improving the data collection efficiency.

G. Detectors -- Position Sensitive Microchannel Plate (MCP)

Recent reports⁶³⁻⁶⁵ of the employment of a position sensitive microchannel plate in a grazing incidence spectrometer and the resulting improvement in detection efficiency by one to two orders of magnitude motivated the development of a similar system. A Galileo 3508 chevron microchannel plate with a resistive anode encoder (RAE) was adopted for this purpose. The chevron MCP is composed of two microchannel plates that each have 25 μm diameter channels that are biased at an angle of 8° to the surface normal. To reduce ion-feedback, the plates are stacked so that the channels from one plate are biased with respect to the channels of the other plate for a total angle of 16° . The exposed area of the MCP is rectangular, 50 mm by 8 mm.

The resistive anode encoder was mounted within a ceramic plate behind the microchannel plate. Before mounting the MCP on the grazing incidence spectrometer, it was first evaluated in a test configuration as shown in Fig. 11. This cut-away drawing shows the MCP on a movable spring-loaded teflon block within an aluminum frame. The MCP was located 142 mm above the soft x-ray source and 9 mm above an adjustable slit, restricting the illumination of the plate to a 127 μm slice. The MCP could be moved across the slit by means of a micrometer positioned shaft. In this way, linearity and response of the plate could be checked.

Two methods of extracting position information from the MCP were tested. Initially, the charge division method⁶⁶ was used where signals from both ends of the RAE were summed and compared with the signal from

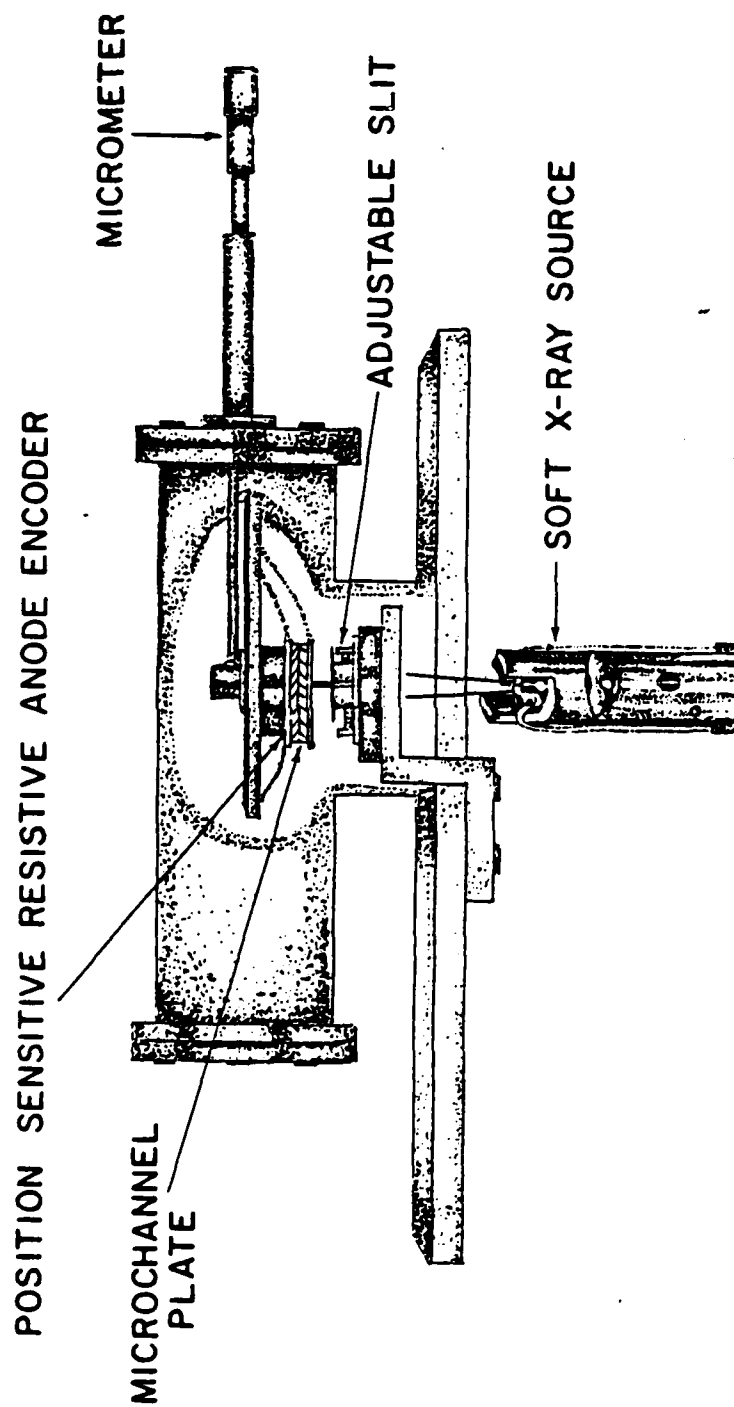


Fig. 11. Cut-away view of the microchannel plate detector on a sliding mount above an adjustable slit and x-ray source.

one of the ends. A schematic of the electronic processing circuit is given in Fig. 12. Essentially the same circuit was used for off-line measurements as for on-line beam-foil spectroscopy. The only difference between the two was the source of the current digitizer signal. This signal came from either the emission current of the x-ray gun or the charge collected in a faraday cup. These signals were used to generate a gate to the multichannel analyzer (MCA) so that the MCA would not receive signals after the preset monitor count was reached. The voltage divider network⁶⁷ was designed for use with a 0.25 ma current supplied by a 0-5 KV power supply. A negative 2000 volts input potential provided a 890 volt drop across each plate and a 220 volt accelerating potential to the RAE. Tuning the electronics for optimum operation by the charge division method was accomplished in the following manner. A 2 volt pulser signal was split and sent to each preamp. The unipolar output of each spec amp was compared on an oscilloscope and the gains of the spec amps were adjusted to give matching output pulse heights of approximately 4.0 volts. A nominal spec amp gain setting of 6 would amplify the 10 mV signal pulses from the RAE into 2-3 volt pulses, which were optimum for this charge division circuitry. After the pulser was turned off, the DC offset signal S2, as shown in Fig. 12, was set to zero volts with respect to ground by reference to a 10 mV oscilloscope reading. Next, the DC offset signal S1 was adjusted so that the DC sum signal (S1+S2) was set to zero. The DC offset adjustment and the matched gain adjustments were necessary to provide a linear response with respect to position along the MCP. Finally, the position out signal from the Ortec 464 was reduced from a 10 volt maximum to a 7.8 volt maximum signal by adding a

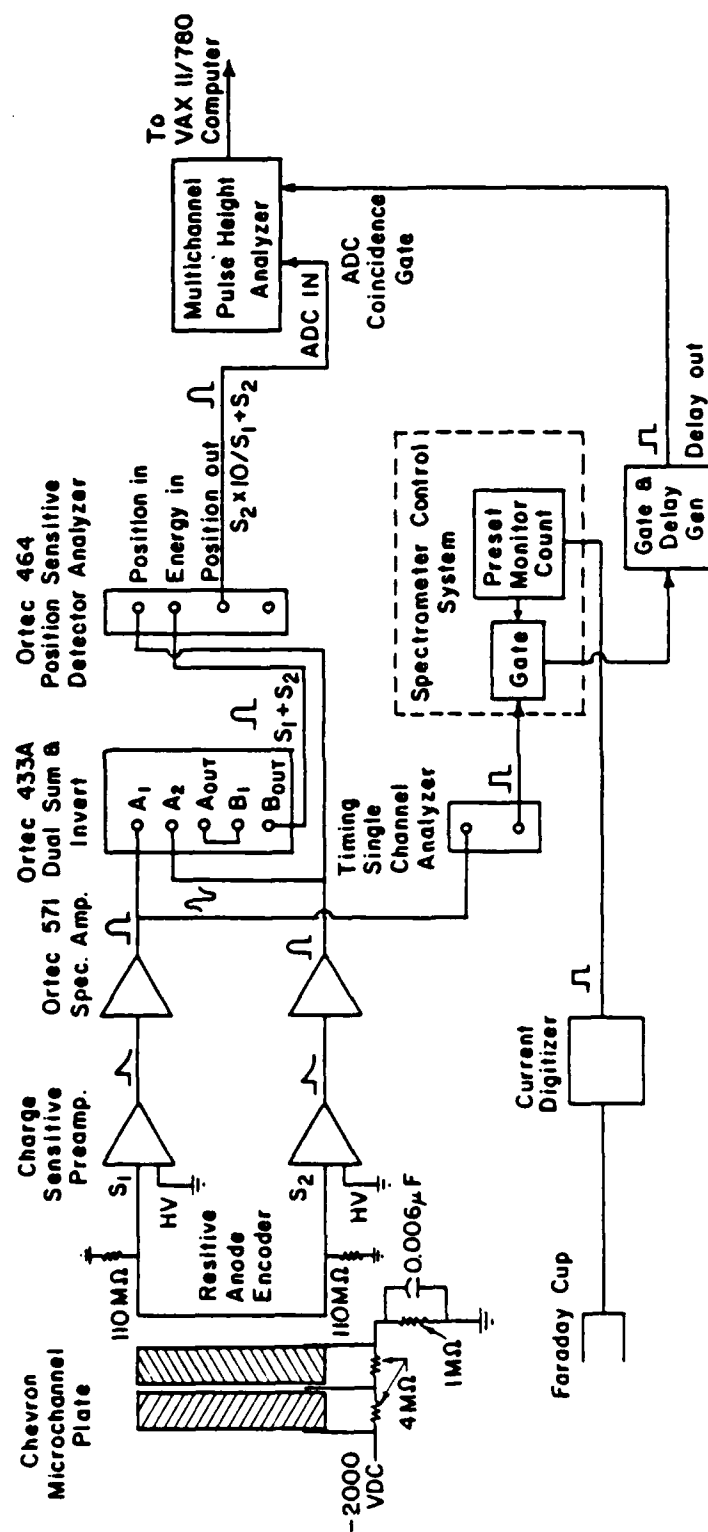


Fig. 12. Schematic diagram of the electronic configuration for the microchannel plate detector.

2.7 K ohm resistor in series. This voltage reduction was necessary to be compatible with the multichannel analyzer (8 volt limit).

The second method of position determination along the MCP consisted of comparing the relative times of the signals from both ends of the plate⁶⁸. The electronic circuit used for this rise time method was taken from reference 69. The results obtained using both methods are shown in Fig. 13. Without going to elaborate lengths to optimize the timing response of the MCP, we found that the charge division method gave much better resolution, as can be seen from the figure. Further tests of the MCP using the charge division method proved that the centroid position of the signal varied linearly (within $\pm 0.4\%$) with plate translation over the fixed slit. A least squares linear fit of plate position versus peak position is displayed in Fig. 14. Carbon K x-rays were directed through the 50 micron slit and were detected by the MCP as shown by the accumulated spectrum in Fig. 15 where the MCP was moved in intervals of 0.025" after a 15 sec exposure. Repeated measurements revealed that the intensity varied by as much as $\pm 10\%$ and that a position resolution of 200 microns could be achieved. This width was approximately three times the manufacturer's ultimate resolution value of 60 microns but proved adequate for the resolution capabilities of the spectrometer above 0.5 Å.

As shown in Fig. 16, the MCP was next attached to a rotatable mount designed to replace the exit slit assembly on the grazing incidence spectrometer. This configuration enabled the simultaneous detection of all wavelengths over a finite wavelength range determined by the 50 mm length of the MCP. As the original spectrometer bellows, designed for the exit slit assembly, had only a one-inch inner

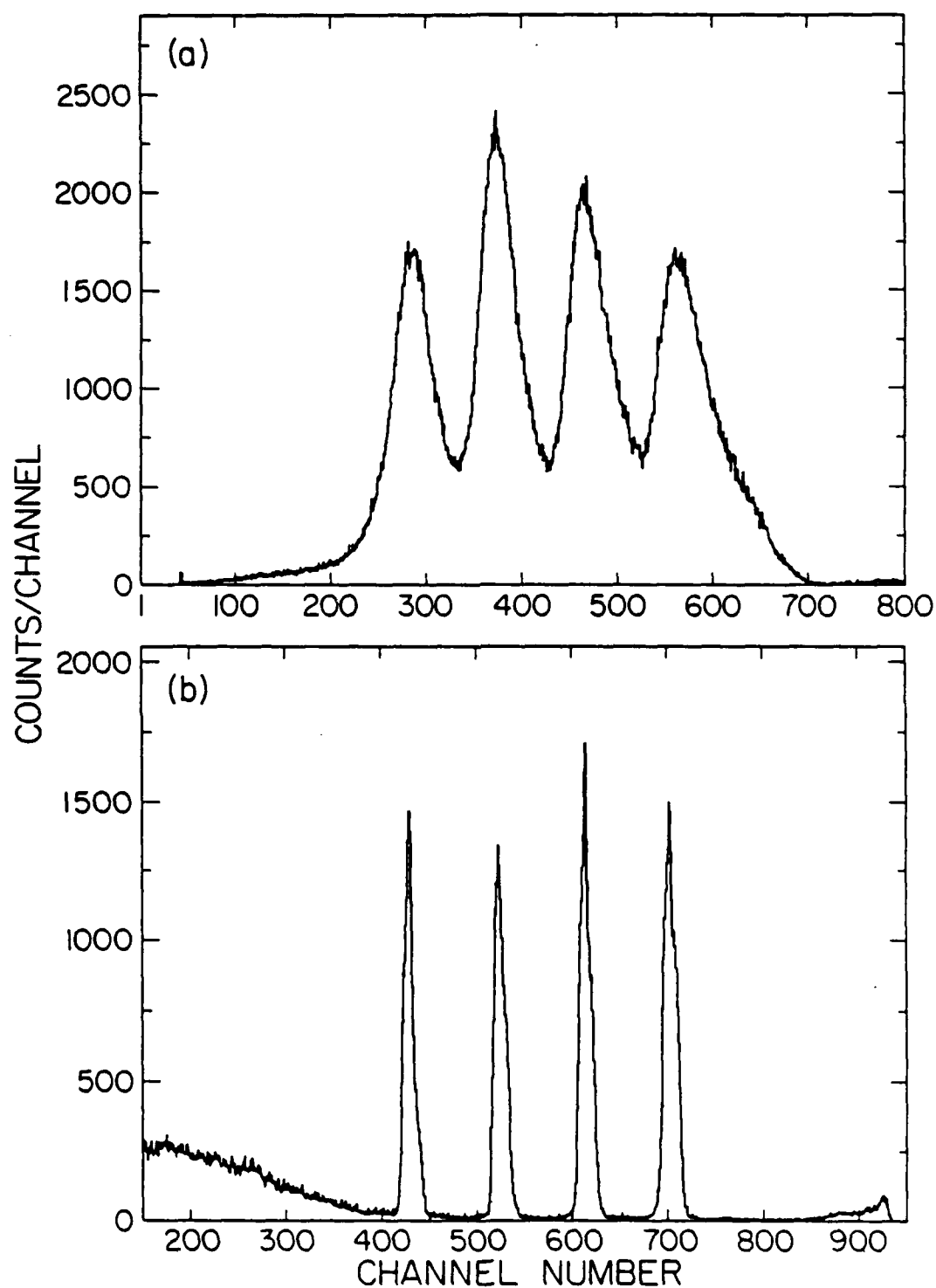


Fig. 13. Comparison of two methods in electronically determining photon position on the microchannel plate.

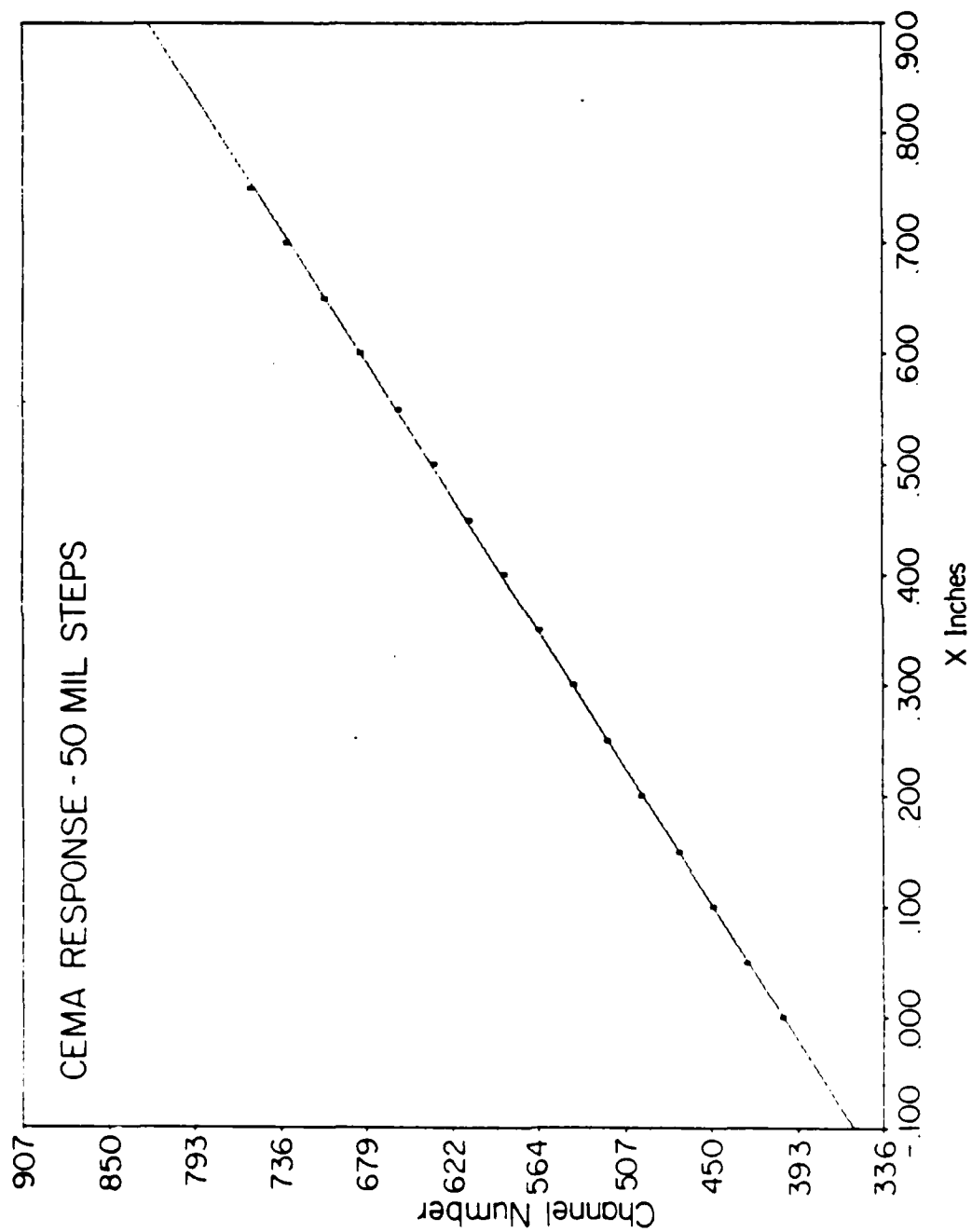


Fig. 14. Least squares linear fit of MCP (CEMA) position versus peak position.

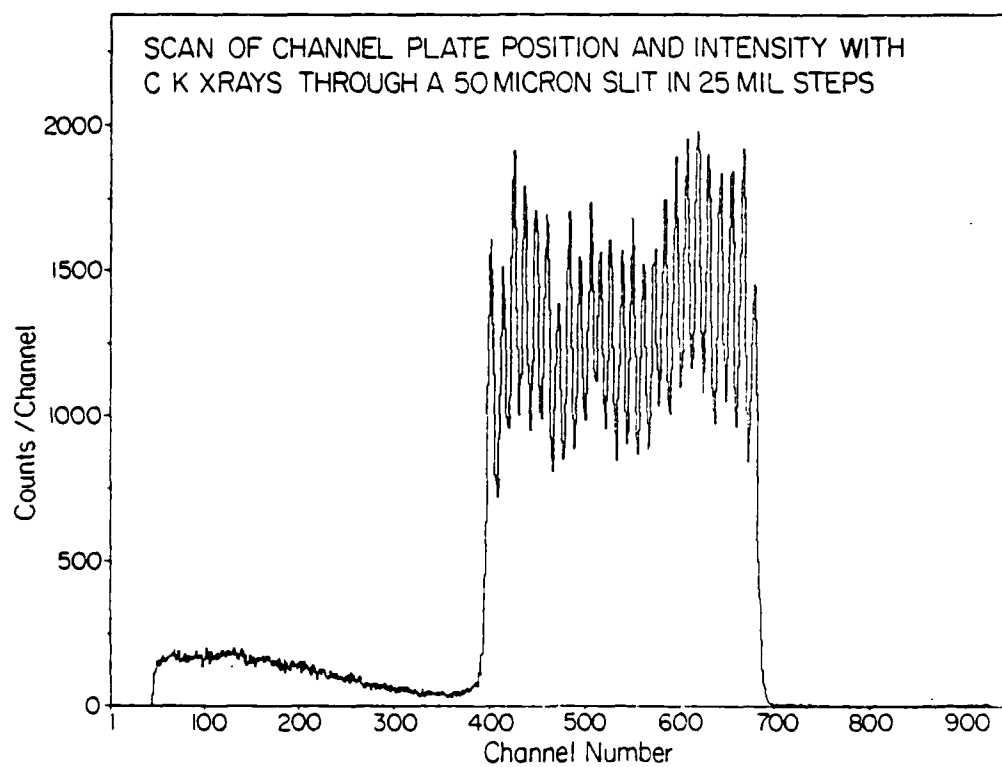


Fig. 15. Position scan as in Fig. 13 (b) but with carbon K x-rays and through a 50 micron slit.

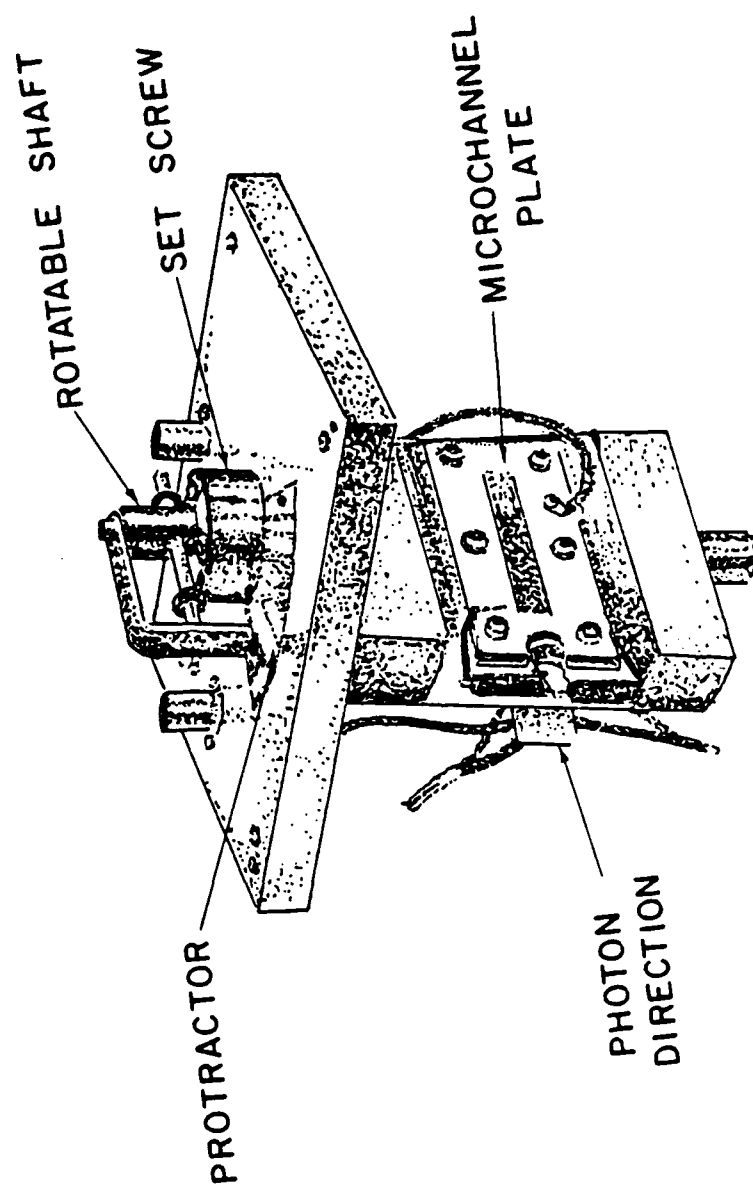


Fig. 16. Microchannel plate configuration for the grazing incidence spectrometer.

diameter, it was soon realized that the orientation of the MCP square aluminum housing was critical. To prevent shadowing of the plate along the full operational range of the detector on the curved Rowland circle track, the housing had to be rotated 10° from its original tangential alignment. The geometry of the arrangement is shown in Fig. 17.

The MCP was positioned so that the center of the face was located on the Rowland circle where the angle of incidence θ , the Rowland circle radius $R/2$, and the length of the MCP plate, Y , are constants with values of 3° , 499.4 mm and 49.66 mm, respectively.

The alignment and focusing of the microchannel plate were accomplished by the following detailed procedures which apply to the Minuteman 310 GM grazing incidence spectrometer:

- 1) With the MCP housing removed, the spectrometer was driven to a counter reading of 2.053, corresponding to the zero order diffraction position at 3° . The position of the exit slit housing was determined under tension by either the load under vacuum or by a spring simulating this load so that its position was matched with the alignment dimension from Minuteman drawing no. B-850. This dimension E , as measured from the closest point on the beveled housing to the end of the Rowland circle track, was 1.679". If there was a discrepancy, the spectrometer was moved manually by rotating the drive shaft counter weight until the 1.679" dimension was obtained. Then the spectrometer odometer was reset to 2.053 by removing the motor housing and adjusting the odometer pulley.

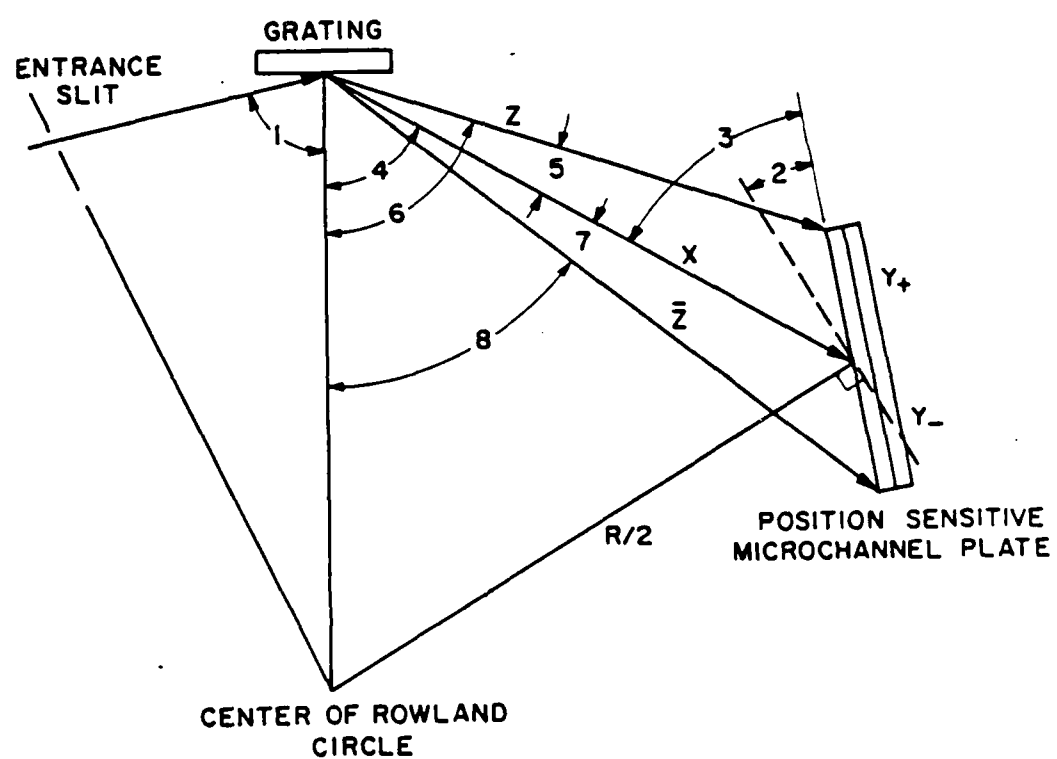


Fig. 17. Geometry of the microchannel plate with respect to the grating and the photon beam defined by the entrance slit.

- 2) The grating was put into rough alignment by positioning the fine adjustment screw a distance of 0.340" from the rear of the head of the knob to the face of the feed-through flange. A detector position which satisfied these conditions resulted in the adjustable brass lower detector positioning plate being set to distances of 0.278" and 0.280" fore and aft from the outer open side of the detector housing.
- 3) Under vacuum conditions, with the microchannel plate in place and the spectrometer set at a peak position (i.e., $X=5.875$ for $Zr\ M\zeta$), the x-ray peak position was checked against the central channel of the spectrum. The central channel number depends upon the total resistance in the cable and resistor carrying the pulse height signal into the multichannel analyser. Small adjustments of the housing fore and aft along the radius of the Rowland circle were made to center the $Zr\ M\zeta$ peak on the MCP. After this procedure, it was necessary to again adjust the grating focus to maximize the count rate in the peak and to give the detector position a final small correction to re-center the peak.

Once the MCP was aligned for a given grating, two adjustable parameters determined the wavelength range accepted by the MCP. These parameters were the chord length X and the detector surface angle with respect to a tangent to the Rowland circle (angle 2). All remaining angles and distances were then fixed by geometric expressions involving these parameters. For example, the following equations⁷⁰ permit the calculation of the wavelength of a peak corresponding to the channel number of its centroid in the spectrum:

$$m \lambda = \sigma [\sin (\text{angle } 1) - \sin (\text{angle } 6)] \quad (2.16)$$

$$\text{angle } 6 = \text{angle } 5 + \text{angle } 4 \quad (2.17)$$

$$\text{angle } 5 = \sin^{-1} [Y/Z \sin (\text{angle } 3)] \quad (2.18)$$

$$\text{angle } 4 = \cos^{-1} (X/R) \quad (2.19)$$

$$Z = [X^2 + Y^2 - 2XY \cos (\text{angle } 3)]^{1/2} \quad (2.20)$$

$$\text{angle } 3 = \text{angle } 2 + \sin^{-1} (X/R) \quad (2.21)$$

$$Y = (MD - C) Y_s \quad (2.22)$$

where all angles and distances are as shown in Fig. 15, C is the channel number of the peak centroid, MD is the channel number corresponding to the center of the MCP (typically 495 out of 1024 channels), and Y_s is the conversion factor found by dividing the MCP active length in mils (1955) by the number of channels in the pulse height spectrum (typically 820 out of 1024 channels).

Similarly, the channel number for a line of known wavelength can be predicted by the following equations:

$$C = MD + (Y)(Y_s) \quad (2.23)$$

$$Y = X \sin (\text{angle } 5) / \sin (180 - \text{angle } 5 - \text{angle } 3) \quad (2.24)$$

$$\text{angle } 5 = \text{angle } 6 - \cos^{-1} (X/R) \quad (2.25)$$

$$\text{angle } 6 = \sin^{-1} [\sin (\text{angle } 1) - (\lambda/\sigma)] \quad (2.26)$$

$$\text{angle } 3 = \text{angle } 2 + \sin^{-1} (X/R) \quad (2.27)$$

From these expressions it can be determined that, for any given setting, a one degree increase in angle 2 expands the wavelength region by approximately 6 Angstroms. Also, for a given fixed angle 2, which is the normal case, an X setting increase of one inch amounts to an

approximate 10 Angstroms addition to the wavelength range as shown in Table 11.

From a practical viewpoint, the chord length X is known to within one one-thousandth of an inch, but angle 2 is set by a protractor scale with a precision of only one degree (a protractor setting of 15° corresponds to an angle 2 setting of approximately 3°). Also, the midchannel number of the MCP, as well as the quotient of the active length of the MCP and the number of channels in a spectrum can be estimated only to a precision of 0.5% as these values are sensitive to the electronic calibration. Angle 1, although constant and set to a value of 3° , may be effectively offset by 0.1° to 0.2° by the grating focus position and the position of the MCP, which in turn may be several thousands of an inch off the Rowland circle. These small uncertainties can easily result in predicted wavelength errors of up to 0.5 \AA .

TABLE 11. Wavelength range (+/-) for values of X and angle 2.

X	Angle 2 and wavelength +/- (\AA)									
	0°		3°		4°		10°		15°	
	+	-	+	-	+	-	+	-	+	-
4.600	66.6-	20.6	76.9-	11.8	80.4-	9.2	103.0-	--	123.4-	--
5.000	79.0-	29.0	89.3-	19.9	92.8-	17.2	115.1-	3.7	134.9-	--
6.000	114.0-	53.9	124.2-	44.5	127.6-	41.6	149.2-	26.0	167.9-	15.6
7.000	154.5-	84.4	164.6-	74.8	168.1-	71.8	189.1-	55.1	207.1-	43.3
8.000	200.7-	120.5	210.8-	110.9	214.2-	107.8	234.8-	90.6	252.2-	77.9
9.000	252.6-	162.4	262.7-	152.8	266.0-	149.7	286.3-	132.2	303.3-	119.1
10.000	310.4-	210.2	320.4-	200.6	323.7-	197.5	343.7-	179.8	360.2-	166.5
11.000	374.1-	263.9	384.1-	254.4	387.4-	251.3	407.0-	233.6	423.2-	220.1
11.300	394.5-	281.2	404.3-	271.7	407.6-	268.6	427.2-	250.9	443.3-	237.4

Therefore, a more accurate calibration was used whereby the channel numbers of lines having known wavelengths were measured. It was found that the wavelength versus channel number was accurately represented by a second order polynomial to within $\pm 0.1 \text{ \AA}$. The fact that the wavelength calibration should be quadratic in channel number is not obvious. Even when Eq. (2.16) is expressed in terms of channel number, it does not directly simplify to a second order polynomial. However, when experimental values are substituted into Eq. (2.16), the resulting wavelength versus channel relationship is closely fit by a second order polynomial as seen in Fig. 18. An example of such a calibration using a number of lines with known wavelengths is presented in Chapter III.

The MCP was tested at several angle 2 settings with the soft x-ray source exciting K x-rays from Be and O from an anode composed of powdered Be in Mg(OH)_2 . Shown in Fig. 19 are spectra taken with the spectrometer slits set at $100 \text{ }\mu\text{m}$, detector set at $X = 5.200$, and angle 2 set at 5° , 15° , and 20° . It is obvious that the spectra cover a larger wavelength region as angle 2 is increased. This observation is consistent with the predictions given in Table 11 (i.e. the wavelength region increases monotonically with increasing angle 2). Two other spectral features also increase monotonically with increasing angle 2. As expected, the peak intensity increases, since the efficiency of the MCP is predicted to drop off with the cosecant of the angle of incidence⁷¹. In addition, the FWHM resolution of the peaks increase with angle 2. This is a consequence of the poorer focusing conditions for positions off the Rowland circle. At first glance, the spectra show no peak broadening and, in fact, the peaks decrease in width.

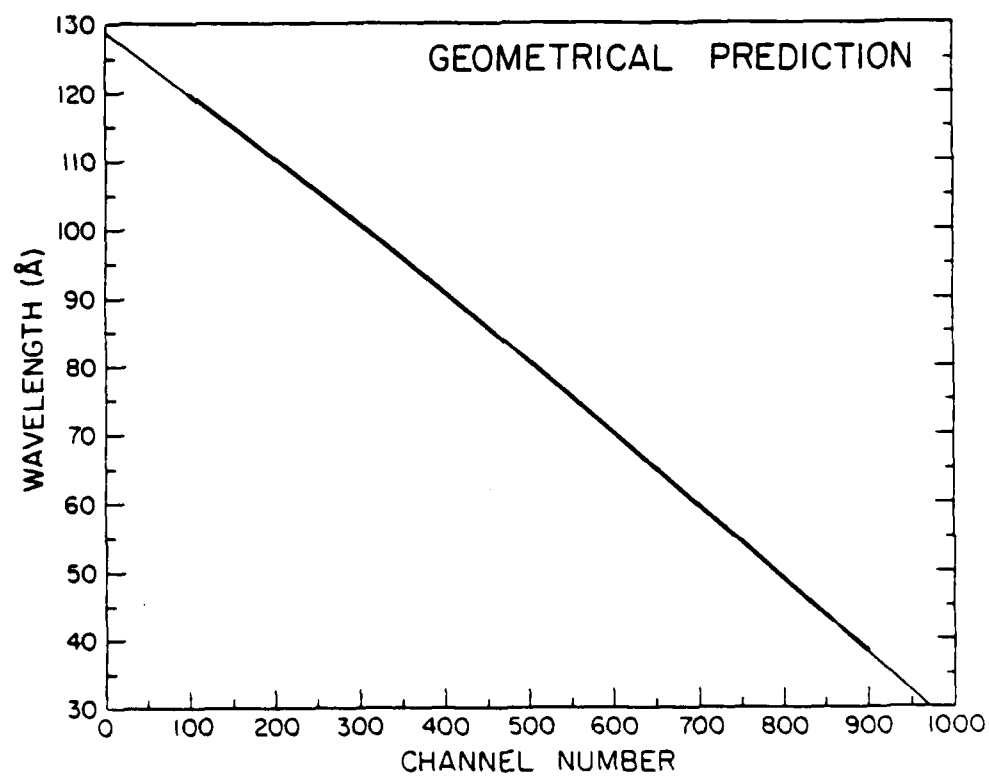


Fig. 18. Comparison of the geometrical prediction of wavelength versus channel number (heavy line) by equations (2.15) - (2.21) and the quadratic fit from the spectrum of peaks of known wavelength (light line).

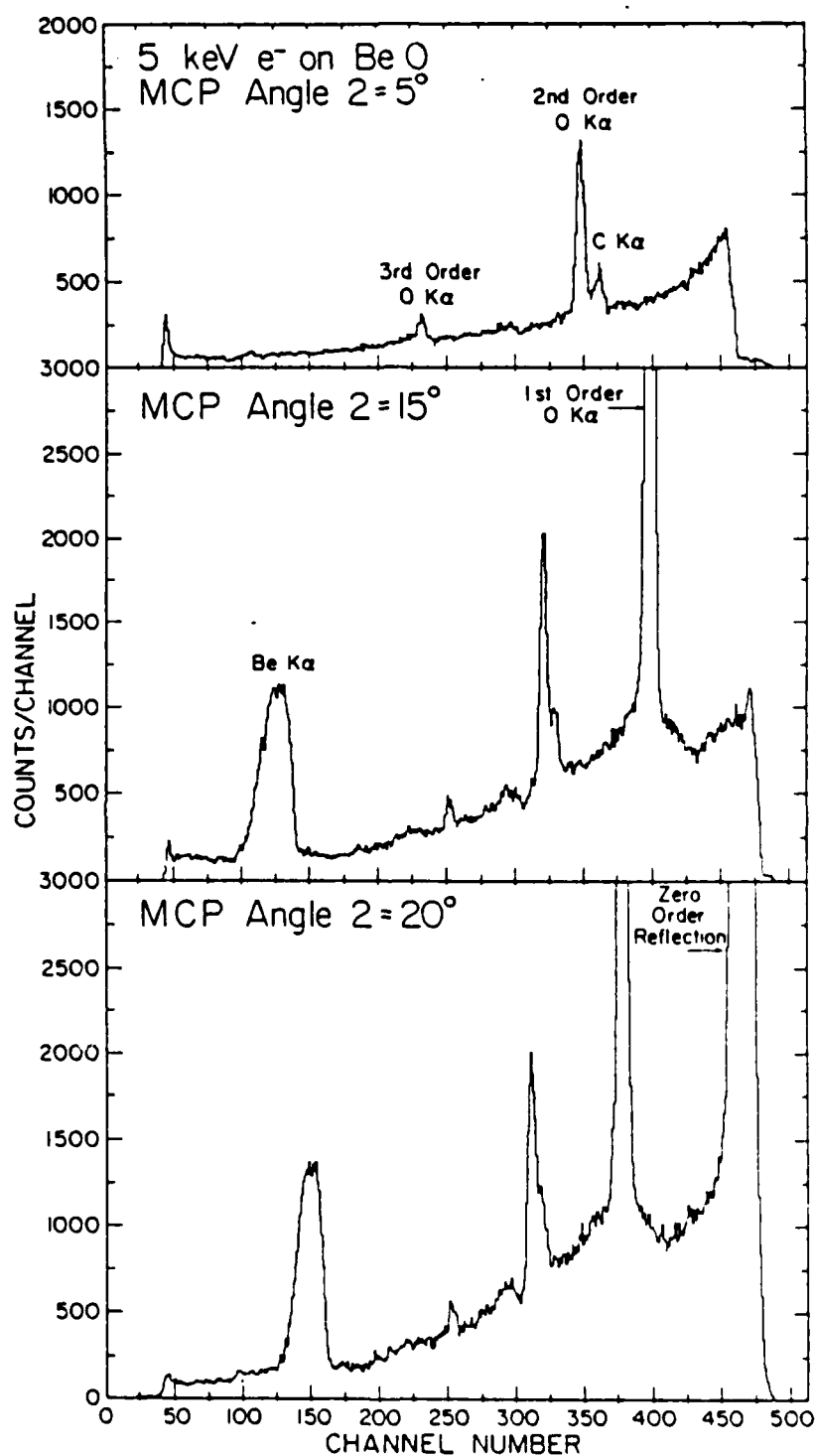


Fig. 19. MCP spectra of BeO at various values of angle 2 at a spectrometer position 5.200 and a 100 μm entrance slit.

However, the decrease in the wavelength dispersion more than makes up for this apparent peak narrowing. The effects of the angle 2 variation on wavelength range, resolution (FWHM), and relative intensity are given in Table 12.

TABLE 12. Sensitivity of the MCP angle at spectrometer position $X=5.200$ and $100\text{ }\mu\text{m}$ slit.

Angle 2 (degrees)	Wavelength Range (Å)	FWHM (Å)	Relative Intensity (arbitrary units)
2.5	94 - 30	1.18	1000
5	103 - 25	1.26	1103
10	123 - 12	1.49	1256
15	141 - 3	1.65	1381
20	161 - 0	1.95	1608

In summary, it would appear that a large value of angle 2 would be most favorable since both the wavelength range sampled and the peak intensities increase with increasing angle 2. Unfortunately, for an angle 2 greater than five degrees, the resolution of the plate deteriorates and becomes an unattractively strong function of peak position along the plate. For example, when angle 2 is set to 3° , the width of a peak increases by 0.2 Å from the center of the plate to the ends of the plate. But only a five degree increase in angle 2 above this causes the width of a peak to increase by an additional 0.5 Å from the center of the plate to the plate ends.

Measurements were also performed to determine the response function of the plate at angles of grazing incidence. To perform these measurements, it was necessary to choose a spectral line that could be seen by the MCP at both small and large X values, so that the peak

could be moved across the plate from one end to the other. The 1200 l/mm grating dictated the choice of a line with a wavelength greater than 80 Angstroms. Some elements in the second transition series were found to provide $M\zeta$ x-rays that have narrow line widths and suitable wavelengths.

Initial testing was carried out on an MCP which showed an order of magnitude variation in the intensity response across the plate. However, additional tests conducted on a new MgF_2 coated plate, where the spectrometer was stepped in even increments of 0.100 inches, showed a very regular response to Zr $M\zeta$ x-rays. This response is shown in Fig. 20. The intensity drop off above channel number 750 was due to shaddowing by the metal frame holding the MCP. This shadowing effect also accounts for a slight shortfall in the observation of the short wavelength limit predicted in Table 11.

The peak position response with spectrometer position was remarkably linear as shown by a linear fit to peak position in Fig. 21. In addition, the MgF_2 coating increased the sensitivity of the MCP over that of the uncoated plate by a factor of 5.7 at 82 Å and by a factor of 3.4 at 109 Å. Similar increases have been noted by others^{60,72}.

In order to compare the performance of the spectrometer system employing the MCP with that employing the CEM and exit slit, the following measurements were carried out:

- (1) An SrO anode was excited by a 120 micro-ampere beam of 5 KV electrons. An exit slit/CEM spectrum with 100 micron slits in steps of 0.010" per channel was recorded over the spectral region 121 Å to 21 Å. The spectrum took 4200 seconds to accumulate.

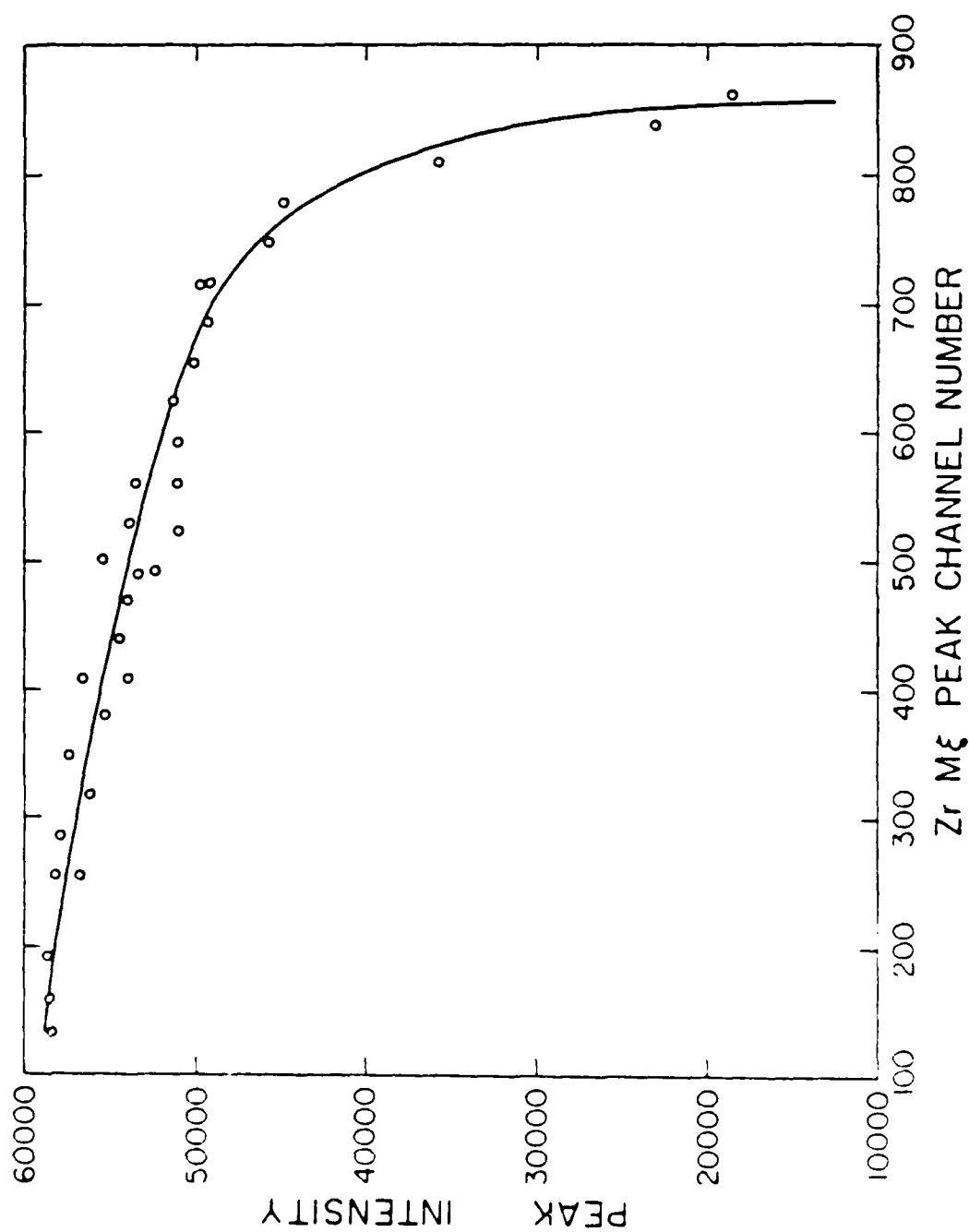


Fig. 20. Intensity response of MCP to the movement of the Zr Mg x-ray peak across the plate.

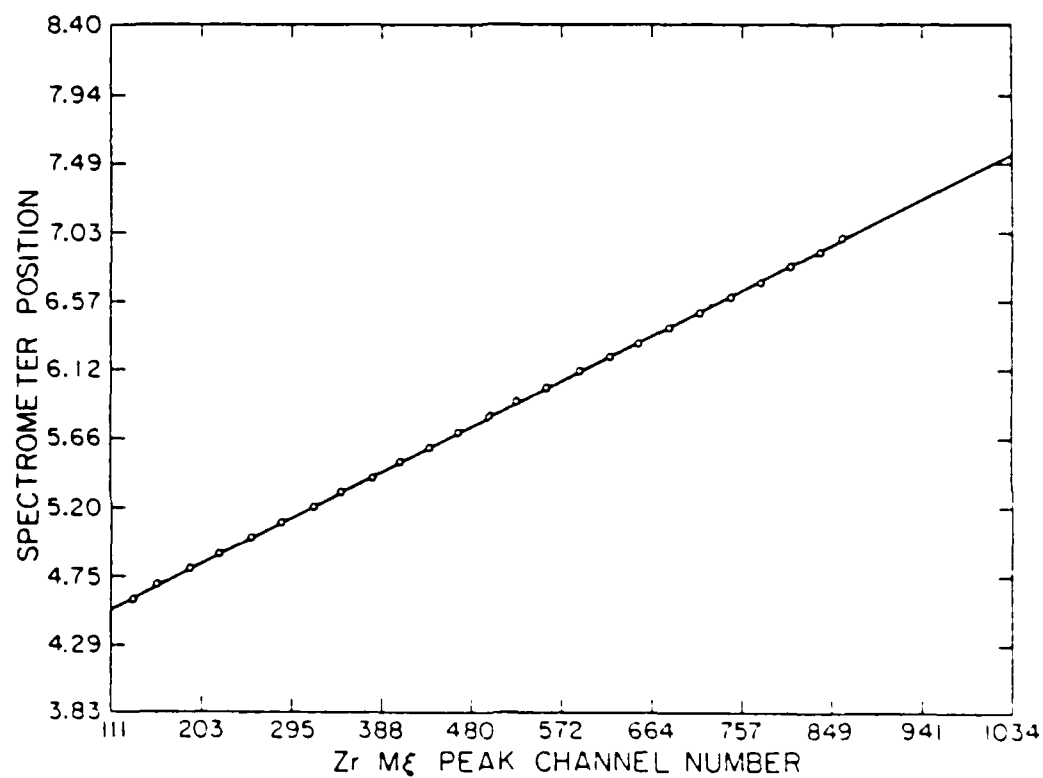


Fig. 21. Linear fit (solid line) of Zr M ξ peak centroid (circles) versus spectrometer position.

- (2) The SrO source was run again under the same conditions, but with two overlapping microchannel plate spectra, each taking 415 seconds to accumulate. Fig. 22 compares the CEM spectrum with a composite of the two MCP spectra. Given that the MCP peaks were 8.5 times as intense and that the counting time was 5.0 times less, the advantage of the MCP over the CEM and exit slit amounts to a factor of 43. If the spectral region could be covered by one MCP spectrum, this advantage could reach as high as a factor of 86.

The CEM and exit slit combination still hold a resolution advantage over the MCP. Although the MCP attains the same resolution at 100 μm slit width as the CEM and exit slit, the soft x-ray data show that the resolution is worse for the MCP at narrower slit widths. For example, at 50 μm slit width, the MCP achieves only a 15% improvement in resolution but at the cost of a 50% reduction in intensity. No further improvement in resolution was apparent by reducing the slit width further. By contrast, the CEM and exit slit resolution improved as predicted by Eq. (2.12) with narrower slit width settings. Additional MCP features as they relate to beam-foil spectroscopy are given in Chapter III and Chapter IV.

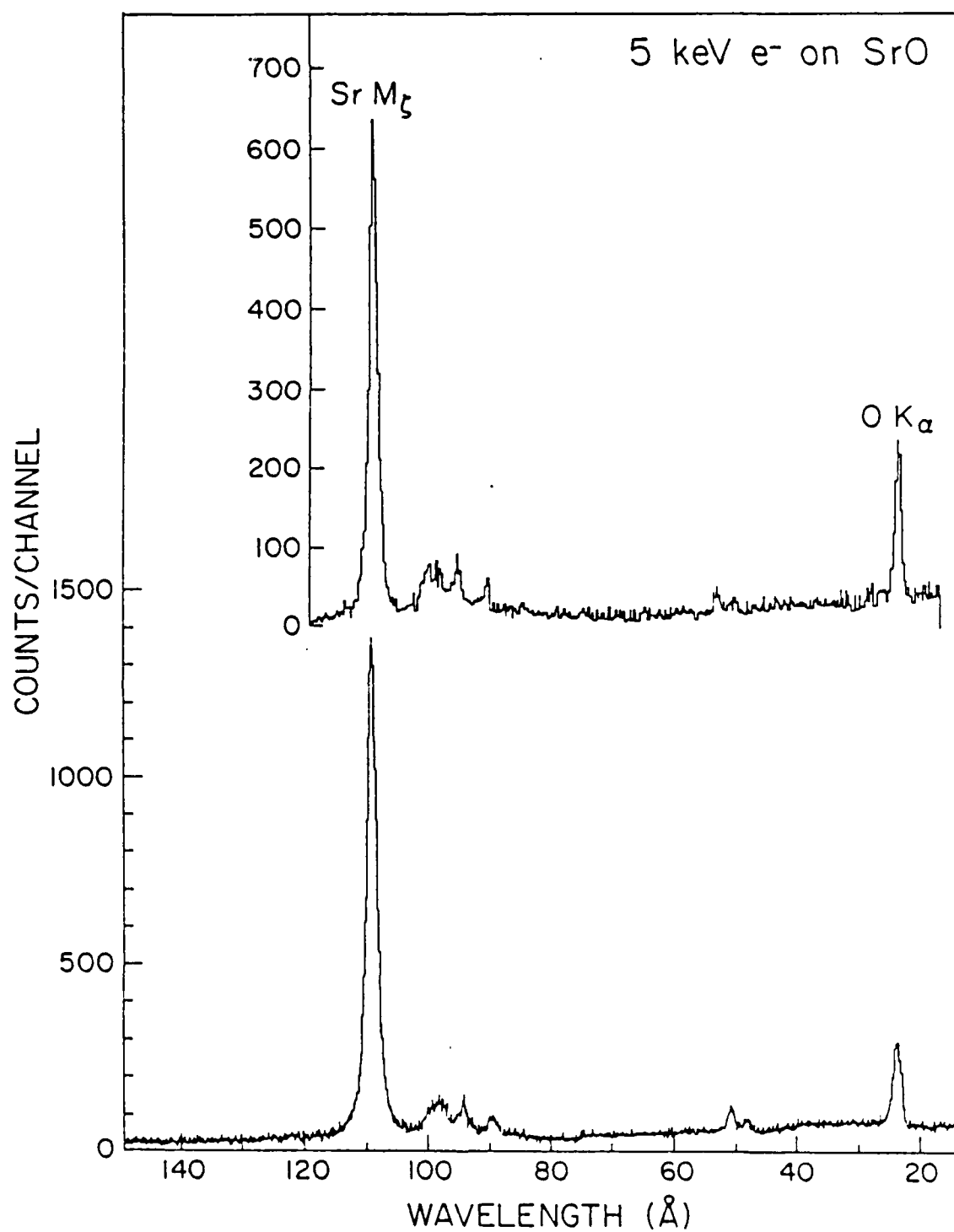


Fig. 22. Comparison of a SrO M₅ spectrum acquired with a CEM detector over 70 minutes (upper spectrum) with a composite of two MCP spectra of 7 minutes each (lower spectrum).

CHAPTER III

ONE-, TWO-, AND THREE- ELECTRON NEON EUV MEASUREMENTS

A. Background

Highly ionized neon was selected for detailed beam-foil study for the following reasons:

- (1) the neon transitions to the $n=3$ and $n=2$ levels fall in the EUV region from 350 to 45 Å.
- (2) the availability of an intense 40 MeV Ne^{+3} cyclotron beam made possible the examination of more highly ionized states than had been studied previously with lower energy ion beams.
- (3) the known wavelengths of many Li-like, He-like, and H-like neon lines furnished an excellent check of the wavelength calibration of the present experimental apparatus.
- (4) reported lifetime measurements of some Li-like and He-like lines provided a means of checking the accuracy of the foil translation device and the decay curve analysis procedure.

Initial beam-foil measurements of 40 MeV neon were carried out with a 1200 l/mm grating blazed at 1 degree and an exit slit/CEM detector arrangement as shown in Fig. 2, Chapter I. The device shown in Fig. 11, Chapter II, was converted into a foil translation mechanism by removing the fixed slit assembly and by replacing the microchannel plate with a sliding foil holder. Target foils were mounted on a bracket attached to a sliding teflon block assembly. The frame holding the foil support had a 13 mm open slot that allowed the spectrometer a

direct view of the rear of the foil. The foil could then be moved along the beam axis in increments as small as 2.5 microns for a distance up to 50 mm. An aluminum frame with a 12.7 mm diameter hole held the thin self-supporting foils. Although this design did not allow the replacement of a foil without disrupting the vacuum, it was found that the foils withstood bombardments of up to 24 hours by the 2 MeV/amu beams at 1-2 microamp currents without breaking. Thus, it was possible to complete a series of lifetime measurements during an experiment without disturbing the monitor signal normalization by having to replace a broken foil.

The ion beams were focused to a 3 mm by 6 mm spot on a phosphorescent target and then limited to this width by inserting a 3 mm by 9.5 mm rectangular collimator located 76 mm upstream. The collimator allowed nearly complete transmission of the beam through the foil unto a shielded faraday cup located 200 mm downstream. A vertical line focus was chosen so as to achieve maximum light transmission through the spectrometer entrance slit. The collimator was mounted on a moveable rod and could be moved out of the beam path and accurately replaced while the system remained under vacuum.

B. Comparison of Spectra Obtained with Channeltron and Microchannel

Plate Detectors

The results of the initial beam-foil measurements made with the exit slit/CEM arrangement confirmed the prediction that the transition intensities were too low to allow the practical application of this

standard mode of operation. It became apparent that only a survey of the most intense lines could be accomplished with this single-channel detection method. For example, it took 8 hours to scan the spectral region from 105 Å to 38 Å with the spectrometer slit widths set to 100 microns using chordal steps of 10 mils per channel and a foil thickness of $20 \mu\text{g}/\text{cm}^2$, even with 40 MeV Ne^{+3} beam currents of two to three μA .

By comparison, a spectrum of the same region taken using the microchannel plate detector achieved 15 times more statistics in an accumulation time of 40 minutes. Thus, the efficiency in data collection was improved by a factor of 120. A comparison of Ne spectra taken by both methods is given in Fig. 23. The upper spectrum is that accumulated with the exit slit/CEM, and the lower spectrum is a composite of several MCP spectra which were spliced together to produce complete wavelength coverage from 350 - 30 Å. For this composite spectrum, the spectrometer slits were set at 100 microns and the MCP Rowland circle off-tangent angle (angle 2) was set to approximately 3 degrees.

Subtle differences in the intensity patterns in Fig. 23 are due mainly to differences in the response functions of the two detectors. Because many experimental configurations had to be tested in a short period of time, the complex problem of measuring the response functions for the various combinations of detectors and gratings employed was not undertaken. A calibrated detection system is a useful goal, however, and others who have used similar detectors and gratings^{65,73,74,75} reported fairly smooth efficiency curves that decrease in a nearly exponential manner from low to high wavelengths.

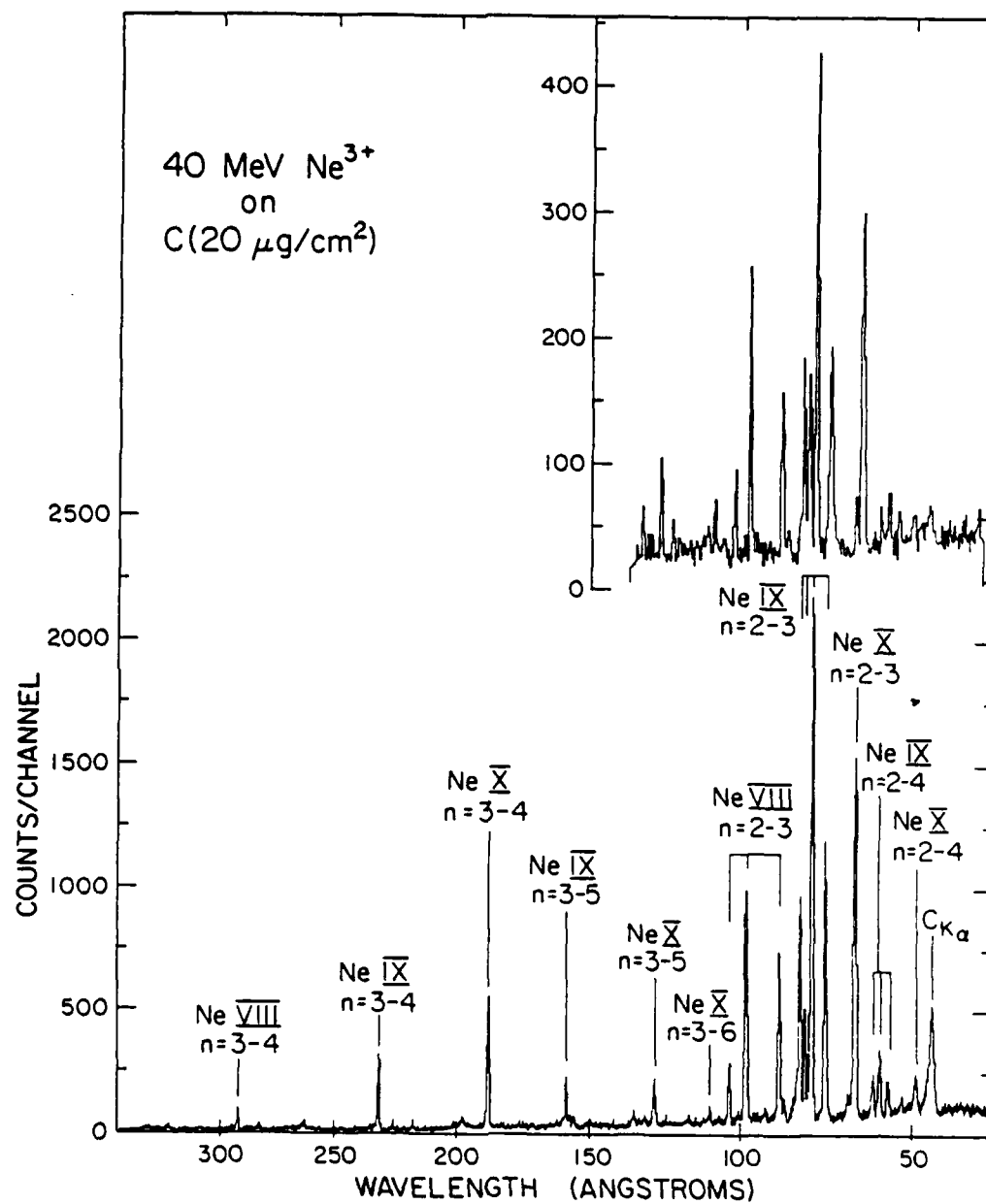


Fig. 23. Composite microchannel plate spectrum₂ of 40 MeV neon excited by passage through a $20 \mu\text{g}/\text{cm}^2$ carbon foil.

Since a simple reference light source is not available in the EUV, a number of elaborate methods of intensity calibration have been used. These include electron and proton impact ionization⁷⁴ synchrotron radiation⁶⁵, charge-exchange excitation of hydrogenic ions in plasmas⁷⁵, and cascade relations or branching ratios from beam-foil data⁷³. All these methods have a number of uncertainties which easily lead to errors of up to 25%, and all require periodic recalibration to account for changes in grating reflectivities. Aside from these difficulties, however, useful comparisons of the relative intensities of the same lines produced under different excitation conditions can still be made without an absolute efficiency calibrated system.

Over forty lines of Ne X, Ne IX and Ne VIII were observed in the wavelength region from 350 to 30 Å. Figures 24 and 25 display the MCP spectra taken at a number of spectrometer position settings, all with identical monitor counts. The identity of these lines is given in the next section of this chapter. It may be seen in Fig. 24 and Fig. 25 that the spectra taken at different spectrometer positions overlap each other. This overlap was intentional and provided a check on the response of the detector. The intensity response was found to be the same as that shown in Fig. 20 in Chapter II. The rapid drop in efficiency in the right portion of the spectra is quite noticeable. For example, line number 37 is twice as intense when measured in the central region of the spectrum as when measured near the right edge.

The center and left portions of the spectra consistently had a resolution of 0.8 Å. However, the resolution decreased to 1.0 Å in the right 25% of the spectra. The 0.8 Å resolution equaled that obtained with the exit slit/CEM detector at 100 μm slit widths and was slightly

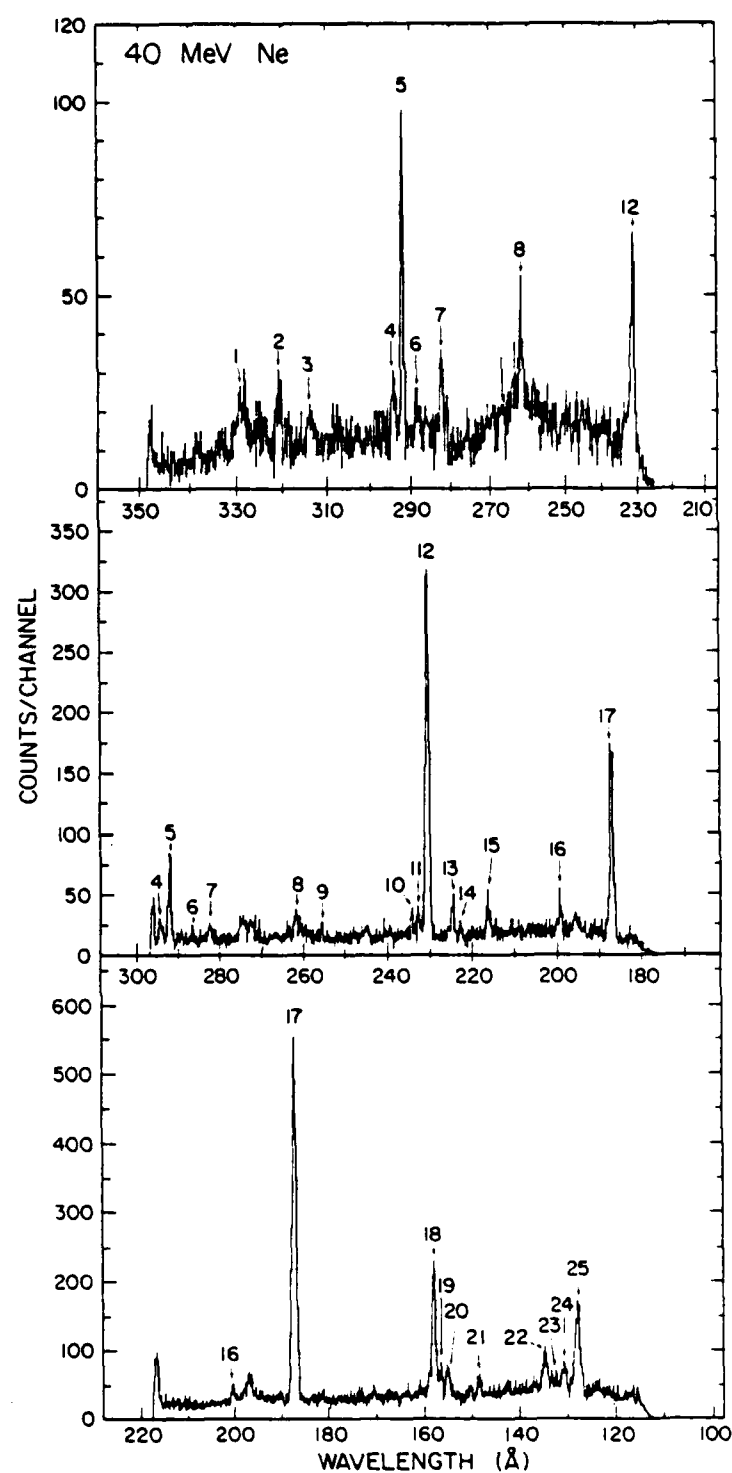


Fig. 24. Microchannel plate spectra of 40 MeV neon taken at spectrometer odometer settings of 10.500, 9.500 and 8.00 from top to bottom, respectively.

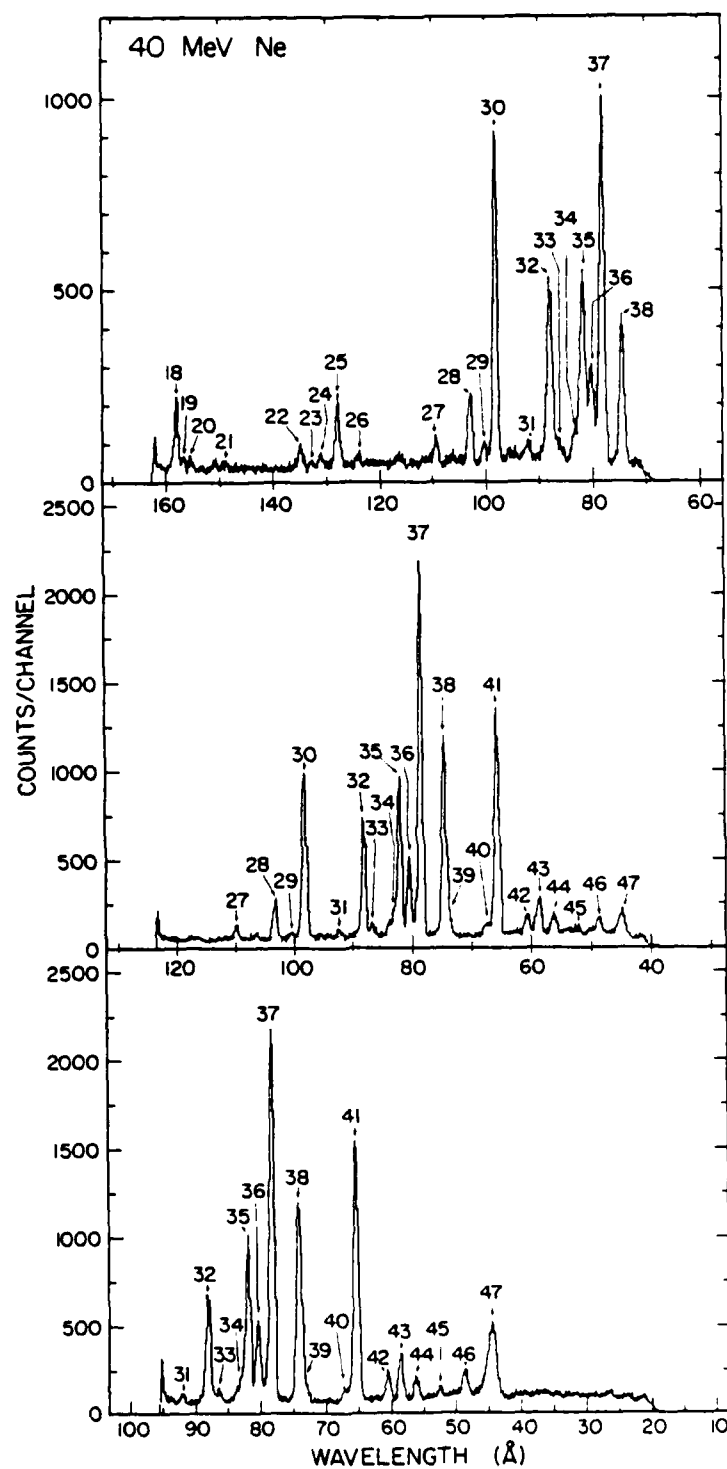


Fig. 25. Microchannel plate spectra of 40 MeV neon taken at spectrometer odometer settings of 6.800, 5.800 and 5.000 from top to bottom, respectively.

better than the 0.9 Å resolution expected from Eq. (2.12). The Doppler broadening component of 0.1 - 0.3 Å predicted by Eq. (1.10) for wavelengths of 100 - 300 Å, respectively, had no discernible effect.

The MCP spectra were calibrated at each spectrometer position for wavelength by fitting a second order polynomial to the channel number and wavelength coordinates of known lines within each spectrum. A fit of wavelength versus channel number for a typical neon spectrum is shown in Fig. 26. The chi-squared deviation of the fit was 7.6×10^{-5} and the resulting calculated wavelengths were within 0.1 Å of the fitted lines.

The second order polynomial equations which fit these spectra had several interesting characteristics:

- (1) the zero order term represented the wavelength of the initial channel number and varied monotonically with the square of the spectrometer position setting, X .
- (2) the first order term varied linearly with X and was negative with a value of near 0.10.
- (3) the second order term was a small value of the order of 10^{-6} and was necessary only to achieve 0.1 Å precision. For rough estimates this term could be ignored.

Expressions of wavelength in terms of spectrometer position are useful because they permit rough predictions (to within 1 Å) of wavelengths for new spectrometer positions. The predictions are not accurate enough for spectral calibration but are useful for general reference when surveying a new region. However, the calibration constants are highly dependent on the electronic gain settings used and

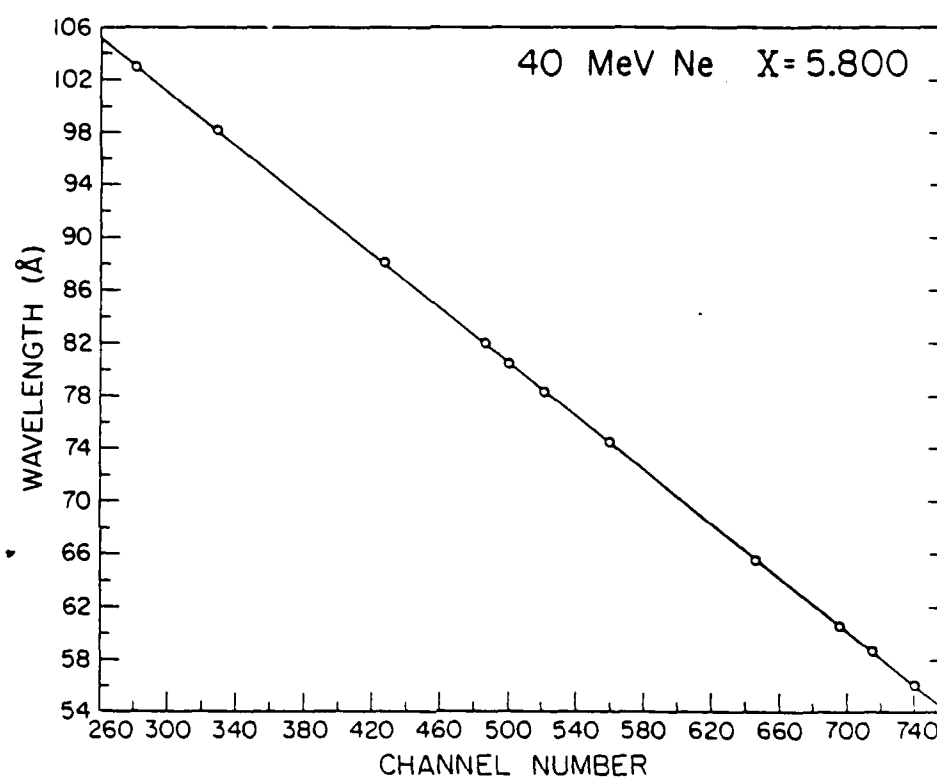


Fig. 26. Spectrometer calibration fit to a second order polynomial for the center spectrum in Fig. 25.

can vary widely (peak shifts of up to 30 channels are not uncommon) if different signal cables, amplifiers or gain settings are used on subsequent set-ups.

C. Neon Line Identification

As is evident from Fig. 23, the spectrum of 40 MeV neon was dominated by lines from one-, two- and three- electron excited states. The transitions in this wavelength region were mainly from $n = 4$ to $n = 3$ and $n = 3$ to $n = 2$. Four Rydberg series were also evident: Ne X $n = 3 - n'$, Ne X $n = 2 - n'$, Ne IX $n = 3 - n'$, and Ne IX $n = 2 - n'$. The most intense lines were from Ne IX, which was consistent with the average charge state of 40 MeV Ne calculated from Eq. (1.11). At this energy, the calculation¹⁵ predicts charge state fractions of 8% for Ne VIII, 42% for Ne IX, and 42% for Ne X. However, instead of a spectrum dominated by equal amounts of Ne X and Ne IX with a scant fraction of Ne VIII present, Ne IX dominated the spectrum as depicted in Fig. 23 and the Ne VIII line strengths exceeded those for Ne X. A more detailed discussion involving level populations is given later in this chapter.

The neon lines numbered in figures 24 and 25 are assigned and compared to previous measurements or theoretical values for Li-like, He-like, and H-like lines in Tables 13, 14, and 15, respectively. In general, the wavelengths were accurate to within 0.1 Å for strong lines and for spectral regions that were calibrated within a number of known lines. Less accurate wavelength values resulted when: (1) the wavelength region had few calibration lines, (2) the lines were

determined by extrapolation rather than interpolation, (3) a weak line was blended by a stronger line, and (4) the line was so weak as to cause a large uncertainty in the determination of its centroid.

TABLE 13. 40 MeV Ne VIII line assignments.

Line #	Wavelength (Å) ^a Measured	Strength ^b	Transition	Other Wavelength ^c Measurements
4	294.5	vw	3rd. Ord. 98.2	---
5	292.4	w	(1s ² 3d) ² D - (1s ² 4f) ² F	292.4
7	282.6	vw	(1s ² 3p) ² P - (1s ² 4d) ² D	282.6
16	200.0 ± 0.3	vw	(1s ² 3d) ² D - (1s ² 5f) ² F	200.0
-- ^d	196.5	vw	2nd. Ord. 98.2	---
28	103.1	w	(1s ² 2p) ² P - (1s ² 3s) ² S	103.0
30	98.2	vs	(1s ² 2p) ² P - (1s ² 3d) ² D	98.2
31	92.2 ± 0.2	vw	(1s2p ²) ⁴ P - (1s2p3d) ⁴ D	92.4 ^e
32	88.1	s	(1s ² 2s) ² S - (1s ² 3p) ² P	88.1
33	86.6	w	(1s2s2p) ⁴ P - (1s2s3d) ⁴ D	86.6 ^e
39	73.5	w,b	(1s ² 2p) ² P - (1s ² 4d) ² D	73.5
40	67.2 ± 0.2	w,b	(1s ² 2s) ² S - (1s ² 4p) ² P	67.4
-- ^d	62.4	vw	(1s ² 2p) ² P - (1s ² 6d) ² D	62.3

^aWavelength accuracy ± 0.1 Å unless shown otherwise.

^bRelative intensity (arbitrary): vs>6000, 6000>s>4000, 4000>m>2000, 2000>m>400, 400>vw, b = blend.

^cReference 76.

^dSome very weak unnumbered lines are included for the sake of completeness.

^eReference 33.

TABLE 14. 40 MeV Ne IX line assignments.

Line #	Wavelength (Å) ^a Measured	Strength ^b	Transition	Other Wavelength ^c Measurements
2	321 ± 1	vw	(1s4f) ³ F - (1s6g) ³ G	--- ^d
3	314 ± 1	vw	2nd. Ord. 158.1	---
6	288.8 ± 0.5	vw	unassigned	288.8
10	234.6	vw	3rd. Ord. 78.3	---
			or (1s3d) ³ D - (1s4p) ³ P	--- ^d
11	232.8	vw	(1s3p) ¹ P - (1s4d) ¹ D	--- ^d
12	231.2	m	(1s3d) ³ D - (1s4f) ³ F	231.2
13	224.9 ± 0.2	vw	(1s3p) ³ P - (1s4d) ³ D	--- ^d
14	223.0	vw	3rd. Ord. 74.4	---
15	216.4 ± 0.5	vw	(1s3s) ³ S - (1s4p) ³ P	216.8
18	158.1	w,b	(1s3d) ³ D - (1s5f) ³ F	158.1
19	156.7	vw,b	2nd. Ord. 78.3	---
20	155.2	vw	(1s3p) ³ P - (1s5d) ³ D	155.2 ^e
-- ^f	150.7	vw	(1s3s) ³ S - (1s5p) ³ P	150.5 ^e
21	148.6	vw	2nd. Ord. 74.4	---
22	134.8	w	(1s3d) ³ D - (1s6f) ³ F	134.9
23	132.7	vw	(1s3p) ³ P - (1s6d) ³ D	--- ^d
26	124.0	vw	(1s3d) ³ P - (1s7f) ³ F	--- ^d
34	82.8	w,b	(1s2p) ¹ P - (1s3s) ¹ S	82.8 ^g
35	82.0	vs	(1s2p) ¹ P - (1s3d) ¹ D	82.0 ^e
36	80.4	s	(1s2p) ³ P - (1s3s) ³ S	80.4 ^e
37	78.3	vs	(1s2p) ³ P - (1s3d) ³ D	78.3

TABLE 14. Continued

Line #	Wavelength (Å) ^a Measured	Strength ^b	Transition	Other Wavelength ^c Measurements
38	74.4	vs	(1s2s) ³ S - (1s3p) ³ P	74.4
42	60.5	w	(1s2p) ¹ P - (1s4d) ¹ D	60.5 ^e
43	58.5	m	(1s2p) ³ P - (1s4d) ³ D	58.5
44	56.0 ± 0.2	w	(1s2s) ³ S - (1s4p) ³ P	56.0
-- ^f	53.8 ± 0.2	vw	(1s2p) ¹ P - (1s5d) ¹ D	54.0 ^e
45	52.6 ± 0.2	vw	(1s2p) ³ P - (1s5d) ³ D	52.4
-- ^f	50.1 ± 0.2	vw,b	(1s2s) ³ S - (1s5p) ³ P	50.3

^aWavelength accuracy ± 0.1 Å unless shown otherwise.

^bRelative intensity (arbitrary): vs>6000, 6000>s>4000, 4000>m>2000, 2000>m>400, 400>vw, b = blend.

^cReference 76.

^dNewly assigned line.

^eReference 33.

^fSome very weak unnumbered lines are included for the sake of completeness.

^gCalculated value given in reference 33.

TABLE 15. 40 MeV Ne X line assignments.

Line #	Wavelength (Å) ^a Measured	Strength ^b	Transition
1	330.0 ± 0.5	vs	
8	262.2 ± 0.2	w	
9	256.1 ± 0.1	w	
-- ^f	244.1 ± 0.1	vw	
10	241.1 ± 0.1	w	

AD-A185 197

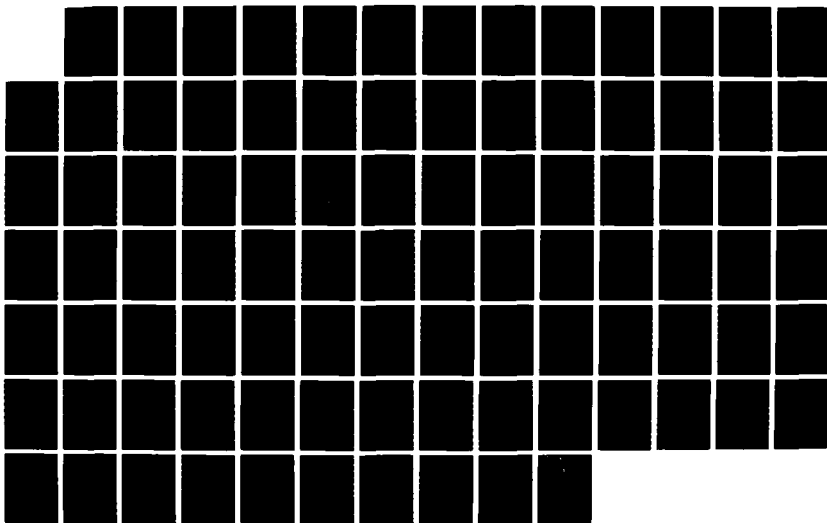
EXTREME ULTRAVIOLET BEAM-FOIL SPECTROSCOPY OF HIGHLY
IONIZED NEON AND ARGON(U) AIR FORCE WEAPONS LAB
KIRTLAND AFB NM J A DEMAREST JUN 87 AFWL-TR-87-26

2/2

UNCLASSIFIED

F/G 20/7

NL



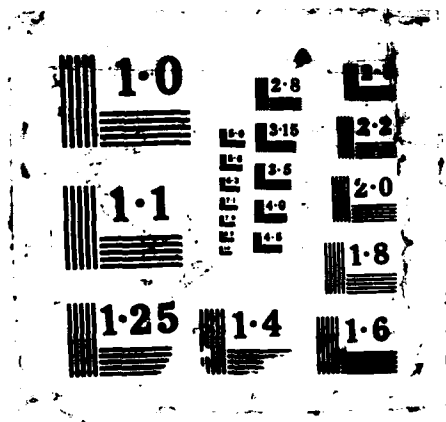


TABLE 15. Continued.

Line #	Wavelength (Å) ^a Measured	Strength ^b	Transition	Other Wavelength ^c Measurements
24	131.0	vw	2nd. Ord. 65.5	---
25	128.0	w	n = 3 - 5	128.1
27	109.5 ± 0.2	w	n = 3 - 6	109.3
29	100.4 ± 0.2	vw	n = 3 - 7	100.4
.. ^f	95.6 ± 0.2	vw	n = 3 - 8	95.4
41	65.6	vs	n = 2 - 3	65.6
46	48.6 ± 0.2	w	n = 2 - 4	48.6

^aWavelength accuracy ± 0.1 Å unless shown otherwise.

^bRelative intensity (arbitrary): vs>6000, 6000>s>4000, 4000>m>2000, 2000>m>400, 400>vw.

^cHydrogen-like fine structure remains unresolved, permitting only level assignments.

^dRef. 76.

^fSome very weak unnumbered lines are included for the sake of completeness.

Of the 53 lines tabulated, ten very weak lines occurred from higher order reflections of strong lines. Fortunately, most of these higher order reflections were well separated from other first order lines. Line 47, the carbon K x-ray at 44.7 Å, was the only non-neon transition observed. The surface of the carbon foil was tilted at a 5 degree angle off the normal to the spectrometer entrance slit and at the foil position used to accumulate this spectrum, part of the foil was directly observable.

Many of the lines were identified by comparing the present wavelength values to values reported in the literature. It took some

effort to identify and assign new lines, and two lines remain unassigned. Of these two, Ne IX 288.8 Å has been reported (but not assigned) in several works^{31,76} and is not predicted by an energy level diagram of singly excited delta $n = 1$ transitions. The other unassigned line falls at 256.0 Å which matches a second order reflection of the Ne X 128.0 Å line. However, since some other stronger lines, such as the Ne IX 82.0 Å line, did not give measurable second order reflections, the origin of the line at 256.0 Å is still unresolved. Both unassigned lines are also greater in wavelength than $n = 3-4$ transitions for Ne X, Ne IX, and Ne VIII which have wavelengths between 216 and 236 Å.

Five of the six newly assigned lines are Ne IX triplet transitions to the $n = 3$ or $n = 4$ levels from higher levels. The remaining line is a Ne IX singlet $n = 3$ to $n = 4$ transition. In assigning these lines, the wavelengths were first checked to insure that they were not higher order reflections of strong lines. Next, the lines were checked against well documented assignments for Ne VIII and Ne X transitions. As some of the lines fell close to previously reported Ne IX lines, it became apparent that constructing a partial energy level diagram would provide a useful reference. Following the approach of reference 33, the energy levels of a number of Ne IX triplet states were tabulated from theoretical values for low l states⁷⁷ or were calculated by the Ritz formula⁷⁸ for higher l states.

The term energy level, T , given by the Ritz formula is

$$T = R \zeta^2 / (n^*)^2, \quad (3.1)$$

where R is the Rydberg constant⁷⁷ for Ne, 109734.3 cm^{-1} , ζ is the net charge equal to $Z - (N-1)$ where Z is the atomic number and N is the number of electrons. The value for ζ is also commonly expressed as the Roman numeral in the spectral symbol. The effective (principal) quantum number, n^* , is also expressed as $n - d$ where d is the quantum defect value. Also, d is largely independent of n and vanishes at large values of l as the effects of penetration into the atomic core diminish. Thus, sufficient accuracy was obtained by setting d equal to zero and using a value of n for n^* when n and l were each greater than 2.

The newly calculated values are shown in a partial level diagram for Ne IX $n = 3$ to $n = 4$ transitions in Fig. 27. A comparison of the newly identified lines with the calculated wavelengths is given in Table 16. The Ne IX $(1s2p) \text{ }^1\text{P} - (1s3s) \text{ }^1\text{S}$ transition at 82.8 \AA , in

TABLE 16. New identifications in Ne IX.

Measured Wavelength (\AA)	Transition	Calculated Wavelength (\AA)	Term Value (cm^{-1})	
			Lower	Upper
321 ± 1	$(1s4f) \text{ }^3\text{F} - (1s6g) \text{ }^3\text{G}$	324.0	$555,530^a$	$246,902^a$
234.6	$(1s3d) \text{ }^3\text{D} - (1s4p) \text{ }^3\text{P}$	234.4	$987,600^a$	$560,913^b$
232.8	$(1s3p) \text{ }^1\text{P} - (1s4d) \text{ }^1\text{D}$	233.2	$984,442^b$	$555,530^a$
224.9	$(1s3p) \text{ }^3\text{P} - (1s4d) \text{ }^3\text{D}$	224.8	$1,000,442^b$	$555,530^a$
132.7	$(1s3p) \text{ }^3\text{P} - (1s6d) \text{ }^3\text{D}$	132.7	$1,000,442^b$	$246,902^a$
124.0	$(1s3d) \text{ }^3\text{D} - (1s7f) \text{ }^3\text{F}$	124.0	$987,600^a$	$181,398^b$

^aRitz formula.

^bReference 77.

good agreement with theory, appears as a weak component to the stronger Ne IX $(1s2p)^1P - (1s3d)^1D$ at 82.0 Å rather than as a separate line at 84.0 Å as reported in reference 33.

D. Neon Lifetime Measurements

1. General considerations

Neon lifetimes for one, two and three electron transitions to the $n = 2$ level from higher levels fall in the picosecond range and require care in obtaining reliable experimental values. A 0.56 mm grating mask was used to limit the average length of the beam viewed by the grating to 0.80 mm. This spatial resolution of the beam translated to a temporal resolution of 40.0 psec for the 20.0 mm/nsec beam. An initial test in which the target foil was stepped by increments of 0.051 mm (2.6 psec or 2 mils) proved that this step size was unnecessarily small in measuring lifetimes greater than 10 psec. Therefore, to economize on beam time, a minimum step size of 0.127 mm (6.4 psec or 5 mils) was used for all subsequent measurements.

The short lifetime limit of a beam-foil measurement has been estimated to range from the minimum foil step size to the sum of the minimum step size and one-sixth the optical averaging length⁷⁹. Also, the upper limit to the mean life of an excited state has been shown to result from the steepest slope on a semi-logarithmic plot of a cascade-affected decay curve¹⁰. For the present measurements the short lifetime limit was predicted to be between 6.4 and 13.1 psec. From the analyses of the neon decay curves, the practical short lifetime limit

was determined to be approximately 9 psec. However, one multiexponential fit resulted in a lifetime of 5.6 psec. Since this decay was heavily influenced by cascade feeding, this value is subject to high uncertainty.

2. Sources of error

Many sources of error are present in beam-foil lifetime measurements. Yet in most instances these errors can be controlled or reduced to allow accurate lifetime determinations. Relevant discussions of the sources of errors are given in references 11 and 80 and are summarized in Table 17 for the present measurements.

TABLE 17. Sources of error in beam-foil lifetime measurements.

Error	Contribution to lifetime Uncertainty
foil thickness uncertainty	< 1%
velocity uncertainty of ion beam	< 2%
charge state equilibrium	< 1%
velocity dispersion of ion beam	< 1%
energy straggling of post-foil ion beam	< 1%
scattering of ion beam	< 1%
Poisson statistics of data	5-10%
cascade effects	5->100%
line blending	5->100%
line position uncertainty	< 1%
foil position uncertainty	< 1.3 ps
monitor signal fluctuations	< 1%
signal/background variations	< 1%

The greatest source of uncertainty in the measurement of lifetimes are cascading and line blending. Using a smaller mask size to narrow

the temporal window and moving the foil in smaller steps reduces the error caused by cascading, a problem for very short lifetimes. Using a narrower slit width or finer grating reduces the error caused by line blending.

On the positive side, the use of a microchannel plate not only improved the data collection efficiency, but proved valuable in reducing common errors associated with single channel data collection methods. One such error that is often overlooked is the way the background signal is subtracted from a lifetime measurement. Single channel data collection methods normally involve measuring a background value once (typically at the start of a lifetime measurement)⁸¹. It is then assumed that this value is constant when in reality the relative proportions of signal-to-background may vary in an unknown fashion with downstream distance. In the case of MCP lifetime measurements, the background and peaks were measured simultaneously so that the background was accurately subtracted at each foil position. In fact, a sudden change in foil condition or signal-to-background ratio due to foil-breakage would be readily apparent in the MCP spectra. Finally, since the lifetimes of a group of transitions were measured simultaneously, internal consistency gave a high degree of confidence in the values obtained.

3. Lifetimes of excited states of 40 MeV neon from 109 to 65 Å

The microchannel plate was set to detect the wavelength region from 112 to 40 Å where the intense lines of Ne VIII, Ne IX and Ne X, $n = 2-3$ exist. Sample spectra taken at several foil positions are shown

in Fig. 28. Since most mean lives of lines in this region are on the order of 10^{-11} seconds, the intensity observed at 3.43 μm , after some 10 lifetimes, is the result of cascade feeding from higher levels. The analysis of lifetime data containing cascade contributions requires a deconvolution into several exponentials, as explained in Chapter I.

The multi-exponential curve-fitting program, Homer⁸², was used to analyze the decay curves. This program fits data by an iterative procedure to a function containing one, two or three exponential terms whose amplitudes and exponents are free parameters. The results are presented in Table 18 and representative fits to the data are given in the appendix. The errors associated with the confidence of the Homer fit based upon one standard deviation are given as a percentage of the lifetime in Table 18. A minimum value of 10%, as discussed above, is shown when the fit gave errors less than this value.

TABLE 18. Lifetimes of excited states of Ne VIII, Ne IX and Ne X.

Wave-length (\AA)	Ion	Upper Level	Lifetime (psec)			Replenishment Ratio ^b
			prompt	This work ^a cascade	Other Values	
231.2 ^c	Ne IX	4^3F	19.5(30%), 45(65%), 1100(41%)	--	--	0.24
109.3	Ne X	$n=6$	11.0(10%), 65(14%)	--	--	0.53
103.1	Ne VIII	3^2S	23.8(15%), 120(98%)	--	21.3(10%) ^d	0.08
98.2	Ne VIII	3^2D	5.6(15%) ^e , 43(10%), >200	--	3.7(15%) ^d	0.48
88.1	Ne VIII	3^2P	13.5(10%), 51(10%)	--	11.5(15%) ^d	0.14

TABLE 18. Continued

Wave-length (Å)	Ion	Upper Level	Lifetime (psec)		Replen- ishment Ratio ^b	
			prompt	This work ^a cascade		Other Values
86.6	Ne VIII	3 ⁴ D	9.2(30%) ^e , 74(30%)		--	0.49
82.0	Ne IX	3 ¹ D	9.2(10%) ^e , 56(12%)		14.0(25%) ^f	0.49
80.4	Ne IX	3 ³ S	23.0(10%), 83(31%)		--	0.06
78.3	Ne IX	3 ³ D	11.3(10%), 97(10%)		14.0(25%) ^f	0.38
74.4	Ne IX	3 ³ P	9.0(10%) ^e , 65(10%)		--	0.18
73.5	Ne VIII	4 ² D	8.6(15%) ^e , 65(12%)		7.8(10%) ^g	0.44
67.4	Ne VIII	4 ² P	27.3(10%)	--	22.0(10%) ^g	0.00
65.6	Ne X	n=3	8.8(15%) ^e , 39(38%), 340(20%)		--	0.50

^aParentheses express errors as discussed in the text.

^bThe ratio of cascade repopulation to decay depopulation as defined by the expressions given in reference 9.

^cMeasurement made with the exit slit/CEM combination.

^dReference 30 where an auxiliary slit gave a minimum mean life limit of below 3 psec.

^eLimited by the minimum mean life limit of 6 - 9 psec.

^fReference 32 where the minimum mean life limit was above 10 psec.

^gReference 31 with a minimum mean life limit of below 3 psec.

4. Discussion of results for carbon-foil-excitation

The agreement between the lifetime measurements in this work and other experimental values that were not limited by minimum mean life determinations was generally within two picoseconds. One exception occurred for the very weak 67.4 Å line and was probably due to low statistics. The reported value of 3.7 psec for the 98.2 Å line⁸³ is in good agreement with the theoretical value of 3.7 psec, whereas our

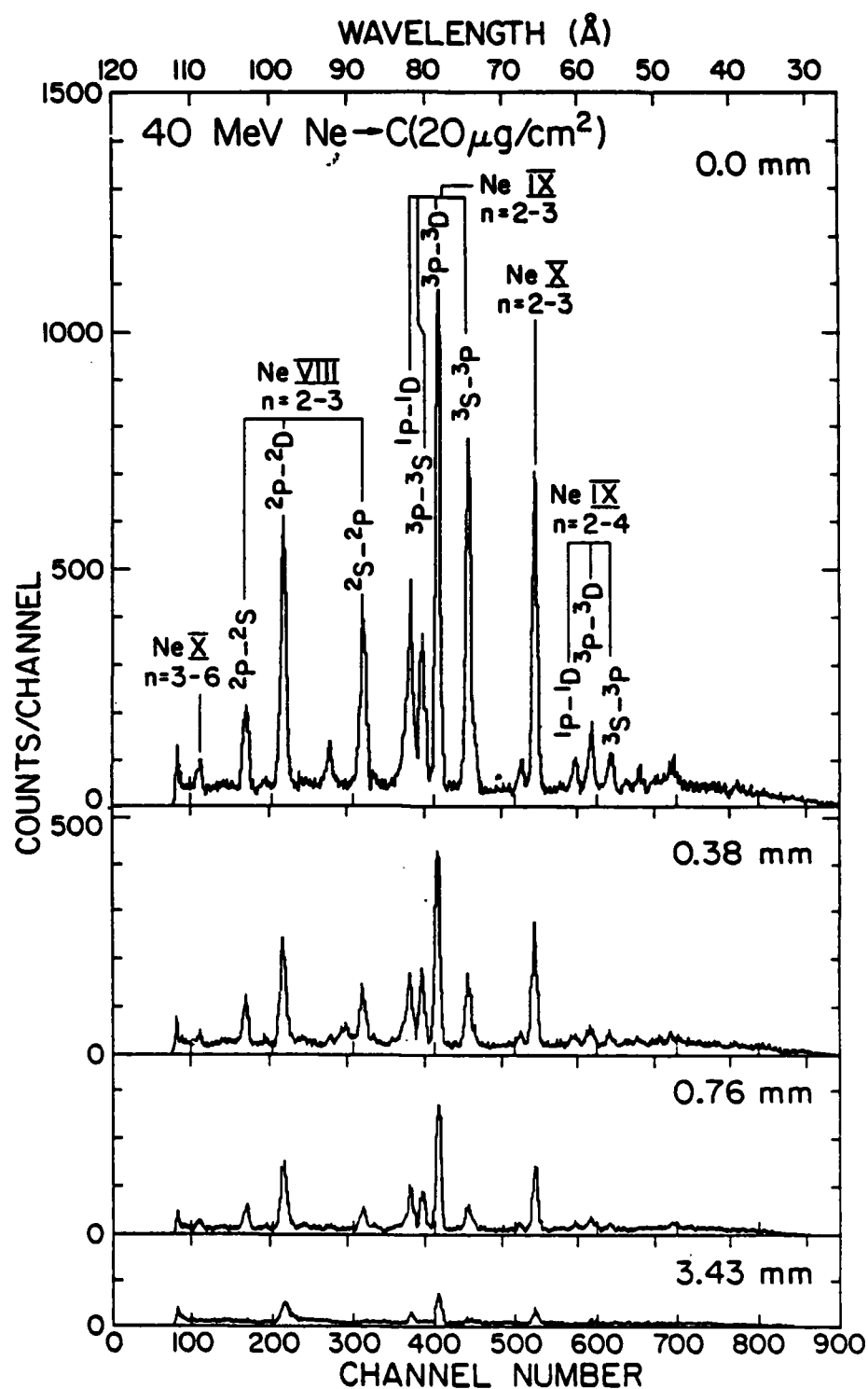


Fig. 28. Spectra of 40 MeV neon on carbon taken at several foil positions.

value of 5.6 psec was limited by the minimum mean life limit of the present experimental method. Another limited value reported here is for the 65.6 Å hydrogenic transition. This line has a theoretical mean life⁸⁴ of 1.0 psec assuming the l states are statistically populated. Since the terms for the 3s, 3p and 3d states were unresolvable (less than 0.2 Å separation), this line was blended by states which have lifetimes of 15.8, 0.5, and 1.6 psec, respectively. Also, the branching ratio for the $n = 3$ state to the $n = 2$ state is only 0.442, while the remaining $n = 3$ fraction decays directly to the $n = 1$ state.

The other hydrogenic line at 109.3 Å provides an interesting look at the deexcitation of a higher Rydberg state. The theoretical mean life of this $n = 6$ state when all l states are statistically populated is predicted to be 19.3 psec⁸⁴. This line is also hopelessly blended by a mixture of transitions from the 6s, 6p, 6d and 6f states having lifetimes of 53.5, 4.1, 11.9 and 24.0 psec, respectively.

The replenishment ratio is a useful value for expressing the relative amount of cascade influence in a lifetime measurement. This ratio reflects the amount of cascade contribution in lines fit with more than one exponential. For example, a value of 0.50 means that 50% of the peak intensity in the decay curve results from a cascade rather than from the decay of the initial population of the level. It has been suggested that only when the replenishment ratio is less than 0.10 can lifetimes be determined with errors of less than 5%⁸⁵. The replenishment ratio, $R(0)$, is defined in reference 9. A replenishment ratio for a two exponential fit is given by

$$R(0) = (1 - \tau_1/\tau_2) C_2/(C_1 + C_2) \quad (3.2)$$

The mean lives in this case are τ_1 and τ_2 and the amplitudes at $t = 0$ are given by C_1 and C_2 . However, these amplitudes are not the amplitudes from the fitted data since the fitted amplitudes have to be corrected for the finite time window, Δt , of the measurement. The corrected amplitudes, C_i (true), are given by

$$C_i(\text{true}) = C_i(\text{fitted}) [\Delta t/(2\tau_i)/\sinh(\Delta t/2\tau_i)] \quad (3.3)$$

The replenishment ratio can be reduced by decreasing the finite time window. For example, Berry *et al.*³⁵ reported a reduction in $R(0)$ from 0.40 to 0.26 for the 59 psec Cl VI (3s3d)³D - (3s4f)³F transition when they used an auxiliary slit to reduce the finite time window from 180 psec to 14 psec. The improvement is more pronounced for faster decays.

In summary, six new lifetimes are reported here and seven lifetimes which have been determined by previous investigators have been remeasured. The known lifetimes not only provide a check of the accuracy of the present methods, but also give a frame of reference for comparing the deexcitation of projectile ions excited by passage through foils of materials other than carbon, as given in the following section. A number of lines were limited by the minimum mean life threshold of this experimental procedure, and improved measurement can only be made by approaching the state of the art limit for the beam-foil method of one psec. At one psec, however, even the bulge in the foil can cause a significant error.

E. Characteristics of Spectra Obtained with Other Exciter Foils

1. Background

In the field of beam-foil spectroscopy researchers have generally concentrated on measuring lifetimes and wavelengths for new transitions and have ignored the mechanics of the excitation process. However, an understanding of the excitation mechanism is also of fundamental interest and is even necessary in some cases for a proper analysis of cascade corrections to the data⁸⁶. The concept of relative level populations is used for estimating cascade contributions where the relative level population is defined as the probability per projectile of populating a specific state or level following foil excitation⁸⁷. Only recently have efforts been directed at examination of the beam-foil collision mechanism with the goal of determining the populations of the various states which are produced^{42,88,89}.

This section presents the results of a comparison of neon projectile EUV spectra obtained with several different exciter foils. The excitation mechanism in the ion-target interaction is still not well understood and may depend upon a number of competing processes. As a fast moving ion penetrates the foil, the outer electrons are quickly stripped away leaving the ion in a highly charged state. The ion is then free to capture electrons from the foil and lose these electrons in the multiple collisions the ion undergoes until exiting the foil. The ion can also capture electrons from the back surface or the last few layers of the foil. However, under the common beam-foil vacuum conditions of 10^{-6} torr, surface contamination should provide

the same environment for last layer capture regardless of foil material. Therefore any variations in the radiation given off by the excited projectiles when different foil materials are used are most likely to be caused by events which take place inside the foil. Such effects have been postulated to play an important role for fast collisions at velocities far exceeding the first Bohr velocity. For Example, Betz et al.⁹⁰ found that the production of projectile Rydberg states exhibited a pronounced target-thickness dependence for 125 MeV sulfur ions with carbon foil thicknesses of 2-200 $\mu\text{g}/\text{cm}^2$. This thickness dependence was found to be not related to direct capture of target electrons from last layers but was suggested as being recaptured projectile core electrons which were ionized throughout the target and became wake riding electrons.

2. Comparison of Spectra Taken Immediately Behind the Foil

Foils of carbon, silver and gold were chosen for comparison as these materials vary widely in their electron densities (6.78, 27.5 and 46.6×10^{23} electrons per cm^3 , respectively). The foils were chosen to be thick enough to withstand breakage from bombardment by beam currents of several microamperes but thin enough to limit the velocity loss of the beam to one percent or less. The thicknesses of the self supporting foils of carbon, silver and gold were 20, 82 and 150 $\mu\text{g}/\text{cm}^2$, respectively.

"Prompt" spectra of 40 MeV neon were taken by observing the region immediately downstream from the foil. In this context, "prompt" is defined by the foil position which corresponded to a maximum in the

radiation intensity measurements for fast (on the order of picosecond) transitions. This maximum was due to the integrated intensity of all transitions occurring within the 40 psec viewing region of the spectrometer. The microchannel plate was set to detect the same wavelength region of 112 to 40 Å in each case. The prompt spectra taken with the silver and gold foils were virtually identical and noticeably different from carbon. The solid line spectrum of neon on gold is compared to the dotted line spectrum of neon on carbon in the upper portion of Fig. 29.

Some immediate qualitative observations can be made from this comparison. The average charge state of the Ne projectiles is decreased by nearly one unit when the higher Z foils are employed. This conclusion follows from the fact that the Li-like lines are now most intense. This is not surprising and, as mentioned in Chapter I, is due to the ease of electron capture from the more loosely bound electrons in the metals. Another more subtle but unexpected difference in the two spectra is that the relative intensities of lines arising from the same charge state are quite different. For the Li-like lines, the 3^2D line at 98.2 Å is considerably enhanced by the Au and Ag foils. In the case of He-like lines, the largest difference appears as the reduction in the population of the 3^3S line at 80.4 Å in the Au and Ag spectra. Before any conclusions can be made from this comparison, it is necessary to determine the extent of cascade contributions to the line intensities.

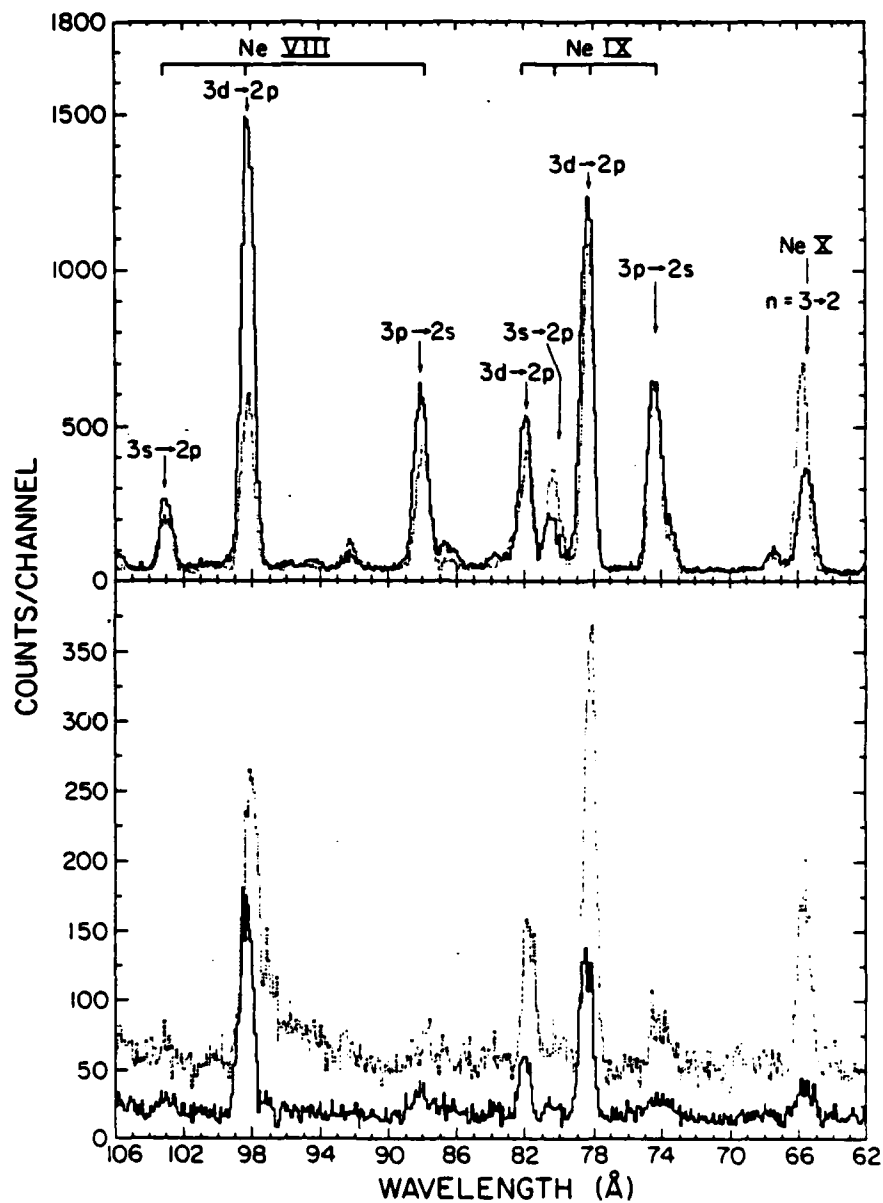


Fig. 29. Spectral comparison of 40 MeV neon passing through 150 $\mu\text{g}/\text{cm}^2$ gold (solid line) with 40 MeV neon passing through 20 $\mu\text{g}/\text{cm}^2$ carbon (dotted line).

3. Foil effects on the cascade population of $n=2-3$

Li-, He- and H-like neon

The decays of all $n=2-3$ transitions of Li-, He- and H-like neon excited by carbon, silver and gold were examined to account for differences in the cascade populations of higher levels. As expected, there were essentially no lifetime differences in the decay curves. But, there was a vast difference in the intensity of the decay curves beyond the prompt decay region.

The difference is readily seen in the comparison of neon spectra excited by carbon and gold taken 3.4 mm or 170 psec downstream as depicted in the bottom half of Fig. 29. This decrease in the cascade intensity when the metal foils were employed can be expressed by the difference in the replenishment ratios for the respective lines. These values are given in Table 19.

The following observations can be made from the above table: (1) if cascading was a significant factor for the Ne lines from the carbon measurements (replenishment ratio greater than 0.2 as was the case for all yrast transitions (3D states)), the effect of cascading decreased by a factor of two for the silver measurements and decreased even further for gold; (2) if cascading was not significant for the carbon measurements (all non-yrast transitions), it was negligible for the silver and gold measurements. This implies that the population of higher n states which would normally decay within the 170 psec temporal scan made in these measurements ($n \leq 6$ for Ne VIII and $n \leq 5$ for Ne IX) was noticeably reduced for the metal foils.

TABLE 19. Replenishment ratios for carbon, silver and gold excited neon.

Wavelength (Å)	Carbon	Silver	Gold
103.0	0.08	0.00	0.00
98.2	0.48	0.16	0.07
88.1	0.14	0.00	0.01
82.0	0.49	0.26	0.20
80.4	0.06	0.00	0.00
78.3	0.38	0.20	0.05
74.4	0.18	0.02	0.02
65.5	0.50	0.31	0.05

One explanation based on experimental conditions for reduced intensities at greater upstream foil positions (longer delay times) would be due to multiple scattering effects which are expected to increase with the heavier foils. However, as shown in Chapter I, the scattering angles for all foils were calculated to be less than one degree (see Table 1) and can be discounted as the source of the intensity reduction mechanism.

Another explanation based on experimental conditions involves the possibility of foil deterioration over the course of the lifetime measurements. An argument against this explanation comes from the fact that not all of the transitions that were simultaneously measured showed reduced intensities at the longer delay times. Only the yrast transitions for the different foils displayed such a behavior whereas the non-yrast transitions gave identical decay curves.

A final experimental explanation on how the replenishment ratio could be reduced was discussed in Section D, by reducing the finite time window of the spectrometer. However, the same experimental

conditions were used for all measurements. The only difference in the measurements was that the carbon data was taken on a different date than the metal foil data.

A possible physical effect that could account for the reduction in cascading could be due to the development of a strong electric field behind the metal foils. Field ionization of some of the high-lying strongly excited Rydberg levels would reduce their cascade contributions. An even more salient effect within given n levels would result from Stark mixing of high- l states with low- l states thus depleting yrast cascades and allowing the newly created low- l states to decay directly to deep-lying vacancies⁹¹.

F. Spectrometer Relative Efficiency Determination

To make more meaningful and quantitative comparisons of the data, it is necessary to determine the level population for the various lines. The relative line intensities, corrected for background and cascading, can be converted into relative level populations by use of the relation⁸⁸

$$N_k = S(\lambda_{ki}) / (K(\lambda_{ki}) \times A_{ki}) \quad , \quad (3.4)$$

where N_k is the relative population of level k , $S(\lambda_{ki})$ is the signal per monitor count of the transition at the wavelength λ_{ki} from the upper level k to the lower level i , $K(\lambda_{ki})$ is the quantum efficiency of the detection system at wavelength λ_{ki} , and A_{ki} is the transition probability for the transition from level k to level i . Note that

autoionization does not compete for the transitions listed in Table 18 and A_{ki} is expressed entirely by the radiative transition probability.

An examination of the available data indicated that it should be possible to perform a rough calibration of the relative efficiency of the spectrometer and microchannel plate detector over the wavelength range of 350 to 45 Å. The method reported by Trabert⁷³ was used to construct a relative efficiency curve. Accordingly, a pair of decays from the same upper level was used since the intensity of a given decay from level k to level i is proportional to the population N_k of level k , to the branching ratio β_{ki} , and to the detection efficiency K :

$$I(\lambda_{ki}) \propto N_k \beta_{ki} K(\lambda_{ki}) \quad , \quad (3.5)$$

where the branching ratio is the fractional probability of the decay from level k to level i compared to the sum of all decays from level k

$$\beta = A_{ki} / \sum_j A_{kj} \quad . \quad (3.6)$$

Thus, the ratio of a pair of decays from the same upper level yields

$$K(\lambda_2)/K(\lambda_1) = A_{k1} I(\lambda_2) / A_{k2} I(\lambda_1) \quad . \quad (3.7)$$

Since the intensities of lines from the same upper level show the same temporal behaviour, they do not need to be corrected for the time window of the detection system. It is sufficient to measure all lines with the foil in the same position. A small correction was applied to normalize the intensities of the lines to the central channel of the

MCP spectrum to compensate for the intensity response shown in Fig. 20. This correction came from a linear fit to the intensity response in Fig. 20 over the channel number region 200-600 where the response is reasonably linear. For example, factors of 0.92, 1.00, and 1.04 were applied to peak intensities in channels 200, 490, and 600, respectively. The calibration method is limited by possible line blending, by the uncertainty associated with weak lines and the assumption of a smoothly varying response. It is also limited by the construction of a response curve by seemingly unrelated ratios of line pairs. However, the line pairs can form a nonarbitrary response curve by an averaging method such as proportional allotment reported in reference 92.

The transition probabilities for the inter-shell transitions were taken from the literature where available or were calculated using the Coulomb approximation⁹³. The Coulomb approximation is generally accurate to within 25% when LS coupling applies, when the upper level is other than ns, and when the transition integral is not too small. In many instances it has been found that the Coulomb approximation is just as accurate as more elaborate self-consistent field calculations including exchange⁹⁴. The Coulomb approximation expresses the potential of an ion by its asymptotic Coulomb form and allows the analytic calculation of the square of the transition integrals, σ^2 , based upon the term value and azimuthal quantum number. The line strength, S , is given by the product of the relative multiplet strengths⁹⁵ and the square of the transition integral. The transition probability is then expressed by

$$A_{ki} = (2.026 \times 10^{18} \times S) / (g_k \times \lambda^3) \text{ sec}^{-1} \quad (3.8)$$

when λ is given in Å and g_k is the statistical weight for the upper level ($2J+1$ for a line or $(2S+1)(2L+1)$ for a multiplet). Another convenient source for the transition probability is obtained from tabulations of the oscillator strengths, f_{ik} , where

$$A_{ki} = (6.670 \times 10^{15} \times g_i \times f_{ik}) / (\lambda^2 \times g_k) \quad (3.9)$$

The line pairs used to generate an efficiency curve discussed above are given in Table 20.

The relative efficiency curve is shown in Fig. 30. Since a number of line pairs overlapped each other and the region was fairly well covered from 280 to 50 Å, the error in the curve should not exceed 20%. In general, it was expected that the calibration curve would increase smoothly and peak at the reported blaze wavelength of 20.3 Å for the one degree blaze angle and then fall rapidly at shorter wavelengths. Instead, the calibration curve was found to peak at approximately 70 Å. A similar finding was reported by Trabert⁷³ who expected his curve to peak at the blaze wavelength of 127 Å, but found it to peak at 190 Å instead. The source of this discrepancy is not known but could be due to possible contamination of the surface of the grating as mentioned in Chapter I. The drop in intensity above 60 Å is not obvious from the neon data since all $n=2-3$ lines lie above this wavelength and the $n=1-2$ lines occur at less than 14 Å, outside the spectral region sampled. However, as shown in Chapter IV, the intensity of argon $n=2-3$ lines in

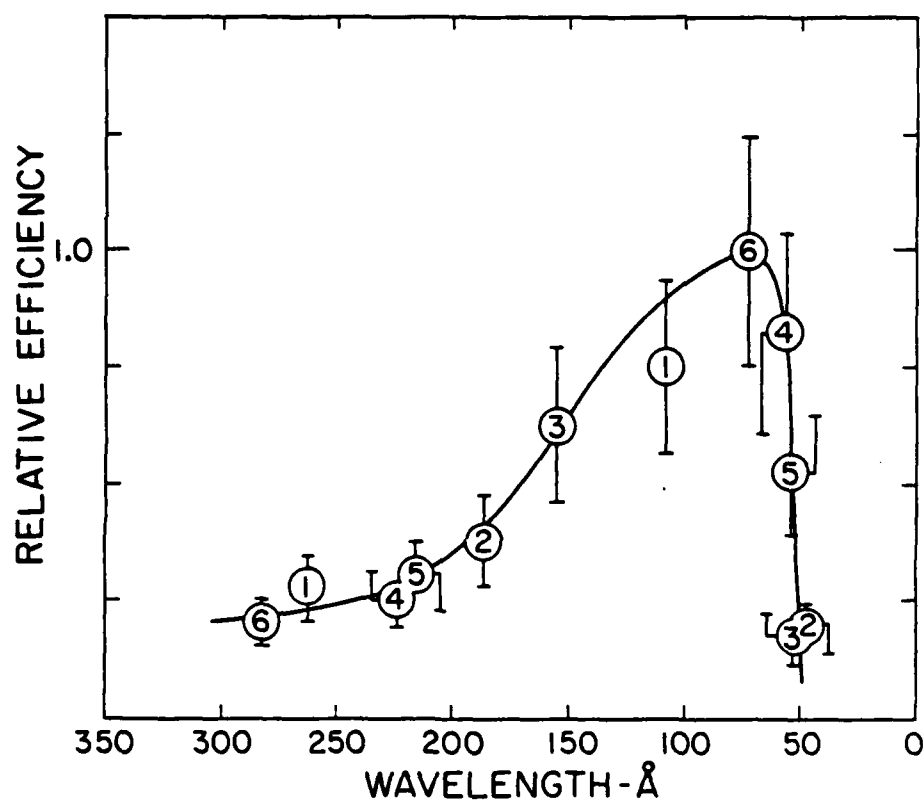


Fig. 30. Relative efficiency curve for the 1200 l/mm grating and microchannel plate detector.

TABLE 20. Transition pairs used for a relative efficiency calibration.

Pair #	Transition	Ion	Wavelength Å	$A_{ki} \times 10^8 \text{ sec}^{-1}$
1	n - 4 - 6	Ne X	262.2	77.1 ^a
1	n - 3 - 6	Ne X	109.3	77.8 ^a
2	n - 3 - 4	Ne X	187.4	899 ^a
2	n - 2 - 4	Ne X	48.6	842 ^a
3	3p - 5d	Ne IX ^b	155.2	221 ^c
3	2p - 5d	Ne IX	52.6	644 ^c
4	3p - 4d	Ne IX	224.9	457 ^c
4	2p - 4d	Ne IX	58.5	1420 ^c
5	3s - 4p	Ne IX	216.9	1870 ^d
5	2s - 4p	Ne IX	56.0	6470 ^d
6	3p - 4d	Ne VIII	282.6	283 ^e
6	2p - 4d	Ne VIII	73.5	908 ^e

^aReference 31.^bOnly triplet states are used for Ne IX.^cCoulomb approximation.^dCalculated from the weighted oscillator strength from reference 96.^eReference 83.

the region of 33 to 25 Å is much less than the weaker transitions of the n=3-4 lines which occur at wavelengths greater than 70 Å. This observation supports the current efficiency curve.

G. Relative Populations of n=2-3 Li- and He-Like Neon

Once the relative efficiency versus wavelength is known, Eq. 3.4 may be applied to determine relative populations of levels. The efficiency was found to vary by less than 10% for the wavelength region

between 103 to 65 Å where lifetime measurements were made. However, it was necessary to apply a decay correction to Eq. 3.4 when the temporal window was greater than the mean lifetime of the transition. The temporal window of 40 psec in this study was greater than the mean lifetimes of all the lines of interest so that the intensities had to be corrected for cascade contributions. This correction can be made by applying Eq. 3.3 if the temporal window is known and if a decay curve is obtained for each transition.

The relative populations for the Li- and He-like neon lines are shown in Fig. 31. All levels excited by the metal foils are more highly populated than those excited by the carbon foil except for the Ne IX 3^3S state. Very little difference exists between the level populations excited by the Ag and Au foils.

Another way of examining the relative populations is to normalize the value for the terms in each charge state by dividing by its respective statistical weight. After applying this correction, the relative populations will all have the same value if the states are statistically populated. The normalized values are shown in Fig. 32. The nonstatistical nature of the levels is clearly shown for Ne VIII where it is apparent that the lower l levels are overpopulated. For Ne IX the 3^3P , 3^3D , and 3^1D levels are statistically populated. The only exception for Ne IX is the 3^3S level which is overpopulated by factors of three, six and nine for excitation by silver, gold and carbon, respectively.

The preference for the population of low l states in 40 MeV neon ions is consistent with previous findings for 40-70 MeV oxygen^{40,97} and 35 MeV fluorine⁹⁸. The population of low l states are also consistent

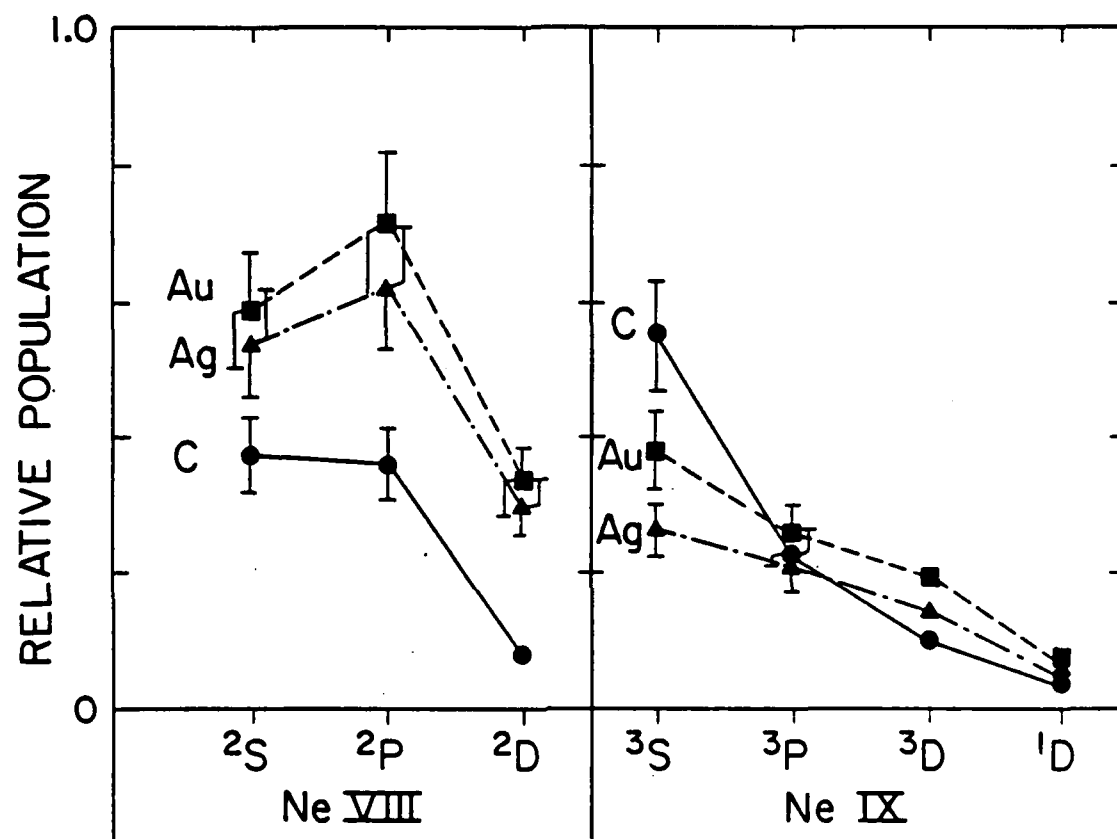


Fig. 31. Relative populations of the $n=3$ levels in Ne VIII and Ne IX for states of different orbital angular momenta.

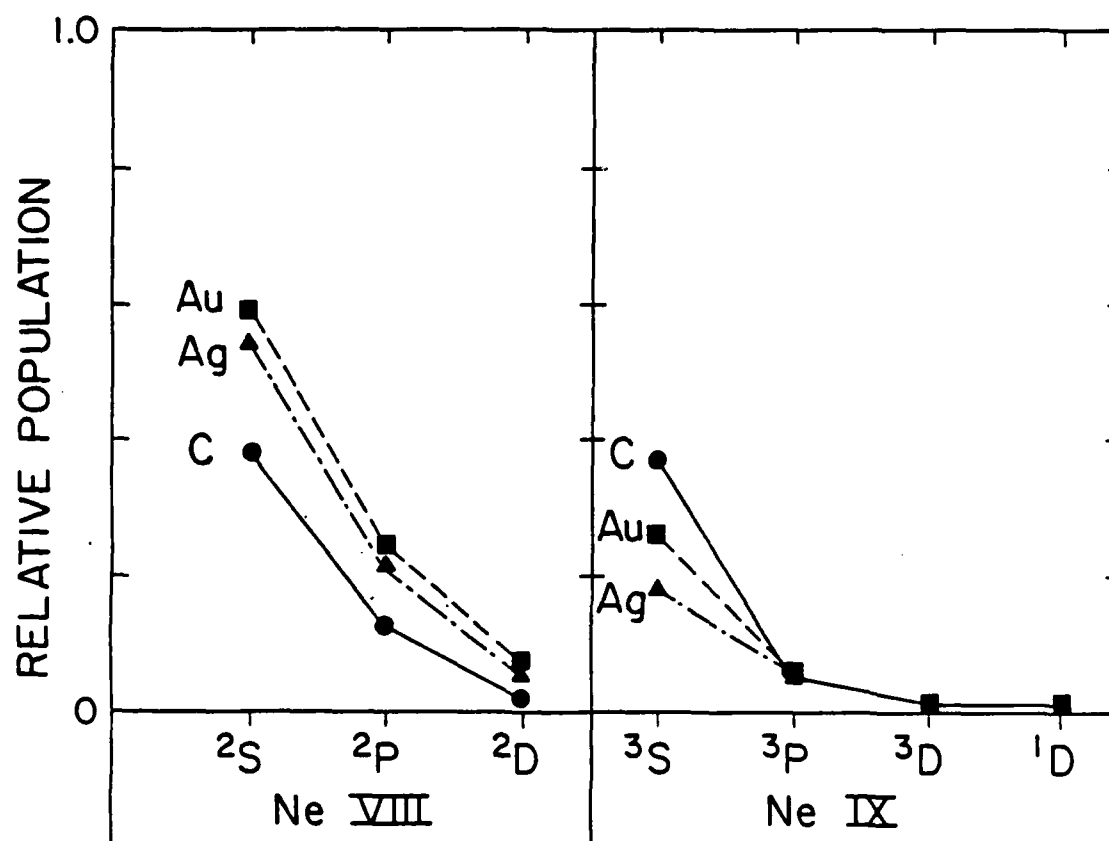


Fig. 32. Relative population of Ne VIII and Ne IX $n=3$ levels compared to statistical population.

with the first Born and Brinkman-Kramers approximations of electron capture⁹⁹ from the target by fast projectiles of velocity v , where the cross sections for electron capture scale as v^{-2} . For example, Andresen and Veje⁹⁹ calculate a maximum capture cross section into s states for MeV/amu magnesium ions. Whether this mechanism accounts for the present results would have to be confirmed by a velocity dependence study of the neon projectile. However, other excitation mechanisms such as bound-bound excitation¹⁰⁰, Coulomb capture of convoy electrons, radiative electron capture of continuum electrons⁴⁰, and, at lower velocities, molecular-orbital promotion processes⁸⁹ all compete so that it is not yet clear what mechanism dominates.

The one state where the population changes clearly depend upon foil material is the 3^3S Ne IX state. Such wide variations in intensity (by factors of 3) are analogous to the reported¹⁰¹ oscillatory behavior of 64 MeV sulfur ion $K\alpha$ satellite and hypersatellite intensity distributions as a function of target atomic number. Such oscillations were found to be correlated to predicted K- and L- electron capture cross sections by the sulfur ions.

In summary, it appears that additional measurements to establish the ion velocity dependence and target atomic number dependence of the population of the neon $n=3$ levels are warranted. Also, it is seen that the l dependence of neon $n=3$ states is not well represented by often used simple analytical expressions⁸⁶ to describe decay curves, i.e., $(2l+1)/n^p$, where p varies from 2 to 3. Bashkin¹⁰² suggests that such expressions give neither the correct l dependence nor n dependence and that experimentally determined level populations have to be used in beam-foil decay models.

CHAPTER IV

EUV MEASUREMENTS OF 80 MEV ARGON

A. Isoelectronic Trends

Because a large accelerator, such as a cyclotron, is needed to produce useful yields of Li-like, Be-like, and B-like argon ions, few extreme ultra-violet beam-foil studies of highly excited argon have been reported. The work presented here on argon was pursued for several reasons. First, it eliminated part of the void that existed for argon in the data base of atomic spectra. Second, it supplemented previous isoelectronic EUV studies of elements from Mg to Cl. Finally, it complemented the study of neon discussed in Chapter III and emphasized how rapidly atomic spectra change as the atomic number of the element under investigation is increased.

In isoelectronic sequences, a number of relations characterizing electric dipole transitions change in a predictable manner as a function of the nuclear charge, Z . The electric dipole transition probability, A , normally dominates radiative deexcitation mechanisms and is proportional to the product of the cube of the transition energy ΔE and the dipole transition integral and is expressed by¹⁰³

$$A \propto (\Delta E)^3 [(\Psi_f | r | \Psi_i)]^2, \quad (4.1)$$

where Ψ_f is the wavefunction of the final state and Ψ_i is the wavefunction of the initial state. The transition integral can also be expressed as a function of line strength, S , (see Eq. 3.8).

$$A = (\Delta E)^3 S(i,f) \quad (4.2)$$

The line strength has been found to vary approximately as $1/Z^2$. Also for $\Delta n=0$ transitions in few electron systems, the transition energies vary in a hydrogenic way approximately as Z^2 . Then from Eq. 4.2 it follows that the transition probabilities for $\Delta n=0$ out of shell transitions vary as Z^4 . However, for in shell $\Delta n=0$ transitions, the transition energies are principally dependent on the interelectronic Coulomb interactions whose matrix elements vary as Z . Therefore, for $\Delta n=0$ transitions, the transition energies are proportional to Z . Applying Eq. 4.2 to $\Delta n=0$ transitions results in the discovery that transition probabilities vary simply as Z as well.

The conclusions to be drawn from these relations are that as heavier elements are examined, the energies of $\Delta n=0$ transitions rapidly approach the x-ray region and the transitions become too fast to measure by the beam-foil method. But since the $\Delta n=0$ transitions increase in energy and rate more slowly than $\Delta n \neq 0$ transitions, they remain interesting candidates for study in the EUV by the beam-foil method up to $Z=50$ ¹⁰⁴ even though relativistic effects gain importance for $Z \geq 18$.

By examining 80 MeV Ar ions in the wavelength region from 355 Å to 25 Å, this study was able to investigate charge states of argon from

Ar^{+12} to Ar^{+15} with transitions from $n=2-2$; $n=3-4$; $n=4-5,6,7$; $n=5-6,7$; and $n=6-8$.

B. Comparison of Argon Spectra Obtained with the Channeltron and Microchannel Plate

The spectral lines of highly ionized argon in the wavelength region from 355 Å to 25 Å were examined using a beam of 80 MeV Ar-ions incident on a thin carbon foil. A composite spectrum formed by overlapping the spectra for six different positions of the MCP is shown in Fig. 33. At the longer wavelengths (above 150 Å) the intrashell $n=2-2$ transitions of Ar XVI (Li-like), Ar XV (Be-like) and Ar XIV (B-like) dominate, whereas at shorter wavelengths, intershell transitions to the $n=3$ and $n=2$ levels of Ar XVI, Ar XV, and Ar XIV are the most prominent features in the spectrum. The inset in Fig. 33 shows a spectrum obtained in the conventional single channel counting mode with an exit slit/CEM combination. The line structure in the two spectra is quite similar except that the resolution is much better (0.8 Å) for the MCP spectrum due to the use of a narrower entrance slit (100 μm). The CEM spectrum was obtained with 200 μm slit widths resulting in a resolution of 1.8 Å.

The CEM/exit slit arrangement required a scan of over six hours to cover the same spectral region as one MCP spectrum, which took less than one hour. Under similar beam conditions for both detectors, three times the intensity was obtained with the MCP detector in less than one eighth the time. Therefore, the data collection rate was nearly 25

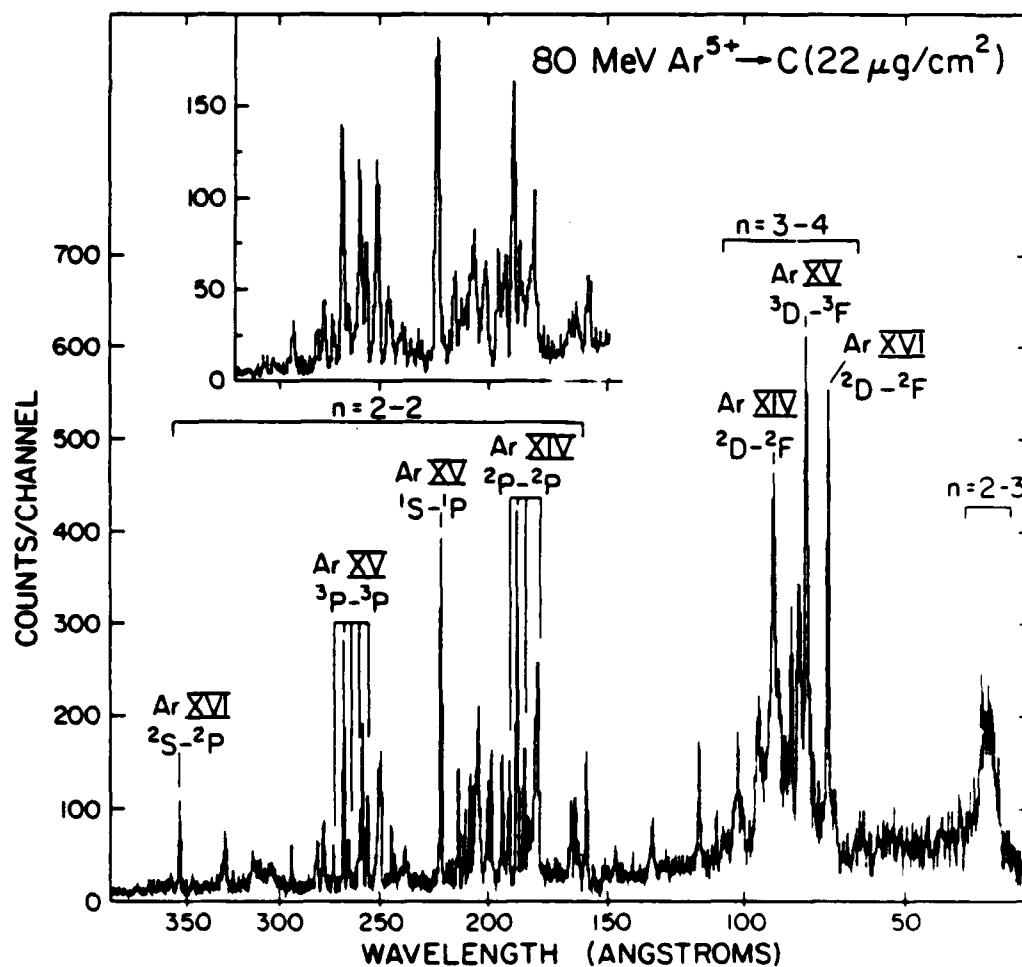


Fig. 33. Composite microchannel plate spectrum of foil excited argon.

times greater for the MCP despite the fact that the entrance slit width was half as large. It has been found experimentally that doubling the slit widths when using the CEM detector results in quadrupling the acquired intensity. Therefore, the overall data collection efficiency with the MCP is effectively improved by approximately two orders of magnitude. This improvement is consistent with that observed in the neon study.

The general features of the composite spectrum of 80 MeV Ar differ considerably from those of the 40 MeV Ne composite spectrum in the EUV region of 350 Å to 25 Å. This difference is partly due to the different charge states and partly due to the Z dependence of line energies and line strengths as discussed in the previous section. Using Eq. 1.11, the equilibrium charge state of 80 MeV Ar is calculated to be 14.0 (i.e., Be-like Ar XV). While Ar XV is predicted to dominate, nearly equal amounts of Ar XVI and Ar XIV are expected. The three yrast lines of $n=3-4$ for these three charge states are identified in Fig. 33 and their respective intensities support the charge state prediction of Eq. 1.11 for 80 MeV Ar.

The longer wavelength region of the argon spectrum is composed of $\Delta n=0$, $n=2-2$ transitions, lines which do not occur in neon below 460 Å. The structure at 70-100 Å is composed of the complex and overlapping lines of Ar XIV, Ar XV, and Ar XVI $n=3-4$. Similarly, the overlapping lines of $n=2-3$ Ar XIV, Ar XV, and Ar XVI appear at 25-30 Å.

C. Argon Line Identification

The individual MCP spectra that composed Fig. 33 are shown in Fig. 34 and Fig. 35. Proceeding from top to bottom in Fig. 34, the spectra were taken at spectrometer positions of 11.300, 10.000, and 8.800 on the odometer. From top to bottom in Fig. 35, the spectrometer was set to positions of 6.800, 5.800 and 4.800 on the odometer. The spectra were intentionally overlapped to study the response of the MCP at different positions. The minimum number of settings to cover the same wavelength region with minimum overlap would be four spectrometer positions at 11.000, 9.000, 7.000, and 5.000. The same integrated charge/channel (monitor count) was used to accumulate the three spectra in Fig. 34 and the top spectrum of Fig. 35. The middle spectrum and bottom spectrum in Fig. 35 were taken with two thirds and one third, respectively, the monitor counts for the others.

The argon lines are numbered as shown in the figures and compared to previously measured or calculated values in Tables 21, 22, 23, and 24 for the C-like, B-like, Be-like, and Li-like lines, respectively. Most of the lines in Fig. 34 were assigned by comparing the wavelengths of the observed lines to the extensive compilation of previously observed or calculated $\Delta n=0$ lines given in reference 105. The wavelength calibration was accomplished, as explained in Chapter III, with a second order polynomial fit of wavelength versus channel number. All the numbered lines in Fig. 35, however, are new and unassigned so that a different procedure was used to calibrate these spectra. Following the 80 MeV Ar experiment, spectra of 40 MeV Ne were taken at

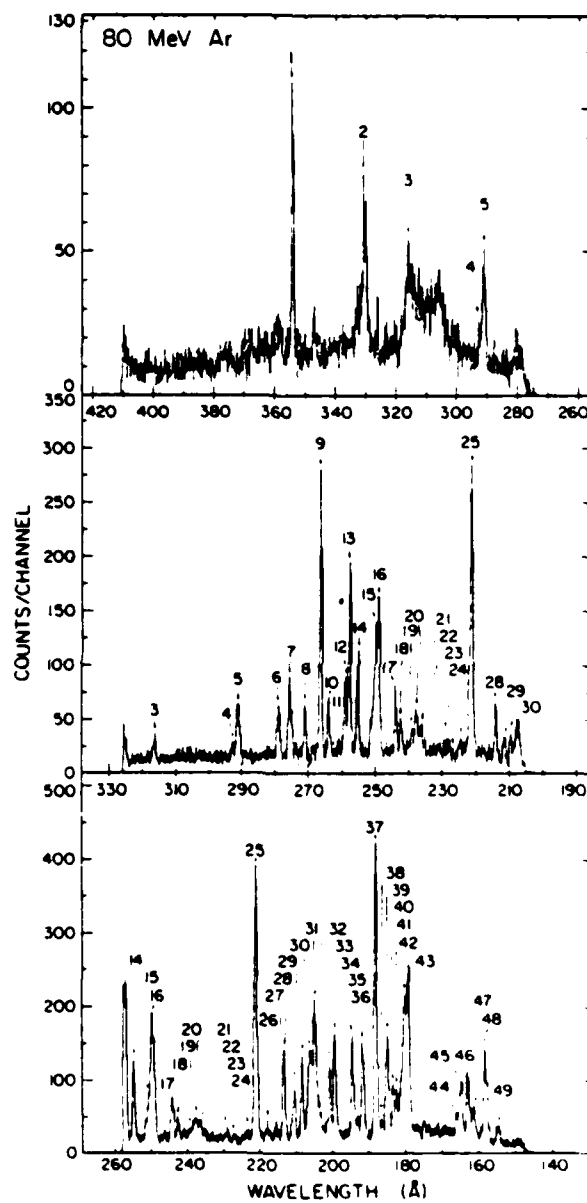


Fig. 34. Microchannel plate spectra of 80 MeV argon taken at spectrometer odometer settings of 11 300, 10 000, and 8 800 from top to bottom, respectively.

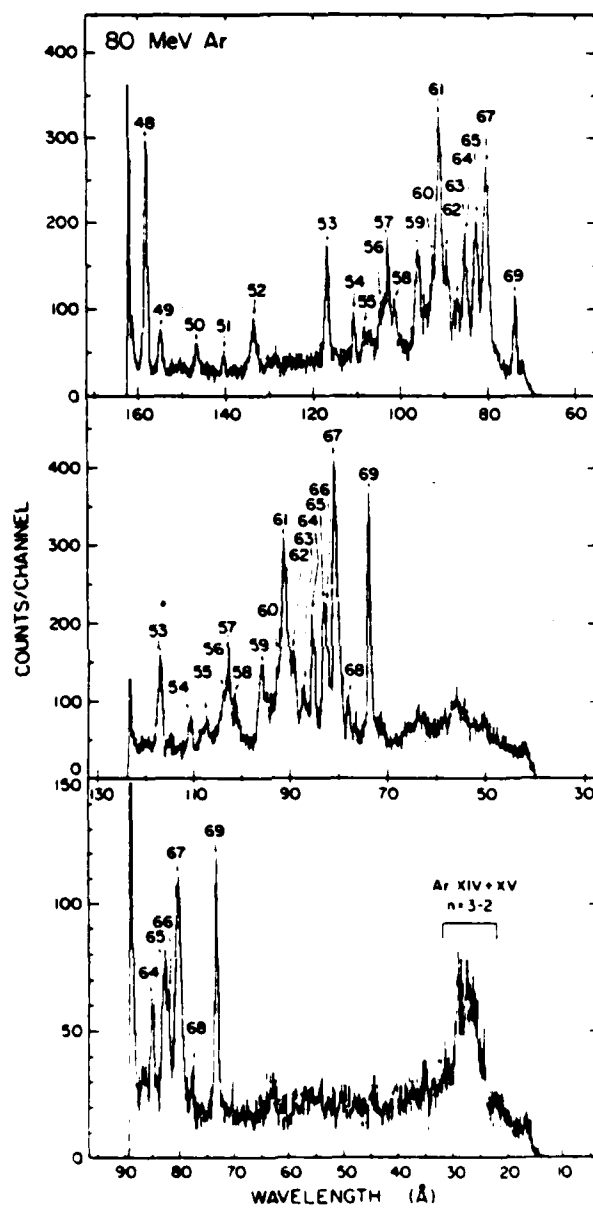


Fig. 35. Microchannel plate spectra of 80 MeV argon taken at spectrometer odometer settings of 6.800, 5.800, and 4.800 from top to bottom, respectively.

the same spectrometer positions as the top two spectra in Fig. 35 (these are shown as the top two spectra in Fig. 24). The same wavelength calibration polynomials for the numerous well known neon lines in this wavelength region were then used to determine the wavelengths of the argon lines.

To make the assignments of lines in the following tables more meaningful, partial level diagrams of $n = 2-2$ transitions in Ar XIII, Ar XIV and Ar XV are given in Figs. 36-38. The J-J multiplet structure within various groups were generally resolvable and the (final state-initial state) J values are shown in the figures following the wavelengths. Dashed lines in the figures represent lines which were not observed.

TABLE 21. 80 MeV Ar XIII line assignments.

Line #	Wavelength (Å) Measured	Strength ^b	Transition ^c	Theory (t) or Other Measurement (m) ^d
18	242.3	vw	$(2s^2 2p^2)^3 P_1 - (2s 2p^3)^3 D_2$	242.23 (m)
19	239 ± 1	vw	$n = 4 - 5$	239.6^e (t)
21	236.5	vw, b	$(2s^2 2p^2)^3 P_0 - (2s 2p^3)^3 D_1$	236.27 (m)
26	218.1	vw	$(2s 2p^3)^3 P_2 - (2p^4)^3 P_2$	218.18 (t)
29	210.6	w	$(2s^2 2p^2)^3 P_1 - (2s 2p^3)^3 P_1$	210.46 (m)
38	186.3	vw	$(2s^2 2p^2)^1 S_0 - (2s 2p^3)^1 P_1$	186.38 (m)
39	184.9	m	$(2s^2 2p^2)^1 D_2 - (2s 2p^3)^1 D_2$	184.90 (m)
41	182.2	w	$(2s 2p^3)^3 D_2 - (2p^4)^3 P_1$	182.38 (t)
45	164.8	m	$(2s^2 2p^2)^3 P_2 - (2s 2p^3)^3 S_1$	164.80 (m)

TABLE 21. Continued

Line #	Wavelength (Å) ^a Measured	Strength ^b	Transition ^c	Theory (t) or Other Measurement (m) ^d
46	162.9	m	$(2s^2 2p^2) \ ^1D_2 - (2s 2p^3) \ ^1P_1$	162.96 (m)
47	161.5	w	$(2s^2 2p^2) \ ^3P_1 - (2s 2p^3) \ ^3S_1$	161.61 (m)
49	155.0	m	$n = 4 - 6$	155.3 (t)

^a Wavelength accuracy ± 0.2 Å unless shown otherwise.

^b Relative intensity (arbitrary): vs>2000, 2000>s>1000, 1000>m>400, 400>w>200, 200>vw, b = blend.

^c Transition : inner shells filled when not shown.

^d Reference 105 theoretical or experimental values unless otherwise shown. All lines compared to theoretical values are newly observed and for intershell transitions, they are newly assigned.

^e Calculated by the Ritz formula.

TABLE 22. 80 MeV Ar XIV line assignments.

Line #	Wavelength (Å) ^a Measured	Strength ^b	Transition ^c	Theory (t) or Other Measurement (m) ^d
-	282.3	vw	$(2s 2p^2) \ ^2P_{3/2} - (2p^3) \ ^2P_{1/2}$	282.28 (t)
6	279.0	w	$(2s 2p^2) \ ^2P_{3/2} - (2p^3) \ ^2P_{3/2}$	279.04 (t)
13	257.4	m,b	$(2s^2 2p) \ ^2P_{3/2} - (2s 2p^2) \ ^2D_{5/2}$	257.37 (m)
15	250.5	w,b	$(2s 2p^2) \ ^2S_{1/2} - (2p^3) \ ^2P_{3/2}$	250.87 (t)
16	249.0	s,b	$(2s 2p^2) \ ^2D_{5/2} - (2p^3) \ ^2D_{5/2}$	248.94 (t)
17	243.8	w	$(2s^2 2p) \ ^2P_{1/2} - (2s 2p^2) \ ^2D_{3/2}$	243.79 (m)
20	237.5	w	$n = 5 - 7$	237.3 ^e (t)
28	213.4	m	$(2s 2p^2) \ ^4P_{5/2} - (2p^3) \ ^4S_{3/2}$	213.45 (m)
30	208.3	m	$(2s 2p^2) \ ^4P_{3/2} - (2p^3) \ ^4S_{3/2}$	208.35 (m)
31	206.1	m	$n = 4 - 5$	205.7 ^f (t)
32	204.7	s,b	$(2s 2p^2) \ ^4P_{1/2} - (2p^3) \ ^4S_{3/2}$	204.64 (m)

TABLE 22. Continued

Line #	Wavelength (Å) ^a Measured	Strength ^b	Transition ^c	Theory (t) or Other Measurement (m) ^d
--	203.6	m, b	$(2s^2 2p) \ ^2P_{3/2} - (2s2p^2) \ ^2S_{1/2}$	203.35 (m)
33	200.7	m	$(2s2p^2) \ ^2D_{3/2} - (2p^3) \ ^2P_{1/2}$	200.51 (t)
34	199.2	m, b	$(2s2p^2) \ ^2D_{5/2} - (2p^3) \ ^2P_{3/2}$	199.27 (t)
35	194.4	m	$(2s^2 2p) \ ^2P_{1/2} - (2s2p^2) \ ^2S_{1/2}$	194.39 (m)
36	191.5	m	$(2s^2 2p) \ ^2P_{3/2} - (2s2p^2) \ ^2P_{1/2}$	191.35 (m)
37	188.1	vs, b	$(2s^2 2p) \ ^2P_{3/2} - (2s2p^2) \ ^2P_{3/2}$	187.95 (m)
40	183.3	m	$(2s^2 2p) \ ^2P_{1/2} - (2s2p^2) \ ^2P_{1/2}$	183.41 (m)
42	180.1	s	$(2s^2 2p) \ ^2P_{1/2} - (2s2p^2) \ ^2P_{3/2}$	180.29 (m)
52	133.7	m	n = 4 - 6	133.5 ^f (t)
54	110.9	w	n = 4 - 7	110.5 ^e (t)
61	91.3	vs	$(3d) \ ^2D - (4f) \ ^2F$	91.3 ^f (t)

^aWavelength accuracy ± 0.2 Å unless shown otherwise.^bRelative intensity (arbitrary): vs>2000, 2000>s>1000, 1000>m>400, 400>w>200, 200>vw, b = blend.^cTransition : inner shells filled when not shown.^dReference 105 theoretical or experimental values unless otherwise shown. All lines compared to theoretical values are newly observed and for intershell transitions^g they are newly assigned.^eCalculated by the Ritz formula⁸.^fCalculated by the Dirac-Fock method of reference 106.

TABLE 23. 80 MeV Ar XV line assignments.

Line #	Wavelength (Å) ^a Measured	Strength ^b	Transition ^c	Theory (t) or Other Measurement (m) ^d
2	330.6 \pm 0.4	w	$(2s5g) \ ^3G - (2s6h) \ ^3H$	331.3 ^e (m)
7	275.7	m, b	$(2s2p) \ ^3P_2 - (2p^2) \ ^3P_1$	275.93 ^f (m)

TABLE 23. Continued

Line #	Wavelength (Å) Measured	Strength ^b	Transition ^c	Theory (t) or Other Measurement (m) ^d
8	271.0	w	$(2s2p) \ ^3P_1 - (2p^2) \ ^3P_0$	270.98 ^f (m)
9	266.2	s	$(2s2p) \ ^3P_2 - (2p^2) \ ^3P_2$	266.22 (m)
10	263.6	w	$(2s2p) \ ^3P_1 - (2p^2) \ ^3P_1$	263.62 ^f (m)
12	258.7	m,b	$(2s2p) \ ^3P_0 - (2p^2) \ ^3P_1$	258.74 ^f (m)
13	257.4	s,b	$(2s2p) \ ^1P_1 - (2p^2) \ ^1S_0$	257.53 ^f (m)
14	254.8	m,b	$(2s2p) \ ^3P_1 - (2p^2) \ ^3P_2$	254.81 ^f (m)
22	229.2	vw	$(2s2p) \ ^3P_2 - (2p^2) \ ^1D_2$	228.85 ^g (t)
25	221.2	vs	$(2s^2) \ ^1S_0 - (2s2p) \ ^1P_1$	221.12 (m)
43	179.1	s,b	$(2s4f) \ ^3F - (2s5g) \ ^3G$	179.3 ^e (t)
53	117.0	s	n = 4 - 6	116.3 ^h (t)
59	96.2	s,b	n = 4 - 7	96.2 ^h (t)
65	83.0	vs,b	$(2s3d) \ ^3D - (2s4p) \ ^3P$	83.2 ^e (t)
66	82.4	s,b	$(2s3p) \ ^3P - (2s4s) \ ^3S$	82.2 ^e (t)
67	80.7	vs	$(2s3d) \ ^3D - (2s4f) \ ^3F$	80.6 ^e (t)
68	77.8	w	$(2s3p) \ ^3P - (2s4d) \ ^3D$	77.9 ^e (t)

^aWavelength accuracy ± 0.2 Å unless shown otherwise.

^bRelative intensity (arbitrary): vs>2000, 2000>s>1000, 1000>m>400, 400>w>200, 200>vw, b = blend.

^cTransition : inner shells filled when not shown.

^dReference 105 theoretical or experimental values unless otherwise shown. All lines compared to theoretical values are newly observed and for intershell transitions, they are newly assigned.

^eCalculated by the Dirac-Fock method of reference 106.

^fPlasma values reported in reference 107.

^gEmpirical calculation reported in Reference 108.

^hCalculated by the Ritz formula.

TABLE 24. 80 MeV Ar XVI line assignments.

Line #	Wavelength (Å) ^a Measured	Strength ^b	Transition ^c	Theory (t) or Other Measurement (m) ^d
1	354.2 ± 0.4	m	(2s) ² S _{1/2} - (2p) ² P _{3/2}	353.8 (m)
4	292.6	vw	n = 6 - 8	292.9 ^e (t)
5	290.8	w	n = 5 - 6	291.1 ^e (t)
48	158.3	s	n = 4 - 5	158.2 ^e (t)
50	146.7	w	2nd. Ord. 73.4	---
57	103.1	vs	n = 4 - 6	102.5 ^e (t)
64	85.3	vs	n = 4 - 7	84.6 ^e (t)
69	73.4	vs	(3d) ² D - (4f) ² F	73.1 ^e (t)

^aWavelength accuracy ± 0.2 Å unless shown otherwise.

^bRelative intensity (arbitrary): vs>2000, 2000>s>1000, 1000>m>400, 400>w>200, 200>vw, b = blend.

^cTransition : inner shells filled when not shown.

^dReference 105.

^eCalculated by the Dirac-Fock method of reference 106.

The $\Delta n \neq 0$ lines were assigned by comparing the observed wavelengths to calculated values obtained by two methods. A number of relativistic Dirac-Fock calculations using the program written by Desclaux¹⁰⁶ were made to calculate accurate energy levels for Li-like, Be-like and B-like $n = 2, 3, 4$, and 5 levels. The accuracy of the Dirac-Fock intershell calculations is within 0.1 Å. A few less accurate Ritz formula calculations (Eq. 3.1) for additional intershell transitions from higher levels were made when it became apparent that transitions from principal quantum numbers as high as 7 were observed in some Rydberg series. The nonrelativistic Ritz formula calculations are

Ar XIII 6 Electrons

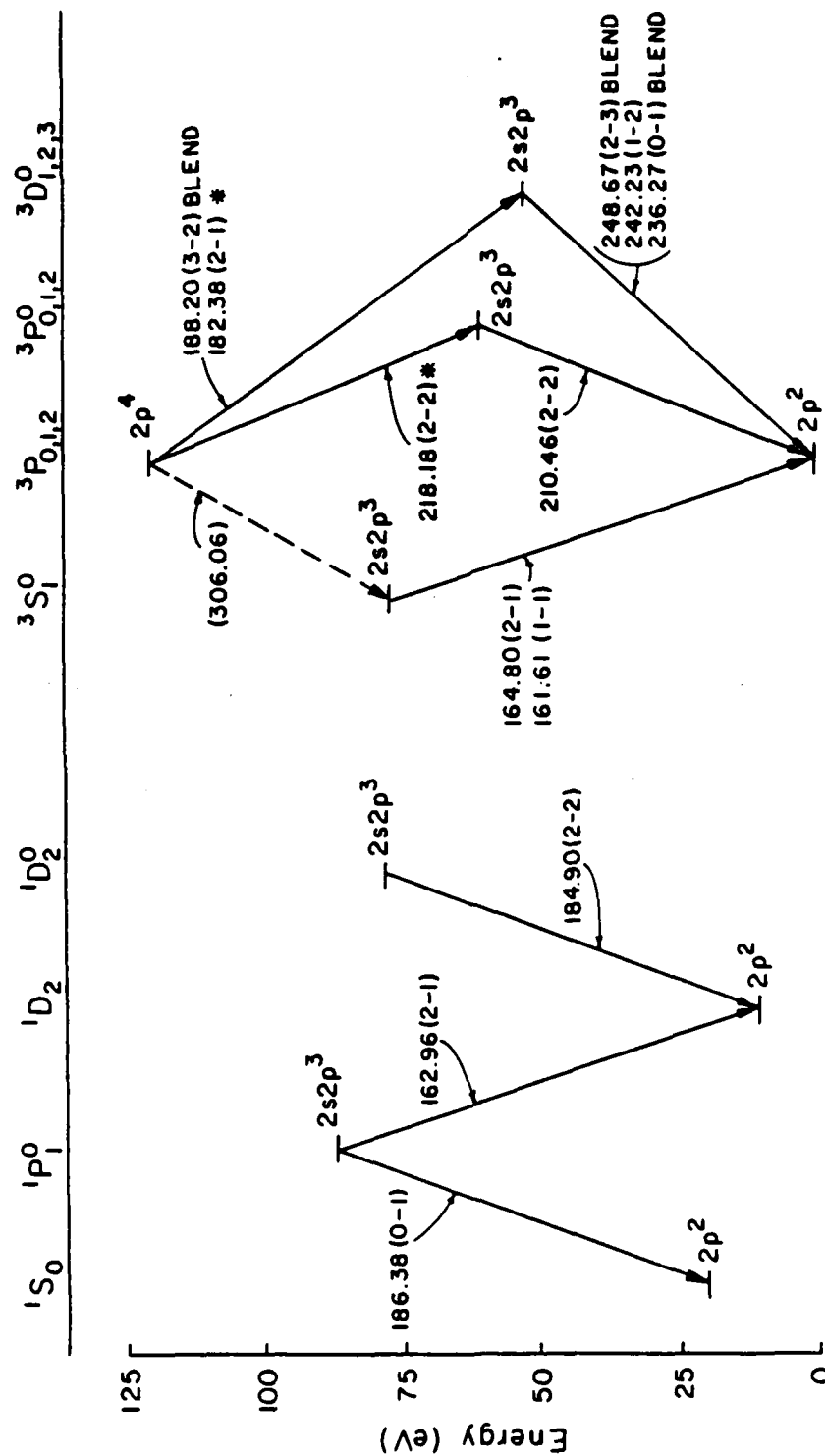


Fig. 36. Partial energy level diagram of Ar XIII. Wavelengths are given in Angstroms.

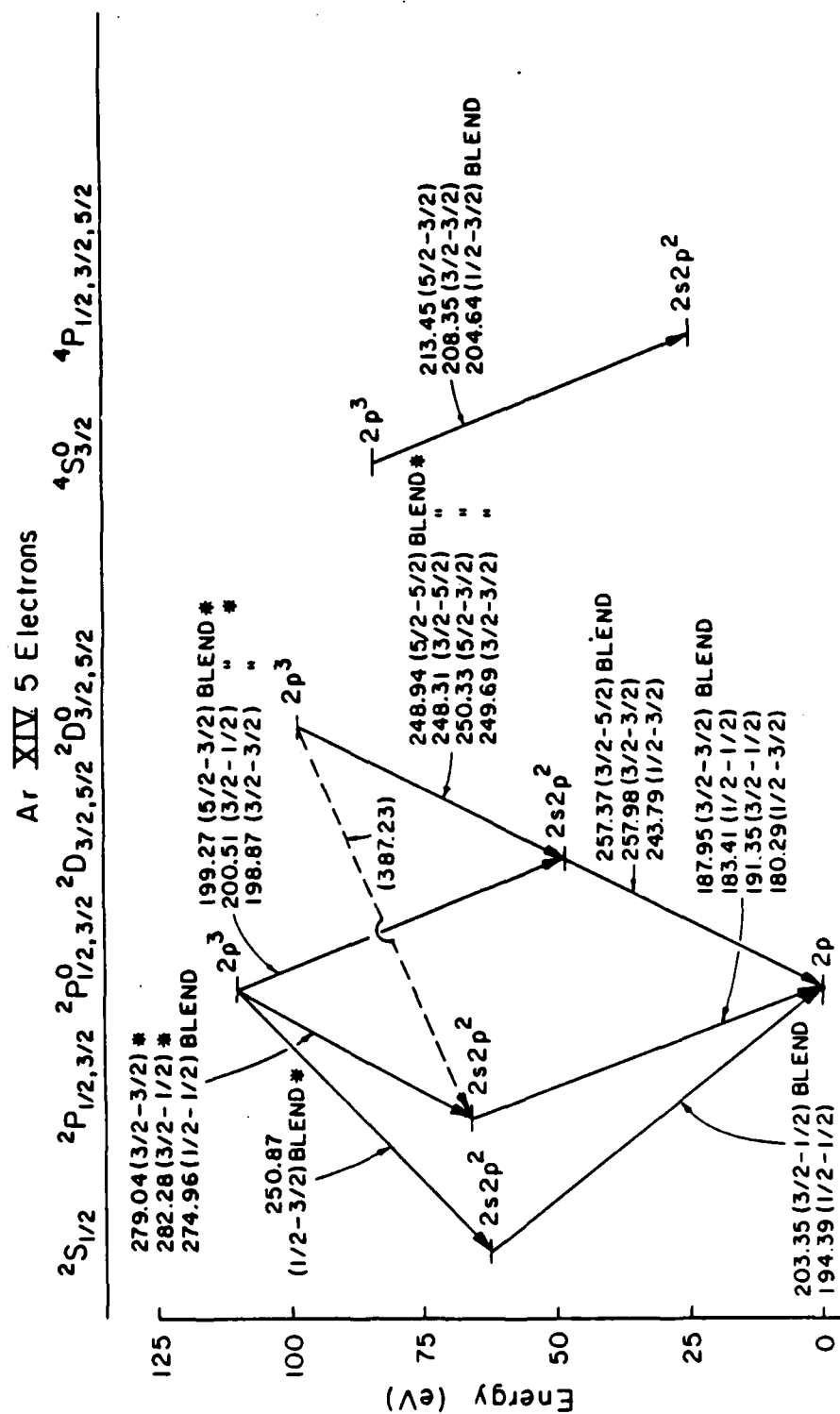


Fig. 37. Partial energy level diagram of Ar XIV. Wavelengths are given in Angstroms.

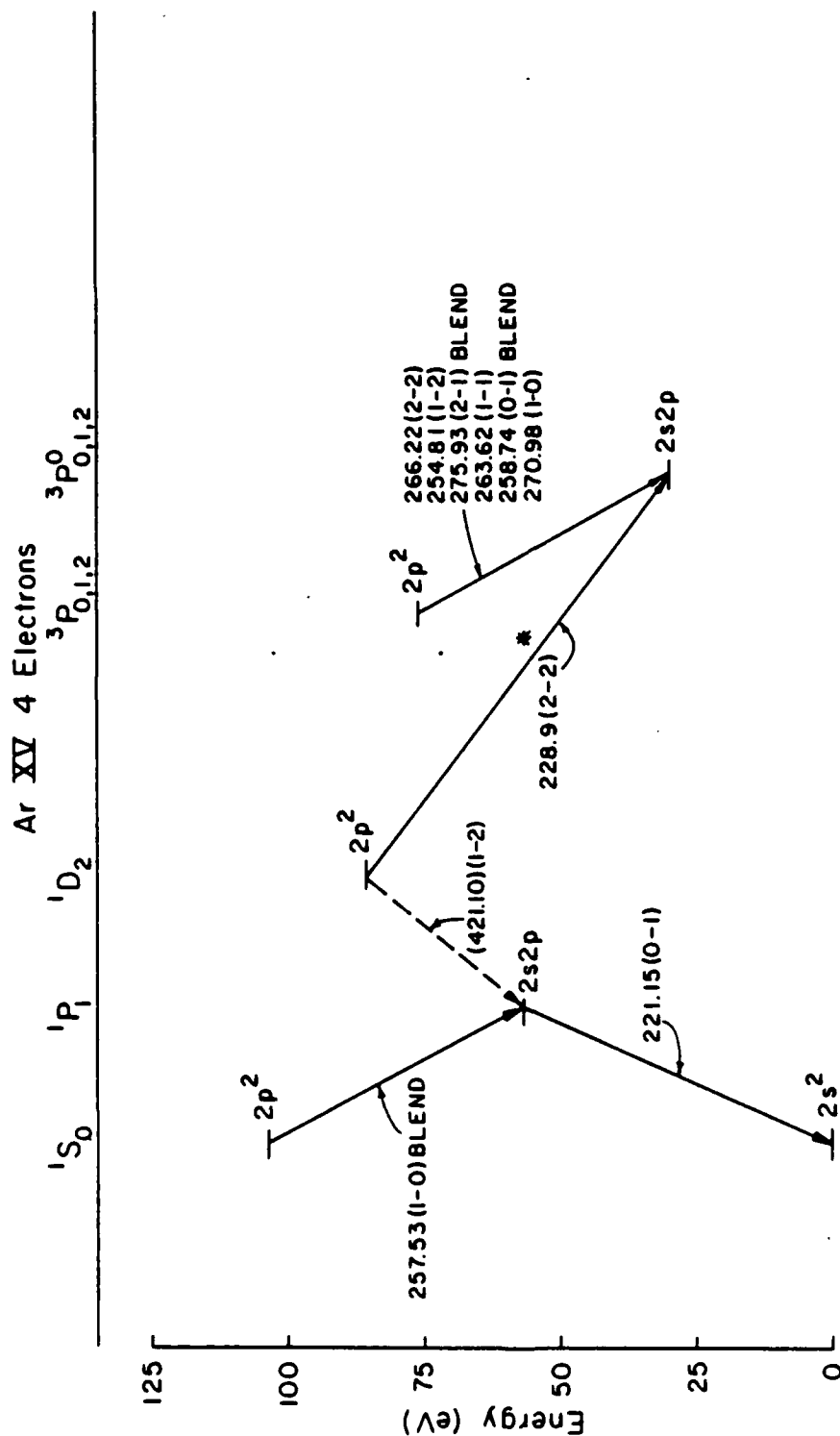


Fig. 38. Partial energy level diagram of Ar XV. Wavelengths are given in Angstroms.

expected to be accurate within 0.2 Å or less for $\Delta n \neq 0$ transitions based upon comparisons with the results of the Dirac-Fock calculations.

Whereas independent-particle model calculations, e.g. single-configuration Dirac-Fock, give accurate energies for intershell transitions ($\Delta n \neq 0$), they are not at all accurate for intrashell ($\Delta n = 0$) transitions. This inaccuracy results from the neglect of electron correlation effects which are significant and caused by the interpenetration of the electrons of the same principal quantum number. Proper treatment of electron correlation has provided a challenge to theorists and numerous attempts have been made to calculate accurate $n=2-2$ transition energies. For example, Cheng *et al.*¹⁰⁹ used multiconfiguration Dirac-Fock calculations with a three-configuration basis of $2s^2$, $2s2p$, and $2p^2$. Edlen¹⁰⁸ used a semi-empirical method of fitting a nearly constant function through experimental points. Glass¹¹⁰ concluded that an expanded basis set including $n>2$ terms was needed to achieve values within 1% of the semi-empirical values and that more experimental data was sorely needed.

Table 25 provides a comparison between experimental and theoretical wavelength values for Li-like and Be-like argon. Since the Li-like ion is nearly hydrogenic (only one electron outside the closed $n=1$ shell), neglect of electron correlation does not result in serious error.

TABLE 25. Comparison of experimental and theoretical wavelengths (Å) for n=2-2 Ar XVI and Ar XV.

Transition ^a		Wavelength (Å)				
		Measured		Theoretical		
		This work	Other ^b	SCDF ^c	MCDF ^d	Semi-emp. ^e
Ar XVI	$2S_{1/2} - 2P_{1/2}$ ---		389.12	389.92	387.4	389.08
Ar XVI	$2S_{1/2} - 2P_{3/2}$	354.2	353.80	351.33	352.6	353.87
Ar XV (DE)	$3P_2 - 3P_1$	275.7	275.92	273.88	274.4	275.89
Ar XV (DE)	$3P_1 - 3P_0$	271.0	270.88	251.70	269.4	270.96
Ar XV (DE)	$3P_2 - 3P_2$	266.2	266.22	263.74	264.6	266.20
Ar XV (DE)	$3P_1 - 3P_1$	263.6	263.68	256.91	262.3	263.65
Ar XV (DE)	$3P_0 - 3P_1$	258.7	258.77	261.96	257.5	258.73
Ar XV (DE)	$3P_1 - 3P_2$	254.8	254.82	247.97	253.4	254.79
Ar XV (DE)	$1P_1 - 1S_0$	257.4	257.42	335.00	257.2	257.34
Ar XV (DE)	$1P_1 - 1D_2$ ---		---	423.88	425.0	421.17
Ar XV (R)	$1S_0 - 1P_1$	221.2	---	237.25	214.7	221.14
Ar XV (DE)	$3P_2 - 1D_2$	229.2	---	223.24	223.8	228.86

^aA singly excited, resonance line is denoted (R) and a doubly excited line is denoted (DE).

^bPlasma values from reference 110.

^cSingle-configuration Dirac-Fock (SCDF)¹⁰⁶.

^dMulticonfiguration Dirac-Fock (MCDF)¹⁰⁹.

^eSemi-empirical prediction¹⁰⁸.

Several n=2-2 lines that were expected to appear in the spectra, based upon observed lines within the same multiplet group, were completely blended with lines from other charge states. Examples of overlaps in the region that was selected for lifetime analysis are

shown in Table 26. When one line dominated the blend, the lifetime measurement reflected this dominance.

TABLE 26. Observed line blends in the 295-185 Å region.

Stronger line ^a	Wavelength (Å)	Hidden line(s)	Wavelength (Å)
Ar XIV (R) $^2P_{3/2} - ^2D_{5/2}$	257.5	Ar XV (DE) $^1P_1 - ^1S_0$	257.3
Ar XIV (DE) quartet $^2D - ^2D$	250.3-248.3	Ar XIV (DE) $^2S_{1/2} - ^2P_{3/2}$	250.9
" "	"	Ar XIII (DE) $^3P_2 - ^3D_2$	249.4
" "	"	Ar XIII (DE) $^3P_2 - ^3D_3$	248.7
Ar XIII (R) $^3P_2 - ^3P_2$	210.5	Ar XIII (DE) $^3P_2 - ^3P_1$	211.0
" "	"	Ar XIII (DE) $^3P_2 - ^3P_2$	210.5
Ar XIV (R) n=4-5	206.4	Ar XIII (R) $^3P - ^3P$	206.0-205.2
" "	"	Ar XIV (DE) $^4P_{1/2} - ^4S_{3/2}$	204.6
" "	"	Ar XIV (DE) $^2P_{3/2} - ^2S_{1/2}$	203.4
Ar XIV (R) $^2P_2 - ^2P_2$	188.0	Ar XIII (DE) $^3D - ^3P$	188.2-187.8

^aA singly excited, resonance line is denoted (R) and a doubly excited line is denoted (DE).

A number of lines have not been assigned and are listed in Table 27. In most cases these lines are weak components of stronger lines and require better resolution and statistics to make an accurate assignment. In fact, it may be necessary to determine the dependence of intensity on projectile velocity in order to classify them according to charge state.

TABLE 27. Unassigned lines in 80 MeV Ar.

Line #	Measured ^a Wavelength (Å)	Strength ^b	Line #	Measured ^a Wavelength (Å)	Strength ^b
3	316.3	vw	55	108.7	vw
11	260.6	vw	56	104.6	m,b
23	226.8	vw	58	102.0	m,b
24	224.6	vw	60	93.7	s,b
27	215.4	vw	62	89.5	s,b
44	165.0	w,b	63	87.4	s
51	140.5	vw			

^aWavelength accuracy ± 0.2 Å unless shown otherwise.

^bRelative intensity (arbitrary): vs>2000, 2000>s>1000, 1000>m>400, 400>w>200, 200>vw, b = blend.

Altogether, of the 30 newly observed lines, 21 were due to transitions from higher levels to the n=3, 4, 5, and 6 levels, and nine were due to n=2-2 transitions from doubly excited states. All of the 27 previously reported lines in Tables 18-21 were due to n=2-2 transitions. Also, a total of 13 lines remain yet unassigned. In addition, a number of Ar XIII and Ar XIV lines were not resolved from the stronger Ar XIV and Ar XV lines, respectively, in the wavelength region of 280 to 155 Å. Second order reflections were not a problem as in most cases they were overwhelmed by stronger first order lines. Strong transitions were observed from the n=5 and n=6 levels to the n=4 level, but transitions from these same upper levels to the n=3 level in the calculated wavelength region of 63 to 42 Å were not prominent. Some structure was seen in this region but the present statistics were too poor to classify any lines.

Finally, the one region that could benefit significantly by additional measurements with better resolution and better statistics is the wavelength region between 120 and 42 Å where the bulk of upper level transitions to the $n=3$ and $n=4$ levels for few electron Ar occur. This region contains many unassigned lines and multiplets of overlapping $n=3-4$, $n=3-5$, $n=3-6$, $n=4-6$ and $n=4-7$ transitions of the various charge states of 80 MeV Ar. However, a resolution better than the 0.8 Å used here is necessary to unambiguously classify all the lines. The situation is similar to a reported study¹¹¹ of Si $n=3-4$ lines where even with a resolution of less than 0.01 Å, many of the lines were still unresolved.

D. Lifetimes of Transitions in the 292 to 185 Å region

The same experimental arrangement for beam-foil lifetime measurements described in Chapter III was used to obtain $\Delta n=0$ transition lifetimes for Be-like, B-like, and some C-like argon. The microchannel plate detector was positioned at an odometer setting of 9.500 so as to view the spectral region from 295 to 180 Å. The 100 μm slit width resulted in a 0.75 Å resolution in the center of the plate and 0.85 Å at the ends of the plate. A carbon foil of thickness 22 $\mu\text{g}/\text{cm}^2$ was moved initially by steps of 0.127 mm and then by multiples of 0.127 mm out to 10.9 mm, comprising a total time interval of 560 psec. Sample spectra taken at several foil positions, in which the persistence of some lines at greater than 400 psec is evident, are shown in Fig. 39.

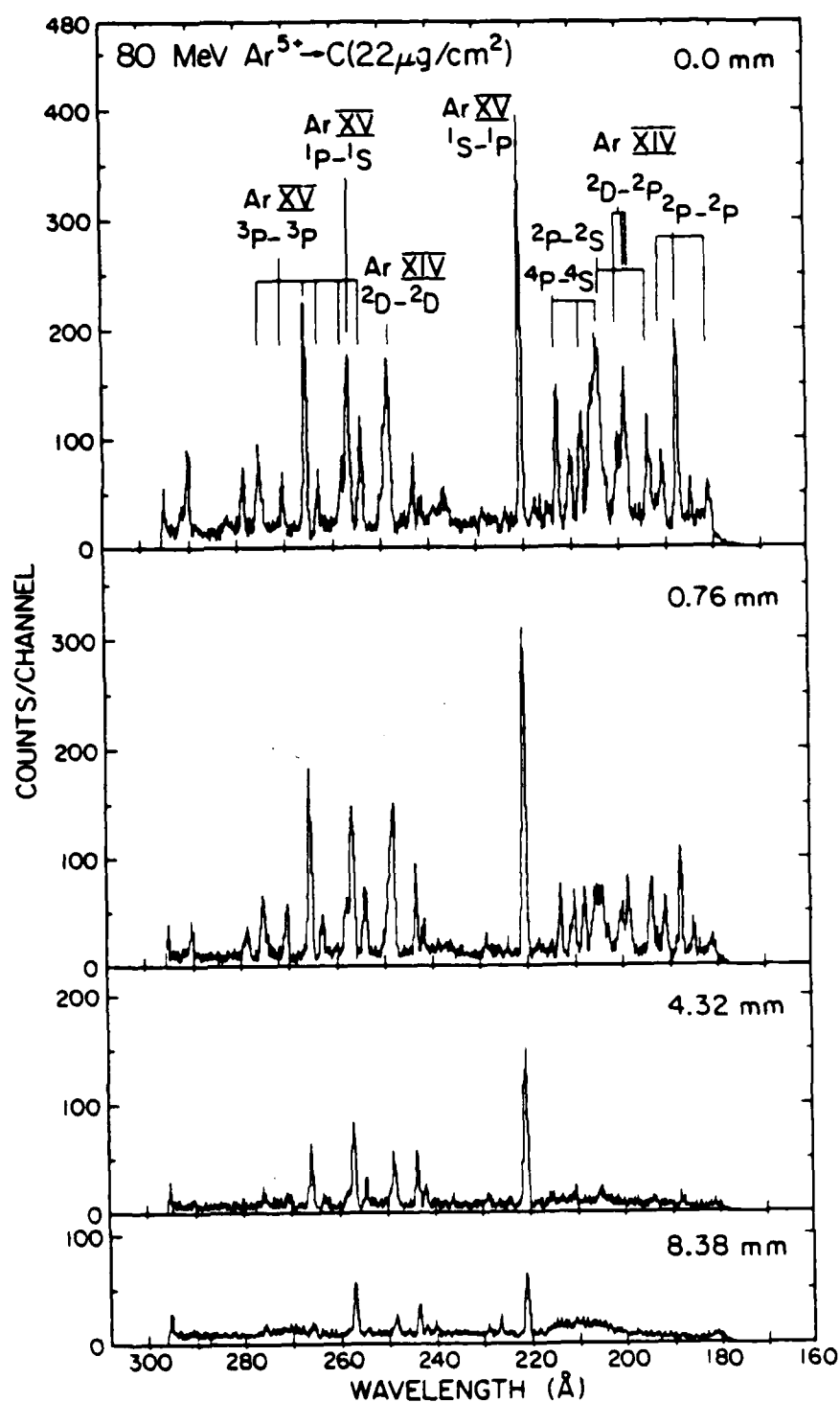


Fig. 39. Example of argon spectra taken at different foil positions representing delay times from top to bottom of: 0 psec, 39 psec, 220 psec, and 428 psec.

The data at each foil position were normalized to a specified number of beam monitor counts measured in a faraday cup downstream. The integrated intensity of each peak was analyzed using the Homer⁸² program to obtain the lifetimes of the various components. The sources of error were the same as for the neon data shown in Table 17.

Decay curves for 26 argon lines are included in the Appendix. The solid lines through the data represent the multiexponential fit given by the Homer program. The lifetime results are presented in Table 28.

TABLE 28. Lifetimes of Ar XVI, Ar XV, and Ar XIV.

Wave-length (Å)	Ion	Upper Level	Lifetime (psec)		Replen- ishment Ratio ^b
			This work ^a prompt	Other cascade values	
290.8	Ar XVI	n=6	10(20%), 66(15%)	9.2 ^c	0.47
279.0	Ar XIV*	² P _{3/2}	47(10%) ---	50 ^d , 45 ^e	---
275.9	Ar XV*	³ P ₁	118(10%) ---	132 ^d , 131 ^e	---
271.0	Ar XV*	³ P ₀	5(100%), 149(10%) gic	139 ^d , 137 ^e	1.1
266.2	Ar XV*	³ P ₂	142(10%) ---	171 ^d , 128 ^e	---
263.6	Ar XV*	³ P ₁	121(10%) ---	133 ^d , 131 ^e	---
258.7	Ar XV*	³ P ₁	133(10%) ---	133 ^d , 131 ^e	---
257.3	Ar XIV	² D _{5/2}	290(10%) blend	284 ^d , 294 ^e	---
254.7	Ar XV*	³ P ₂	134(10%) ---	131 ^d , 128 ^e	---
249.2	Ar XIV*	² D _{5/2}	143(10%) blend	107 ^d , 102 ^e	---
243.9	Ar XIV	² D _{3/2}	66(22%), 260(11%) gic	240 ^d , 245 ^e	2.1
242.2	Ar XIII	³ D ₂	34(32%), 297(12%) gic	224 ^d , 225 ^e	1.7
229.1	Ar XV*	¹ D ₂	742(50%) ^f	465 ^e	---

TABLE 28. Continued

Wave-length (Å)	Ion	Upper Level	Lifetime (psec)		Other values	Replen- ishment Ratio ^b
			This work ^a prompt	cascade		
221.2	Ar XV	$1P_1$	157(43%), 410(95%)	99,459 ^e , 99,458 ^e		0.20
213.6	Ar XIV*	$4S_{3/2}$	44(10%) ---		41 ^d , 40 ^e	---
210.7	Ar III	$3P_2$	153(10%) ---		100 ^d , 95 ^e	---
208.4	Ar XIV*	$4S_{3/2}$	47(10%) ---		41 ^d , 40 ^e	---
206.4	Ar XIV	n=5	11(10%), 116(10%)		6.1 ^c	0.43
205.4	Ar III	$3P_2$	13(10%), 120(10%)blend		100 ^d , 95 ^e	0.40
204.5	Ar XIV* ?	$4S_{3/2}$	12(10%), 85(12%)blend		41 ^d , 40 ^e	0.35
200.6	Ar XIV*	$2P_{1/2}$	57(10%) ---		50 ^d , 43 ^d	---
199.1	Ar XIV*	$2P_{3/2}$	44(10%) ---		51 ^d , 45 ^e	---
194.2	Ar XIV	$2S_{1/2}$	94(10%) ---		60 ^d , 60 ^e	---
191.3	Ar XIV	$2P_{1/2}$	40(23%) ---		41 ^d , 40 ^e	---
188.0	Ar XIV	$2P_{3/2}$	43(10%) 112(39%)blend		36 ^d , 37 ^e	0.15
185.0	Ar XIII	$1D_1$	61(10%) ---		33 ^d , 32 ^e	---

^aSome measurements gave evidence to a growing-in cascade (gic) and are so indicated. A few measurements were taken of a blend of overlapping lines.

^bReference 9.

^cScaled hydrogenic approximation where the hydrogen transition probability is multiplied by a factor $1/12 (Z-\sigma)^4$, where $(Z-\sigma)$ = the spectral number of the ion, σ , e.g., 16 for Ar XVI.

^dFrom the weighted oscillator strengths given in reference 113.

^eFrom the transition probabilities given in reference 109.

^fThe uncertainty of this measurement is large since only close to one decay length was measured rather than the preferred 4 to 10 decay lengths.

*An asterisk denotes doubly excited states.

The main difference in the decay curves for argon versus those for neon was the absence of prominent long-lived cascade contributions to the relatively long lifetime argon intrashell transitions. Generally, the example in Fig. 3a was typical of the neon decay curves, as opposed to the argon decay curves which resembled all three examples in Fig. 3. Another significant difference between neon and argon that was that many of the excited levels measured in the neon data had only one electric dipole transition decay path (no branching). However, most of the argon excited levels had many lower levels to feed and therefore had significant branching ratios. This fact did not influence the lifetime measurements, but had to be taken into account when converting either theoretical transition probabilities¹⁰⁹ (Eq. 1.18) or absorption oscillator strengths¹¹³ into lifetimes (Eq. 1.19 and Eq. 3.6) to compare with the measured lifetimes, as in Table 29.

To compare experimental and theoretical transition probabilities directly, branching ratios are used. As stated in Chapter III, the fraction formed by the ratio of the probability for the transition represented by the actual line to the total transition probability from that level is the branching ratio (Eq. 3.6). Branching ratios can be found experimentally by measuring the intensities of all transitions from a given level with an intensity calibrated spectrometer. Experimental branching ratios using Eq. 3.6 were compared to theoretical values when all lines fell within the experimental wavelength region and were not too heavily blended. The experimental values were obtained by normalizing to a value of unity the sum of all relative populations of a state determined by Eq. 3.4. The results are

shown in Table 29. All experimental values are in good agreement with theory except for the Ar xv 3P_2 state. The measured intensity of the line at 254.8 Å is three times greater than theory predicts. No other known Li-, Be-, B-, or C-like line is predicted or observed at this wavelength, so a blend is not suspected. Besides, the lifetime measurement gave a value that agreed well with theory for the 2^3P_2 state. This would not be expected if the line were blended.

E. Discussion of Lifetime Results

In general, there is excellent agreement between the experimental lifetime values in Table 28 and the theoretical ones. The few exceptions warrant further discussion.

The line at 271.0 Å shows evidence of a fast growing-in cascade. The Ar XV (DE) 2^3P_0 state has an empty 2s subshell and with two 2p electrons can only decay by an E-1 transition directly to the 2^3P_1 state with no branching. Any feeding into this state would most likely be via an intrashell transition from a state like (2p3d) 3^3D_1 with a lifetime of less than 1 picosecond. The other members of the Ar XV (DE) 2^3P group have maxima at the t=0 position in the decay curve analyses and are not characterized by a fast growing-in cascade. Therefore, the apparent intershell cascade may be an artifact of the statistics in the analysis. However, this illustrates an important advantage of using a position sensitive MCP; that is, the t=0 position is very well defined by the simultaneous collection of numerous decay curves, some of which have lifetimes much shorter than the experimental

TABLE 29. Comparison of selected Ar XV and Ar XIV experimentally determined branching ratios with theoretical values.

Ion ^a	Transition	Branching Ratio	
		Experimental ^b	Theory ^c
Ar XV (DE)	$^3P_2 - ^3P_2$	0.53	0.72
	$^3P_1 - ^3P_2$	0.47	0.28
Ar XV (DE)	$^3P_2 - ^3P_1$	0.41	0.38
	$^3P_1 - ^3P_1$	0.30	0.26
	$^3P_0 - ^3P_1$	0.27	0.37
Ar XIV (DE)	$^2P_{3/2} - ^2P_{3/2}$	0.36	0.34
	$^2D_{5/2} - ^2P_{3/2}$	0.49	0.52
	$^2D_{3/2} - ^2P_{3/2}$	---	0.14
	$^2S_{1/2} - ^2P_{3/2}$	---	0.14
Ar XIV (DE)	$^4P_{5/2} - ^4S_{3/2}$	0.44	0.48
	$^4P_{3/2} - ^4S_{3/2}$	0.38	0.34
	$^4P_{1/2} - ^4S_{3/2}$	---	0.18
Ar XIV (R)	$^2P_{1/2} - ^2P_{1/2}$	0.44	0.37
	$^2P_{3/2} - ^2P_{3/2}$	0.56	0.63

^aDoubly excited, empty 2s shell denoted as (DE), singly excited, resonance line (R).

^bWeak branching ratios less than 0.20 were not observed, therefore the theoretical value is assumed for normalization purposes.

^cReference 109.

time window. Definite growing-in cascades, such as seen in Ar XIV (R) at 243.9 Å and Ar XIII III (R) at 242.2 Å, are not misinterpreted due to uncertainty in the t=0 position.

The main lifetime component, 260 ps, of the Ar XIV (R) $2^2D_{3/2}$ transition compares very favorably with the theoretical values of 240 and 246 ps. The growing-in component of 66 psec appears to come from a blend of the two intrashell feeding transitions. These feeding transitions, with lifetimes of 45 and 104 psec, come from the doubly excited 2^2P and 2^2D states as shown in Fig. 37. In a similar manner, the Ar XIII (R) 2^3D_2 state has a single feeding transition of 26 psec from the 2^3P_3 doubly excited state, which at 188.0 Å is overwhelmed by the Ar XIV (R) 188.0 Å line and thus, can only be determined by analysis of the lifetime of the 242.2 Å line.

The line at 257.4 Å is a blend of the Ar XIV (R) $2^2D_{5/2}$ and the Ar XV (DE) 2^1S_0 both with unity branching ratios. The measured lifetime of 290 psec matches that of the Ar XIV line and shows no evidence of the faster 62 psec Ar XV line. Another blend at 249.2 Å involves four unresolved lines from Ar XIV (DE) 2^2D . The theoretical lifetime of this state, 102-104 psec, is still somewhat faster than the measured lifetime of 143 psec.

The dominating line at 221.2 Å is solely from the Ar XV (R) 2^1P_1 state. It might be expected that a measurement of the lifetime of this line would be accurate and simple since the statistics are so favorable and since no other line blends with it. However, this Be-like line is in fact quite difficult to analyze since it is fed by two other intrashell transitions -one having nearly the same lifetime -as shown in Fig. 38. The theoretical lifetime of this line is 99 psec and the principal cascade contributions are 62 psec for the 2^1S and 458 psec

for the 2^1D . The long lived contribution can be resolved from a multi-exponential fit of the lifetime of the 221.2 Å line. The 62 psec lifetime is too close to the 99 psec lifetime to resolve by means of a multi-exponential fit. Other methods to deal with lifetime blends have been developed, such as the "arbitrarily normalized decay curve" (ANDC) method⁸⁵. This method makes use of decay curves of all direct cascades in the analysis from the level of interest. Unfortunately, such a technique could not be used here since one cascade level was masked by a stronger transition at 257.4 Å and the other was outside the experimental wavelength range at 421.1 Å.

The experimental lifetime for Ar XIII (R) 2^3P_2 at 210.7 Å was found to exceed theory¹⁰⁹ by a factor of 1.6. Other experimental values reported for this C-like line exceed theory by similar factors. For example, this transition in Ne V, Mg VII, Al VIII¹¹⁴, Si IX IX¹¹⁵, and P X¹¹⁶ was found to exceed theory by factors of 1.6, 1.4, 1.5, 1.3, and 1.4, respectively.

Another line that had an experimental lifetime value considerably greater than theory¹⁰⁹ was the Ar XIII (R) 2^1D_2 line at 185.0 Å. The measured value of 61 psec exceeded theory by a factor of 1.9. Once again other experimental values for this C-like line were found to exceed theory by factors of 1.8, 1.5, 1.9, 2.0, 2.0 and 2.0 for Ne V¹¹⁴, Mg VII¹¹⁴, Al VIII¹¹⁴, Si IX¹¹⁵, P X¹¹⁶, and Cl XII¹¹⁷, respectively. The consistency in the experimental factors suggests that the theoretical value is in error.

One final remark about the experimental lifetimes concerns the unresolved group of lines at 206-204 Å. Three components were analyzed

at their respective wavelength positions as indicated in Table 25 and illustrated by the decay curves in the Appendix. A fast component dominated the decay curves followed by a slower cascade. The fast component (10-13psec) is due to the Ar XIV n=4-5 transition and the slow component (85-120 psec) is probably due to either the Ar XIII (R) 2^3P_2 at 205.2 Å with a measured lifetime of 153 psec at 210.7 Å or the Ar XIV (R) $2^2S_{1/2}$ at 203.4 Å with a measured lifetime of 94 psec at 194.2 Å. An analysis of the line strengths from multiplets of the three major lines in this group also indicates that the Ar XIV n=4-5 and the Ar XIV (R) 2^2S lines dominate this group.

CHAPTER V

CONCLUSION

A. Characterization of the Performance of a Position

Sensitive Microchannel Plate in the EUV

In this investigation, a grazing incidence spectrometer was modified to conduct beam-foil spectroscopy of ion beams accelerated by the Texas A&M University variable energy cyclotron. Neon and argon beam-foil measurements were made at beam energies of 2 MeV/amu, a factor of two higher than any previous studies. A wavelength calibration based on a second order equation of spectrometer position was found to result in an accuracy of $\pm 0.1 \text{ \AA}$. However, the inefficiency of the detector system with the normal exit slit/channel electron multiplier combination, which sampled only a fraction of an Angstrom per channel, severely limited the amount of spectral data that could be obtained within the available beam time.

To improve the efficiency, the spectrometer was adapted to use a position sensitive microchannel plate that allowed a 100 Angstrom wavelength range to be detected simultaneously. A careful study of the MCP detector system revealed the following:

- (1) the resolution over two thirds of the 50 mm wide plate was the same as with the double slit system.
- (2) the position information of the MCP was linear over 90% of the plate length and the spectrometer position correlated

directly with x-ray peak position, thereby permitting an accurate wavelength calibration ($\pm 0.1 \text{ \AA}$) using a second order polynomial fit of channel number versus wavelength.

- (3) a two order of magnitude improvement in detection efficiency was achieved, thus allowing the study of many lines under varying conditions, such as, with different material foils or varying foil positions.
- (4) simultaneous lifetime measurements for numerous lines were possible.

This latter feature allowed an accurate background subtraction at each foil position and ensured consistency of measurement; as all peaks were recorded simultaneously in one foil movement sequence, not by a continuous resetting of the foil to the starting position as required by the single channel detection method. The only disadvantage of the MCP detector was its sensitivity to the configuration of the electronic processing circuitry. Operating the detector with different amplifiers, gain settings, signal wires and/or voltage conditions made a new wavelength calibration necessary for each experimental setup. An additional improvement to the detection system might be accomplished through the use of a microchannel plate that has funneled micro-openings in the front surface. Such a feature is reported to increase the detection efficiency at grazing angles of incidence by several fold⁶⁵.

B. Beam-foil Study of Few-electron Neon Ions

A number of interesting observations resulted from the examination of the neon beam-foil data:

- (1) The branching ratio method of efficiency calibration gave a broad maximum nearly 50 Å greater than the expected maximum at the blaze wavelength of 20 Å. The reason for this behavior is likely due to surface conditions of the grating where low electron density oil could attenuate short wavelength lines due to the movement of the short wavelength cutoff in reflectivity to higher wavelengths as predicted for a less dense material.
- (2) The most populated charge state for the metal-foil-excited neon ions was Li-like as opposed to He-like for the carbon-foil-excited spectra. This reduction in charge state might be indicative of enhanced electron capture from the metal surface.
- (3) Among the He-like states, the 3^3S was more highly populated by the carbon foil than by the metal foils. As this was the only state for which this was the case, a mechanism such as a resonant electron transfer from the carbon to the 3s shell of a H-like neon ion is suggested. Experiments on other foils, such as Be and Al, Ti, Ni, Cu and Sn would provide additional information on the anomalous behavior of this state and allow

a target material comparison to calculations for electron capture.

- (4) The relative populations of both the carbon-excited and metal-excited neon ions showed a nonstatistical behavior with respect to orbital angular momentum. The lowest l states showed evidence of preferential population, which is consistent with an OBK prediction that electron capture proceeds as v^{-2l} . Hence, for 2 MeV/amu Ne, s states are predicted to be maximized for electron capture⁹⁹.
- (5) The yrast lines, which displayed heavy cascade feeding in the carbon-excited neon spectra (Ne VIII 3^2D , Ne IX 3^1D and 3^3D), showed little cascade feeding in the metal-excited spectra. This absence of contributions from high n, l (Rydberg) states could be due to several factors. On the one hand, high n state populations cannot exist within the foil longer than it takes to traverse a few lattice spacings due to collisional ionization. For the most part, these states must be populated as the ion exits from the rear of the foil by capture of an electron from the surface of the foil or from the convoy electrons traveling within the wake potential of the beam. The mechanism for post foil capture to high Rydberg states might be more effective for carbon-foils than for heavy metal foils. On the other hand, the presence of an electric field would cause Stark mixing of high Rydberg states which could then decay rapidly to low n, l vacancy states by a fast cascade transition resulting in a noticeable

loss of cascade feeding from these upper levels. Additional information pertaining to this question might be obtained by examining the effect of foil thickness on cascade feeding. Another approach would be to examine composite foils of a few $\mu\text{g}/\text{cm}^2$ of metal on carbon to determine the relative importance of surface effects versus bulk effects.

- (6) A number of new He-like lines were observed from high n levels feeding the Ne $n=3$ and $n=4$ levels. Another candidate for a beam-foil study would be 2 MeV/amu Mg. A number of new He-like lines could be classified and it would be of interest to look for changes in the relative populations of the $n=3$ levels of Mg in comparison to those observed for Ne.

C. Beam-foil Study of Few-electron Argon Ions

The argon beam-foil data confirmed wavelength predictions of 30 previously unobserved lines. The lifetime measurements of many of the $n=2-2$ transitions also agreed well with theory. Three lifetimes were found to exceed theory by a factors of 1.6, 1.6 and 1.8 : Ar XIII (R) 3P_2 , Ar XIV (R) $^2S_{1/2}$, and Ar XIII (R) 1D_2 , respectively. These findings were consistent with measurements of the same states of lower Z ions. Additional beam-foil examinations of highly ionized argon could be accomplished with a crystal spectrometer to examine the relative population of Li-like and Be-like $n=3$ to $n=2$ transitions which occur in the wavelength region 30-23 Å (413-539 eV).

D. Possible Future Developments

In summary, a number of interesting beam-foil effects that were observed were made possible by the efficiency increase in the spectrometer system. Several additional experiments, can be accomplished with this experimental arrangement to expand our understanding of beam-foil excitation mechanisms. Of these, the examination of the effect of excitation by different foil materials and/or thicknesses is recommended so as to elucidate the mechanism of electron capture. A comparison between layered foils and single composition foils is also recommended since such a dramatic change in the composition of the EUV spectra of 40 MeV neon was achieved by changing from a carbon foil to a heavy metal foil. These comparisons can be made without conducting lifetime measurements if care is taken to limit cascade contributions to the prompt spectra by limiting the time window of the spectrometer system either by use of a smaller grating mask or by means of an auxiliary slit mounted close to the target.

REFERENCES

1. P. L. Hagelstein, *Plasma Phys.* 25, 1345 (1983).
2. D. J. Nagel and W. L. Baun in X-Ray Spectroscopy, edited by L. V. Azaroff (McGraw-Hill, New York, 1974), pp. 445-532.
3. S. Bashkin, L. Heroux and J. Shaw, *Phys. Lett.* 13, 229 (1964).
4. J. A. R. Samson, Techniques of Vacuum Ultraviolet Spectroscopy (John Wiley & Sons, New York, 1967).
5. M. C. Hutley, Diffraction Gratings (Academic Press, New York, 1982).
6. D. J. Pegg in Methods of Experimental Physics, edited by P. Richard (Academic Press, New York, 1980), Vol. 17, pp. 529-606.
7. H. G. Berry, *Rep. Prog. Phys.* 40, 155 (1977).
8. B. C. Fawcett in Advances in Atomic and Molecular Physics (Academic Press, New York, 1974), Vol. 10, pp. 223-293.
9. L. J. Curtis, H. G. Berry and J. Bromander, *Phys. Scr.* 2, 216 (1970).
10. L. Kay, *Phys. Scr.* 5, 139 (1972).
11. H. J. Andra, in Progress in Atomic Spectroscopy, edited by W. Hanle and H. Kleinpoppen (Plenum Press, New York, 1978), Part B, pp. 829-953.
12. L. C. Northcliffe and R. F. Schilling, *Nucl. Data Tables* A7, 233-463 (1970).
13. J. D. Stoner, Jr. and L. J. Radziemski, Jr., *Nucl. Instrum. Methods* 90, 275 (1970).
14. J. B. Marion and F. C. Young, Nuclear Reaction Analysis - Graphs and Tables (North-Holland, Amsterdam, 1968).
15. V. S. Nikolaev and I. S. Dmitriev, *Phys. Lett.* 28A, 277 (1968).
16. H. D. Betz in Applied Atomic Collision Physics - Condensed Matter, edited by S. Datz (Academic Press, New York, 1983), Vol. 4, pp. 1-42.
17. J. Davidson and W. S. Bickel, *Nucl. Instrum. Methods* 110, 253 (1973).
18. L. J. Curtis, in Beam-Foil Spectroscopy, edited by S. Bashkin (Springer-Verlag, New York, 1976), pp. 63-109.

19. L. Kay, Phys. Lett. 5, 36 (1963).
20. I. Martinson and A. Gaupp, Phys. Rep. 15, 113 (1974).
21. I. Martinson, in Atomic Physics of Highly Ionized Atoms, edited by R. Marrus (Plenum Press, New York, 1983), pp. 1-47.
22. D. J. G. Irwin, A. E. Livingston and J. A. Kernahan, Nucl. Instrum. Methods 110, 105 (1973).
23. D. J. G. Irwin, A. E. Livingston and J. A. Kernahan, Can. J. Phys. 51, 1948 (1973).
24. J. A. Kernahan, K. E. Donnelly and E. H. Pinnington, Can. J. Phys. 55, 1310 (1977).
25. J. P. Buchet and M. Druetta, J. Opt. Soc. Am. 65, 991 (1975).
26. S. Bashkin, R. K. Wangness and L. Heroux, Phys. Rev. 151, 87 (1966).
27. A. E. Livingston, J. E. Hardis, L. J. Curtis, R. L. Brooks and H. G. Berry, Phys. Rev. A 30, 2089 (1984).
28. J. E. Hardis, H. G. Berry, L. J. Curtis and A. E. Livingston, Phys. Scr. 30, 189 (1984).
29. L. Barrette, E. J. Knystautas and R. Drouin, Nucl. Instrum. Methods 110, 29 (1973).
30. L. Barrette and R. Drouin, Phys. Scr. 10, 213 (1974).
31. L. Barrette, D. J. G. Irwin and R. Drouin, Phys. Scr. 12, 113 (1975).
32. J. Buchet, M. C. Buchet-Poulizac, G. Do Cao and J. Desesquelles, Nucl. Instrum. Methods 110, 19 (1973).
33. J. P. Buchet, A. Denis, J. Desesquelles, M. Druetta and J. L. Subtil, in Beam-Foil Spectroscopy edited by I. A. Sellin and D. J. Pegg (Plenum Press, New York, 1976), Vol. I, pp. 355-365.
34. A. E. Livingston, E. H. Pinnington, D. J. G. Irwin, J. A. Kernahan and R. L. Brooks, J. Opt. Soc. Am. 71, 442 (1981).
35. H. G. Berry, J. Desesquelles, P. Tryon, P. Schnur and G. Gabrielse, Phys. Rev. A 14, 1457 (1976).
36. H. G. Berry and C. H. Batson in Beam-Foil Spectroscopy edited by I. A. Sellin and D. J. Pegg (Plenum Press, New York, 1976), Vol. I, pp. 367-375.

37. H. G. Berry, J. Desesquelles, K. T. Cheng and R. M. Schechtman, Phys. Rev. A 18, 546 (1978).
38. M. C. Buchet-Poulizac and J. P. Buchet, Phys. Scr. 27, 99 (1983).
39. J. P. Buchet, M. C. Buchet-Poulizac, A. Denis, J. Desesquelles and G. Do Cao, Phys. Scr. 9, 221 (1974).
40. J. Rothermel, H. D. Betz, F. Bell and V. Zacek, Nucl. Instrum. Methods 194, 341 (1982).
41. J. Bromander, Nucl. Instrum. Methods 110, 11 (1973).
42. S. Bashkin, E. Trabert, P. H. Heckmann, H. v. Buttler and K. Brand, Phys. Scr. 28, 193 (1983).
43. Minuteman Laboratories, Inc. Action, MA.
44. J. B. Nicholson, Adv. X-Ray Anal. 8, 301 (1964).
45. H. A. Rowland, Phil. Mag. 13, 469 (1882).
46. J. E. Mack, J. R. Stehn and B. Edlen, J. Opt. Soc. Am. 22, 245 (1952).
47. H. G. Beutler, J. Opt. Soc. Am. 35, 311 (1945).
48. T. Namioka, J. Opt. Soc. Am. 51, 4 (1961).
49. J. R. Cuthill, in X-Ray Spectroscopy, edited by L. V. Azaroff (McGraw-Hill, New York, 1974), pp. 133-172.
50. S. P. Davis, Diffraction Grating Spectrographs (Holt, Rhinehart and Winston, New York, 1970).
51. B. Bandong, private communication.
52. A. A. Sterk, Adv. X-Ray Anal. 9, 410 (1966).
53. J. E. Manson Co., Inc., Concord, MA.
54. A. Strasheim and M. P. Brandt, Spectro. Chim. Acta 25B, 1 (1970).
55. G. L. Wiessler and R. W. Carlson, in Methods of Experimental Physics edited by L. Marton and C. Marton (Academic Press, New York, 1979), Vol. 14.
56. Leybold-Heraeus Vacuum Products Inc., Monroeville, PA.
57. For a description and example see A. Langenberg, R. L. Watson and J. R. White, J. Phys. B 13, 4193 (1980).

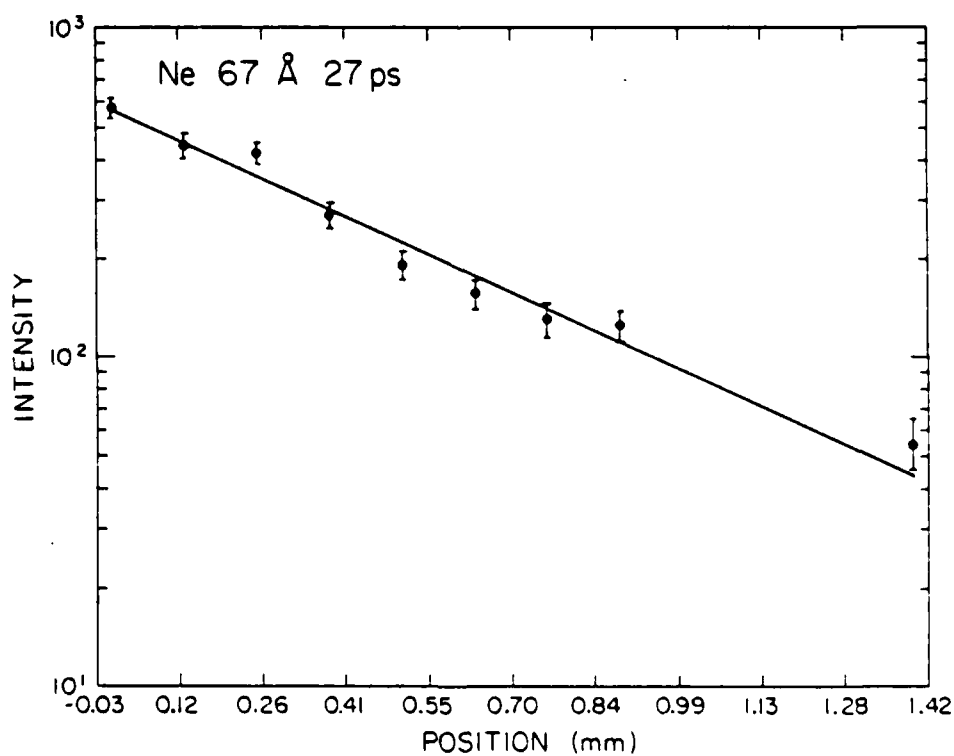
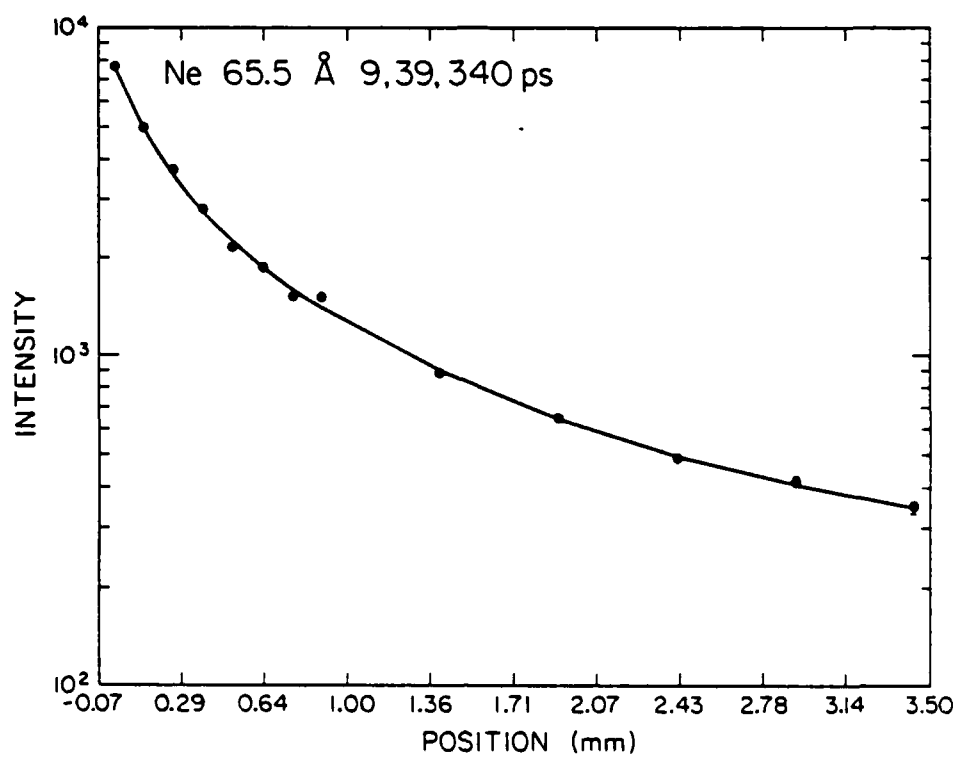
58. D. G. Smith and K. A. Pounds, IEEE Trans. Nucl. Sci. NS-15, 541 (1968).
59. J. G. Timothy and L. B. Lapson, Appl. Opt. 13, 1417 (1974).
60. L. B. Lapson and J. G. Timothy, Appl. Opt. 15, 1218 (1976).
61. J. E. Mack, F. Paresce and S. Bowyer, Appl. Opt. 15, 861 (1976).
62. J. P. McCau, J. Jamar and S. Gardier, IEEE Trans. Nucl. Sci. NS-23, 2049 (1976).
63. B. M. Johnson, K. W. Jones, D. C. Gregory, T. H. Kruse, and E. Trabert, Phys. Lett. 86A, 285 (1981).
64. T. H. Kruse, J. L. Cecchi, B. M. Johnson, D. C. Gregory and K. W. Jones, Phys. Lett. 90A, 284 (1982).
65. W. L. Hodge, B. C. Stratton and H. W. Moos, Rev. Sci. Instrum. 55, 16 (1984).
66. G. M. Lawrence and E. J. Stone, Rev. Sci. Instrum. 46, 432 (1975).
67. J. L. Wisa, P. R. Henkel and R. L. Roy, Rev. Sci. Instrum. 48, 1217 (1977).
68. M. Lampton and F. Paresce, Rev. Sci. Instrum. 45, 1098 (1974).
69. J. K. Swenson and D. Brandt, IEEE Trans. Nucl. Sci. NS-30, 1548 (1983).
70. B. M. Johnson, private communication.
71. G. W. Fraser, M. A. Barstow, J. E. Pearson, M. C. Whiteley and M. Lewis, Nucl. Instrum. Methods 224, 272 (1984).
72. J. G. Timothy, Space Sci. Instrum. 2, 289 (1976).
73. E. Trabert, Phys. Scr. T8, 112 (1984).
74. E. W. P. Bloemen, H. Winter, T. D. Mark, D. Dijkkamp, D. Barends and F. J. de Heer, J. Phys. B 14, 717 (1981).
75. R. C. Isler and R. A. Langley, Appl. Opt. 24, 254 (1985).
76. R. L. Kelly and L. J. Palumbo, "Atomic and Ionic Emission Lines Below 2000 Å: Hydrogen through Krypton", Oak Ridge National Laboratory Report ORNL-5922 (U.S. Government Printing Office, Washington D.C., 1982).
77. Y. Accad, C. L. Pekeris and B. Schiff, Phys. Rev. A 4, 516 (1971).

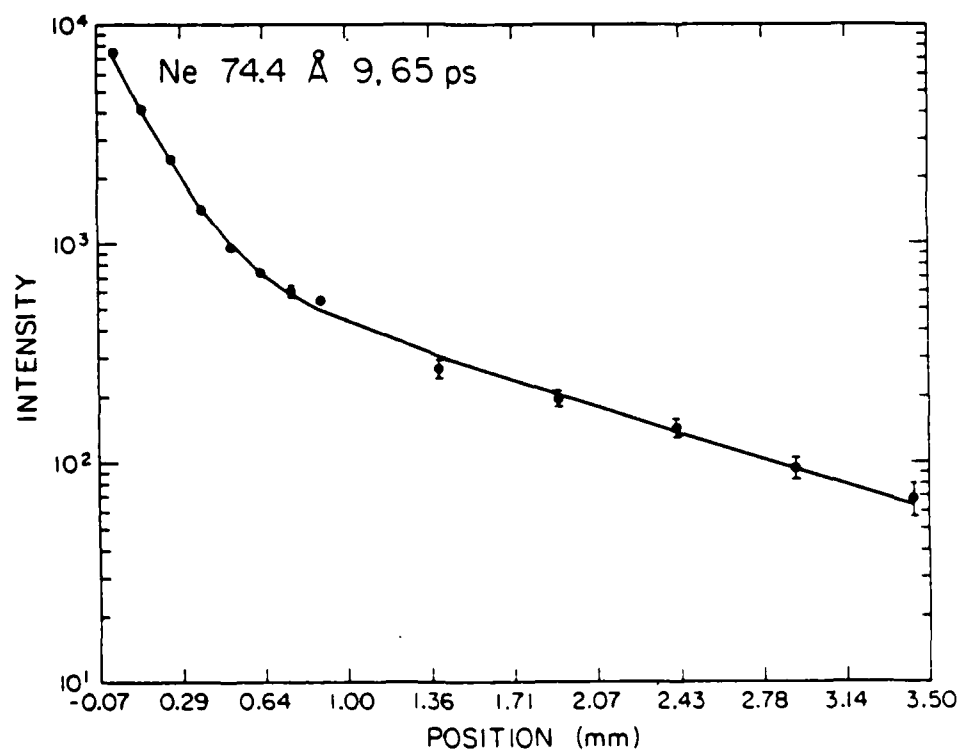
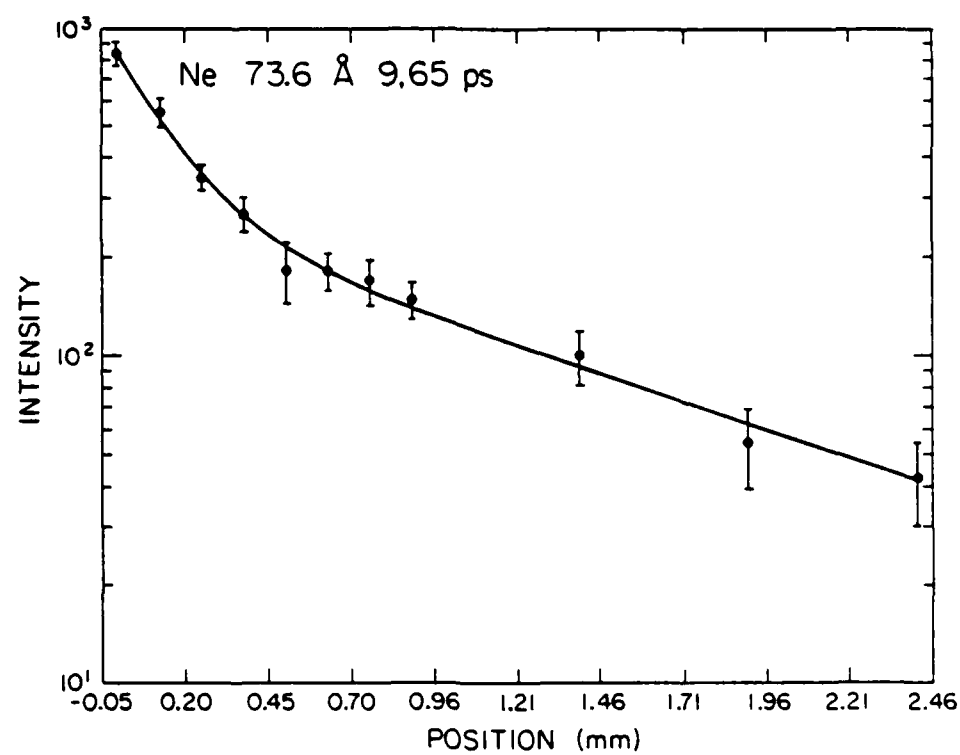
78. B. Edlen, Handbuch der Physik, edited by S. Flugge (Springer-Verlag, Berlin, 1964), Vol XXVII, p. 123.
79. E. H. Pinnington, R. N. Gosselin, J. A. O'Neill, J. A. Kernahan, D. E. Donnelly and R. L. Brooks, Phys. Scr. 20, 151 (1979).
80. L. Heroux, Phys. Rev. 153, 156 (1967).
81. S. Bashkin, J. de Phys. 40, CI-125 (1979).
82. D. J. G. Irwin and A. E. Livingston, Comput. Phys. Commun. 7, 95 (1974).
83. A. Lindgard and S. E. Nielson, Atomic and Nucl. Data Tables 19, 533 (1977).
84. K. Omidvar, Atomic and Nucl. Data Tables 28, 1 (1983).
85. H. G. Berry, J. Bromander, L. J. Curtis and R. Buchta, Phys. Scr. 3, 125 (1971).
86. S. M. Younger and W. L. Wiese, Phys. Rev. A 17, 1944 (1978).
87. B. Andresen, S. Hultberg, B. Jelenkovic, L. Liljeby, S. Mannervik and E. Veje, Z. Physik A 242, 101 (1979).
88. B. Andresen, B. Denne, J. O. Ekberg, L. Engstrom, S. Huldt and I. Martinson, Phys. Rev. A. 23, 479 (1981).
89. C. Jupen, B. Denne, J. O. Ekberg, L. Engstrom, V. Litzen, I. Martinson, W. Tai-Meng, A. Trigueiros and E. Veje, Phys. Rev. A 26, 2468 (1982).
90. H. D. Betz, D. Roschenthaler and J. Rothermel, Phys. Rev. Ltr. 50, 34 (1983).
91. A. Lindgard and E. Veje, Nucl. Instrum. Methods 202, 283 (1982).
92. K. Sato, M. Otsuka and M. Mimura, Appl. Opt. 23, 3336 (1984).
93. D. R. Bates and A. Damgaard, Phil. Trans. 242, 101 (1949).
94. W. L. Wiese, M. E. Smith and B. M. Glennon, Atomic Transition Probabilities (U.S. Government Printing Office, 1966) Vol. I, NBS-4.
95. C. W. Allen, Astrophysical Quantities, 2nd Ed. (The Athlone Press, London, 1963).
96. E. Biemont, Nucl. Instrum. Methods 202, 283 (1982).
97. W. J. Braithwaite, D. L. Mathews and C. F. Moore, Phys. Rev. A 11, 465 (1975).

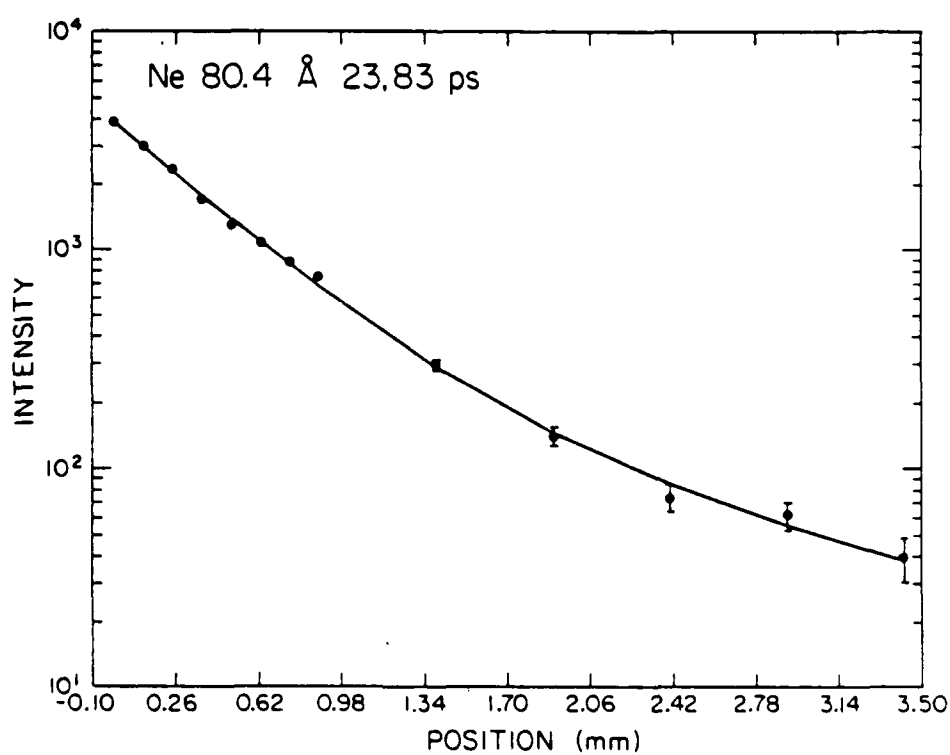
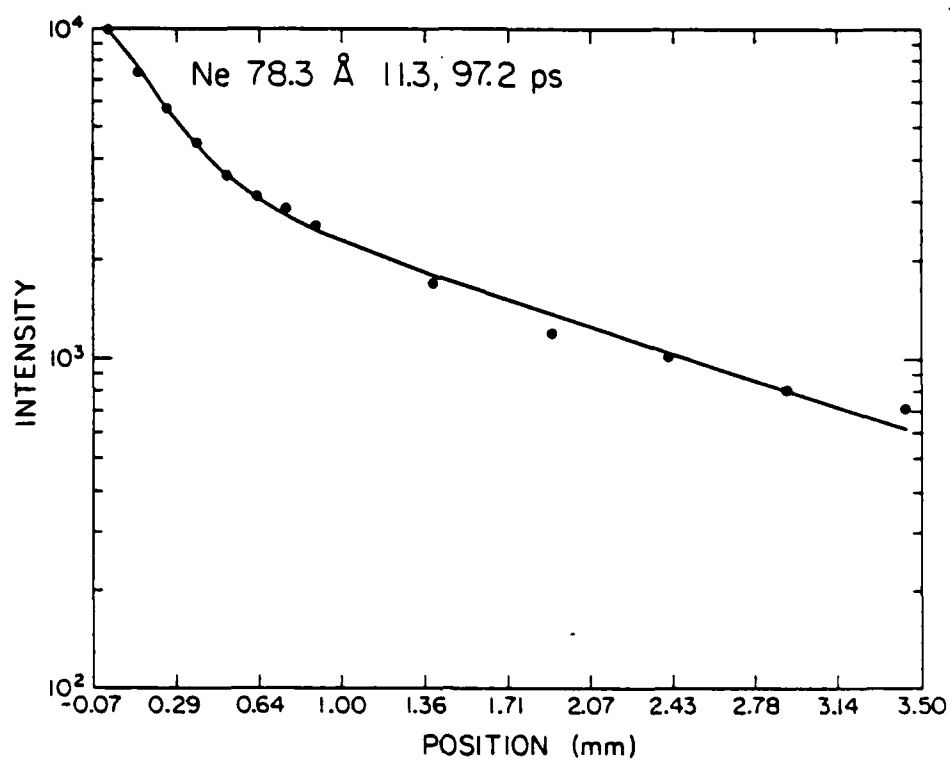
98. J. R. MacDonald, P. Richard, C. L. Cocke and M. Brown, *Phys. Rev. Lett.* 11, 684 (1973).
99. B. Andresen and E. Veje, *Phys. Rev. A* 16, 1980 (1977).
100. H. D. Betz, J. Rothermel, D. Roschenthaler, F. Bell R. Schuch and G. Nolte, *Phys. Lett.* 91A, 12 (1982).
101. R. L. Watson, J. R. White, A. Langenberg, R. A. Kenefick and C. C. Bahr, *Phys. Rev. A* 22, (1980).
102. S. Bashkin, H. Oona and E. Veje, *Phys. Rev. A* 25, 417 (1982).
103. L. Armstrong, Jr., in *Structure and Collisions of Ions and Atoms*, ed. by I. A. Sellin (Springer-Verlag, New York, 1978), p. 72.
104. O. Sinanoglu and W. Luken, *J. Chem. Phys.* 64, 4197 (1976).
105. B. C. Fawcett, *At. Data and Nucl. Data Tables* 16, 135 (1975).
106. J. P. Desclaux, *Comput. Phys. Commun.* 9, 31 (1975).
107. B. C. Fawcett, A. Ridgeley, and A. T. Paget, *J. Opt. Soc. Am.* 70, 1349 (1980).
108. B. Edlen, *Phys. Scr.* 20, 129 (1979); B. Edlen, *Phys. Scr.* 22, 593 (1981); B. Edlen, *Phys. Scr.* 28, 51 (1983); and B. Edlen, *Phys. Scr.* 28, 483 (1983).
109. K. T. Cheng, Y. K. Kim, and J. P. Desclaux, *At. Data and Nucl. Data Tables* 24, 111 (1979).
110. R. Glass, *Z. Physik A* 320, 545 (1985).
111. E. Trabert, P. H. Heckmann, and H. v. Buttler, *Z. Physik. A* 290, 7 (1979).
112. E. Trabert and P. H. Heckmann, *Phys. Scr.* 21, 146 (1980).
113. B. C. Fawcett, *At. Data and Nucl. Data Tables* 22, 473 (1978).
114. L. C. McIntyre, Jr., D. J. Donahue, and E. M. Bernstein, *Phys. Scr.* 17, 5 (1978).
115. E. Trabert, P. H. Heckmann, W. Schlagheck, and H. v. Buttler, *Phys. Scr.* 21, 27 (1980).
116. E. Trabert and P. H. Heckmann, *Phys. Scr.* 21, 35 (1980).
117. J. P. Forester, D. J. Pegg, P. M. Griffin, G. D. Alton, S. B. Elston, H. C. Hayden, R. S. Thoe, C. R. Vane, and J. J. Wright, *J. de Phys.* 40, C1-208 (1979).

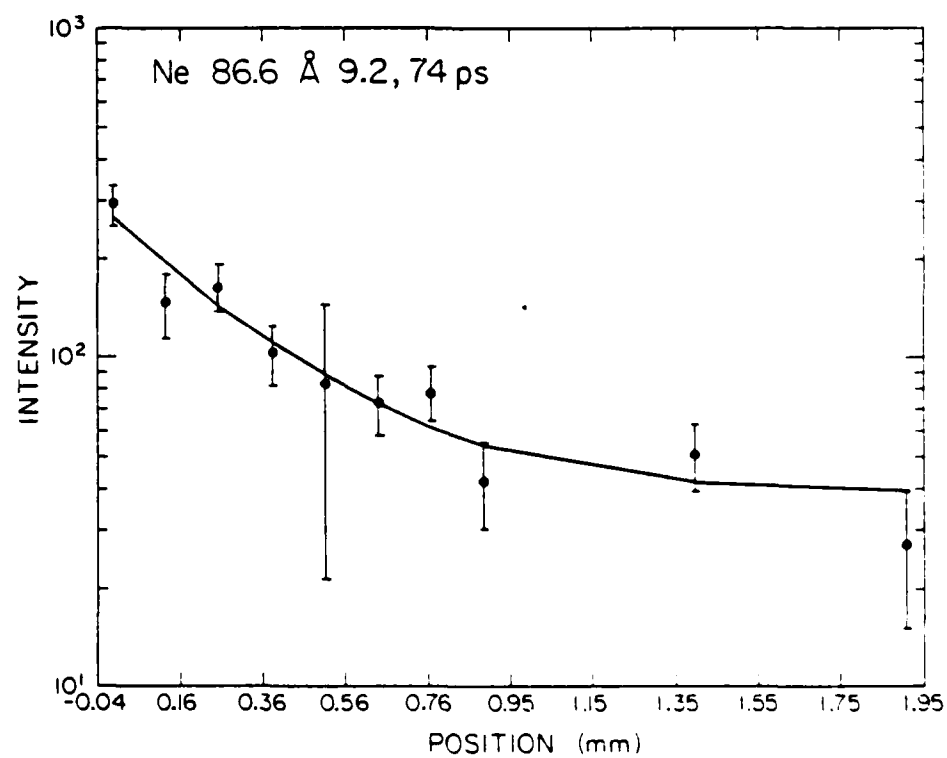
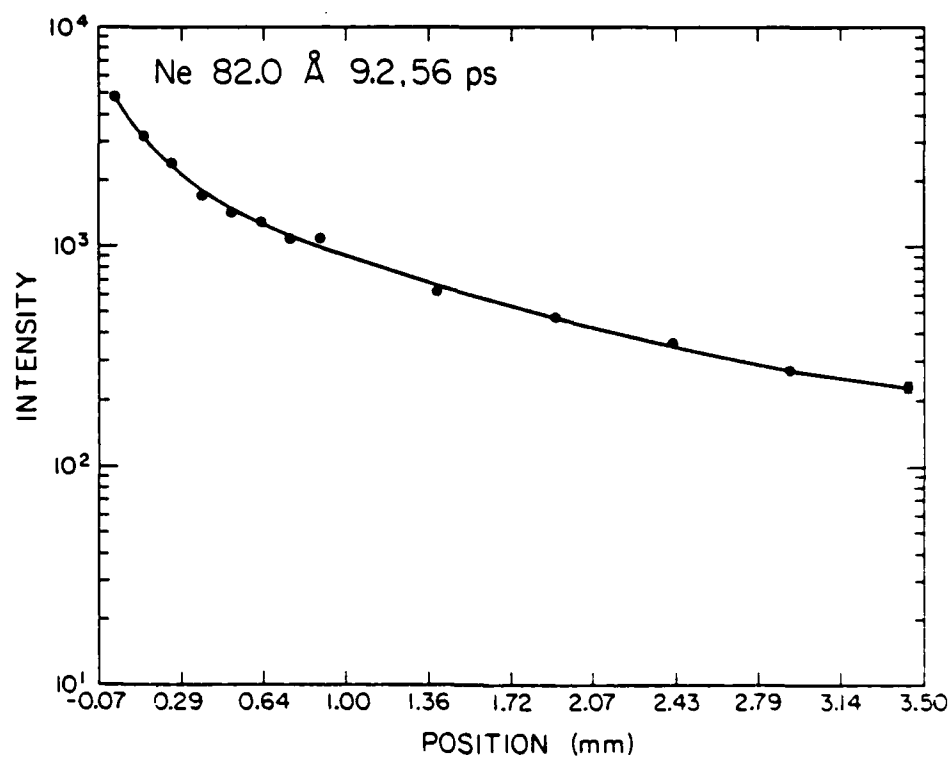
APPENDIX

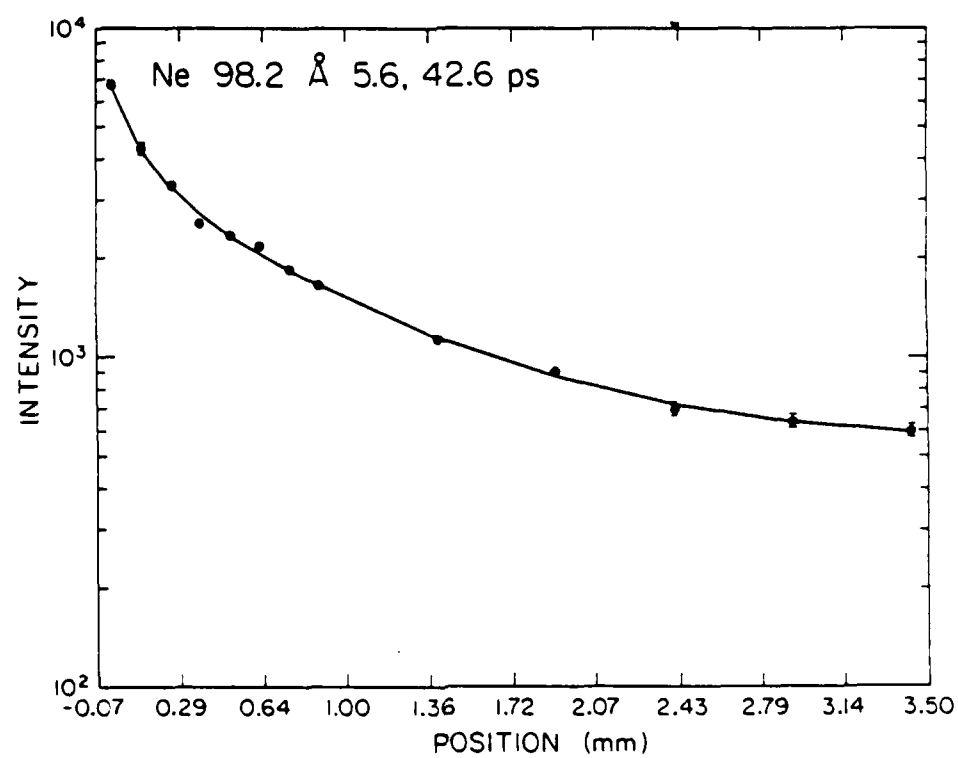
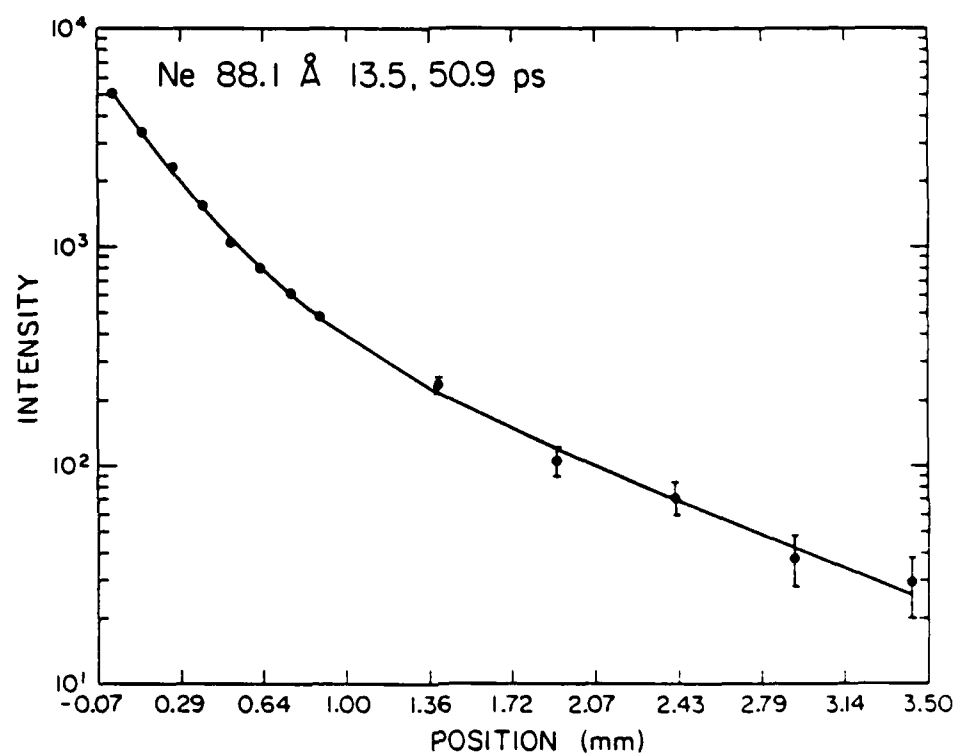
The following figures represent the lifetime measurements made on lines of neon and argon. The data are indicated by solid dots and a multiexponential fit to the data by the program Homer is shown as a line.

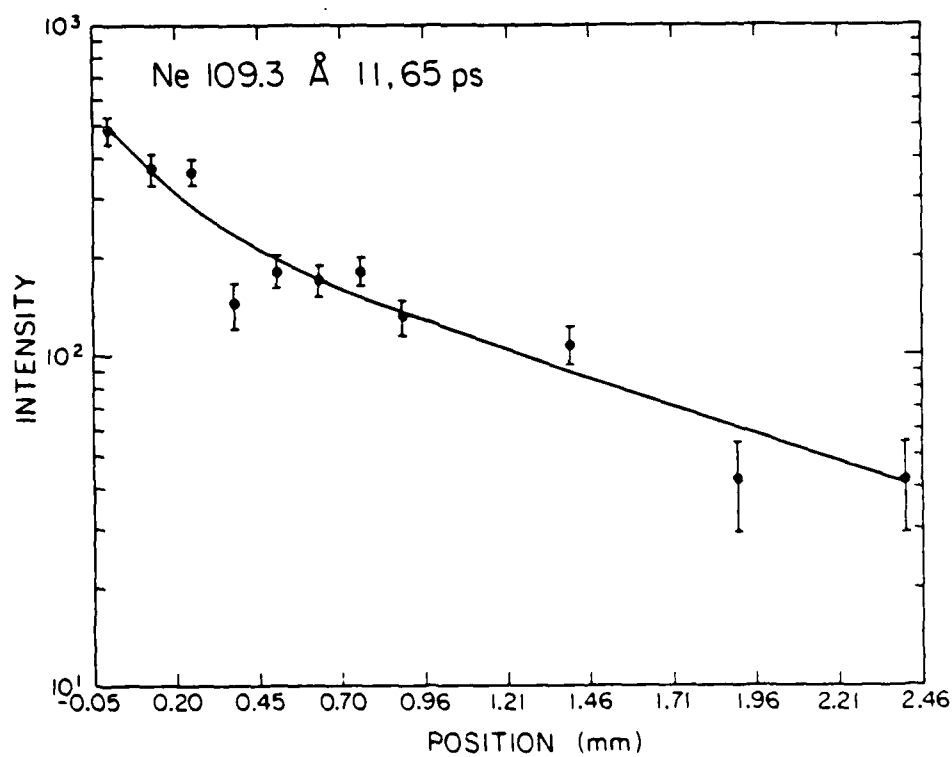
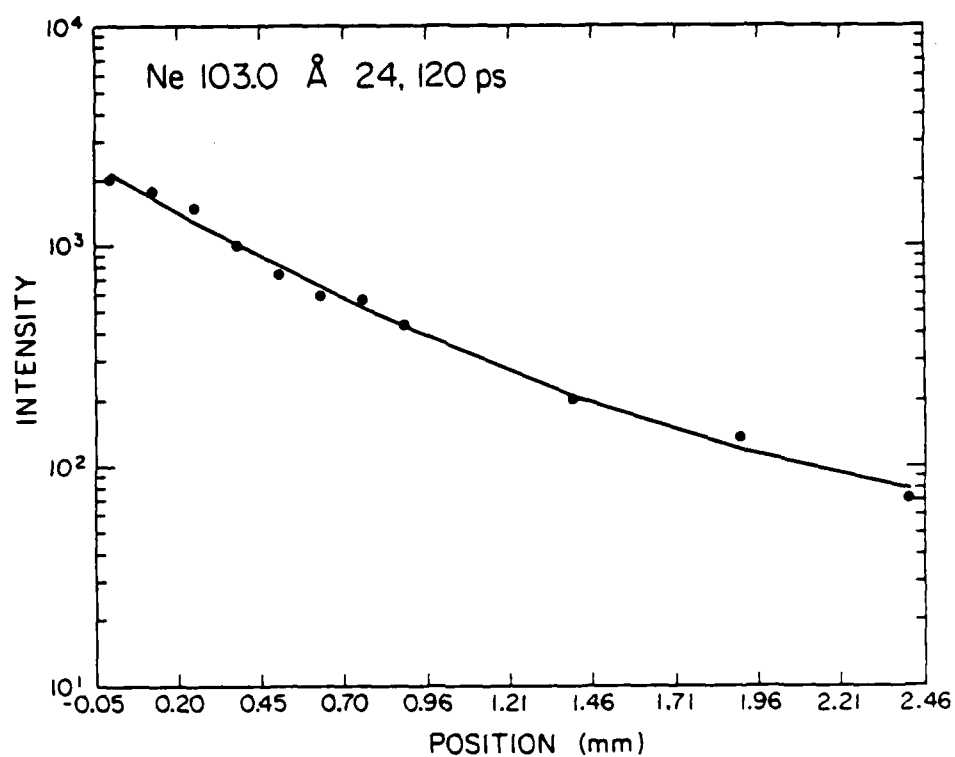


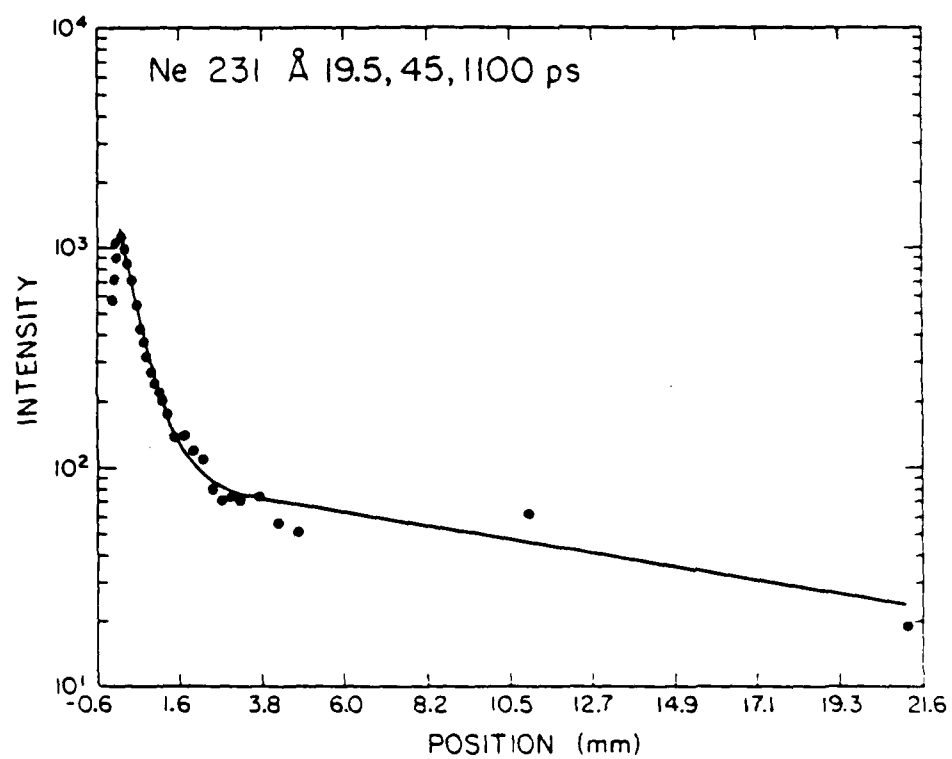


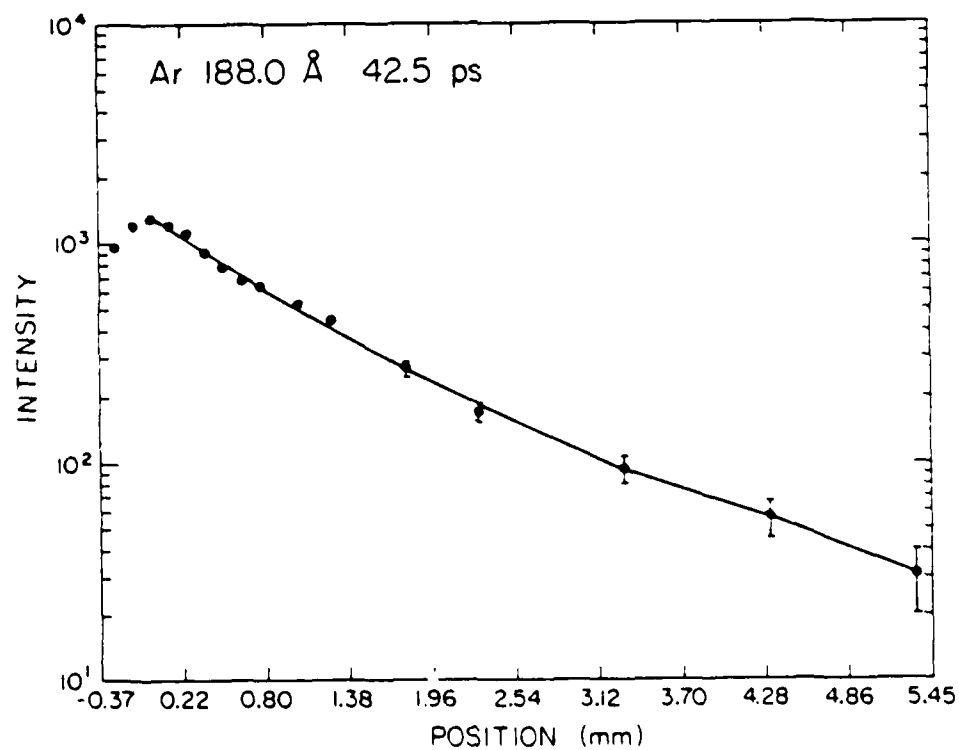
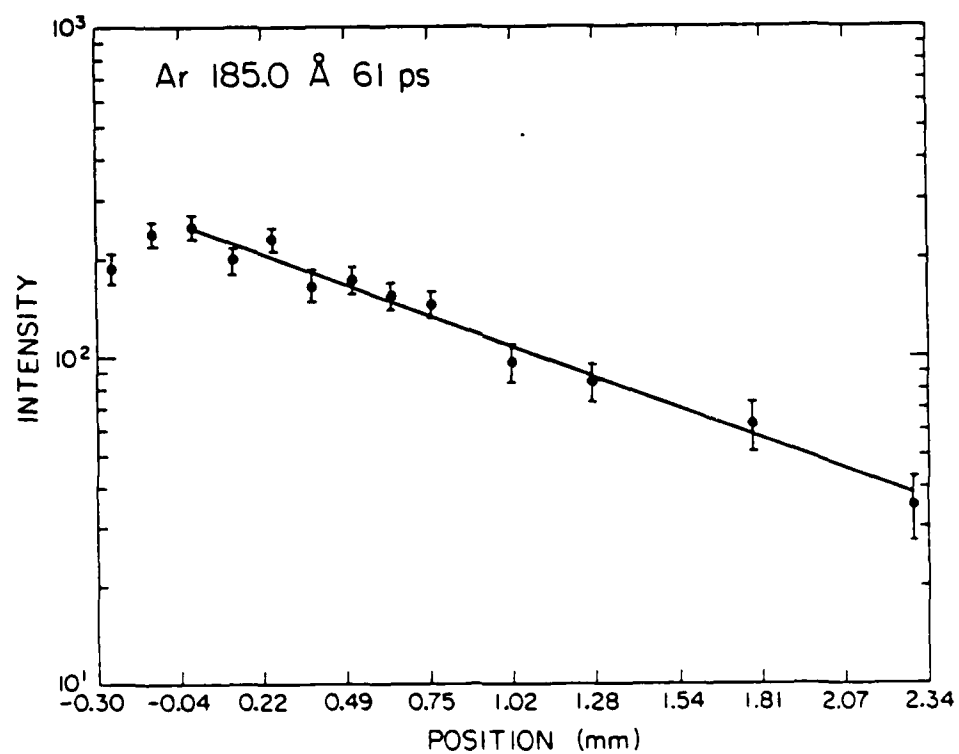


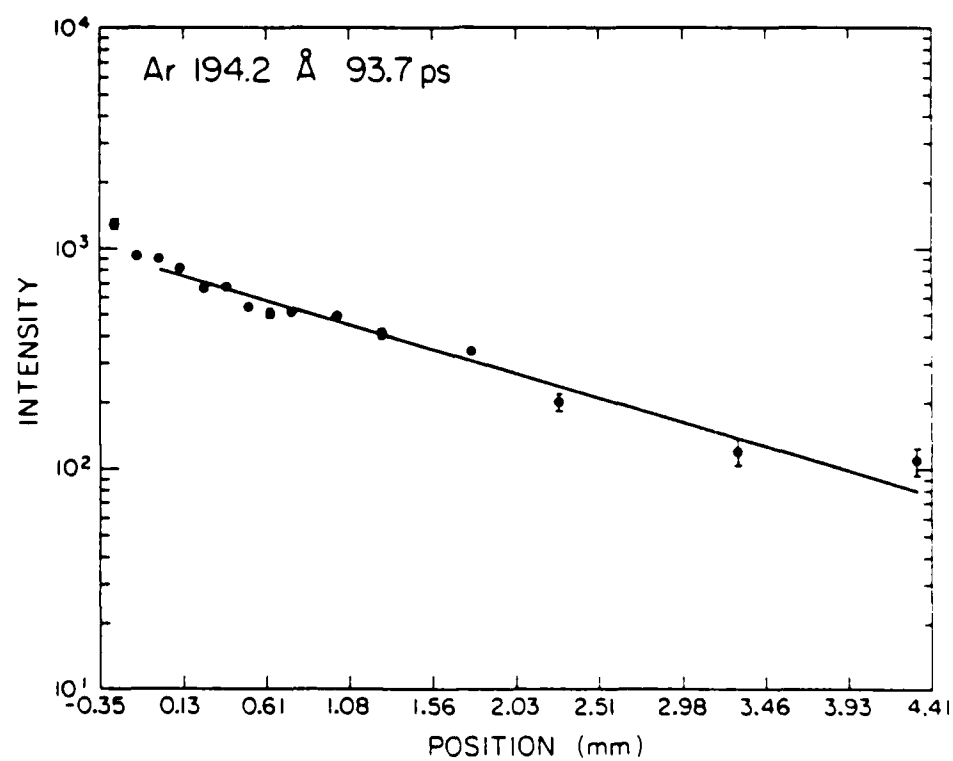
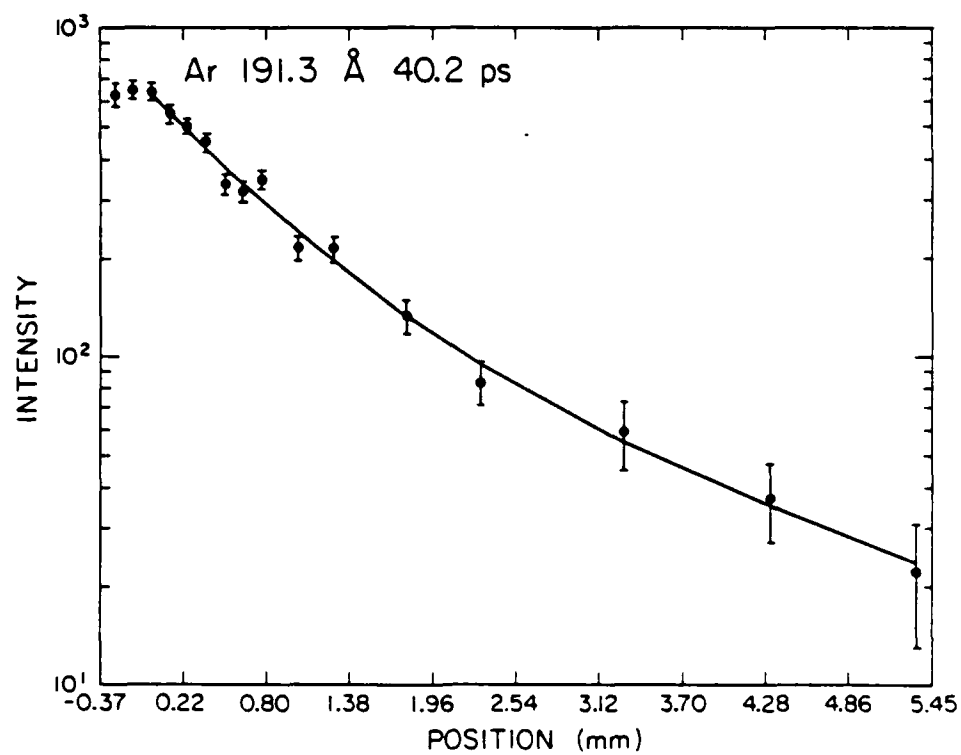


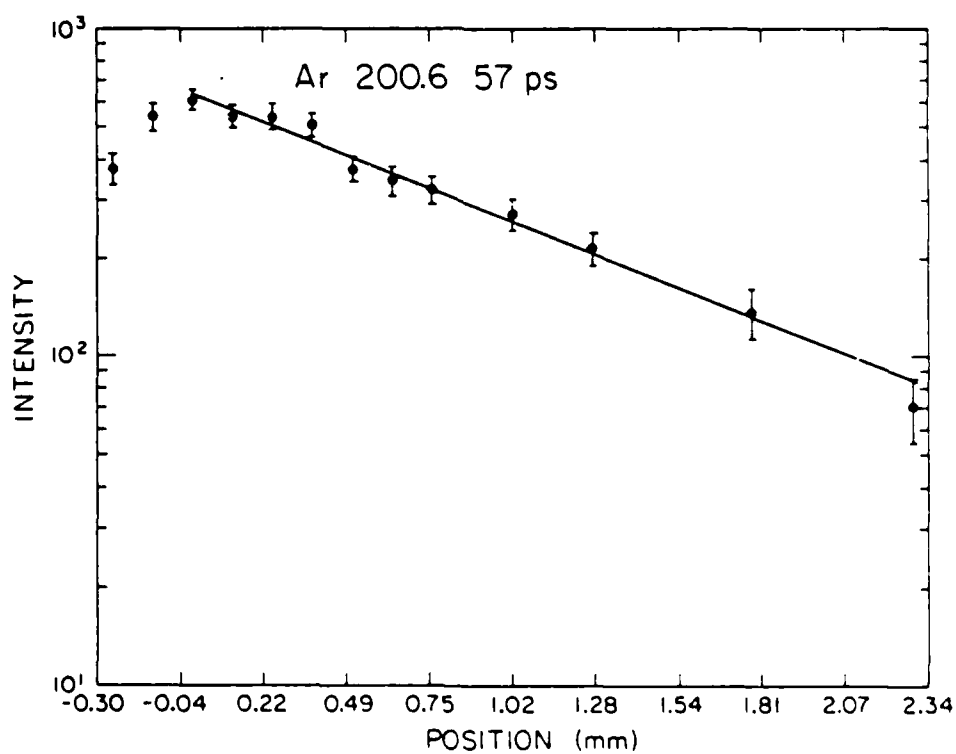
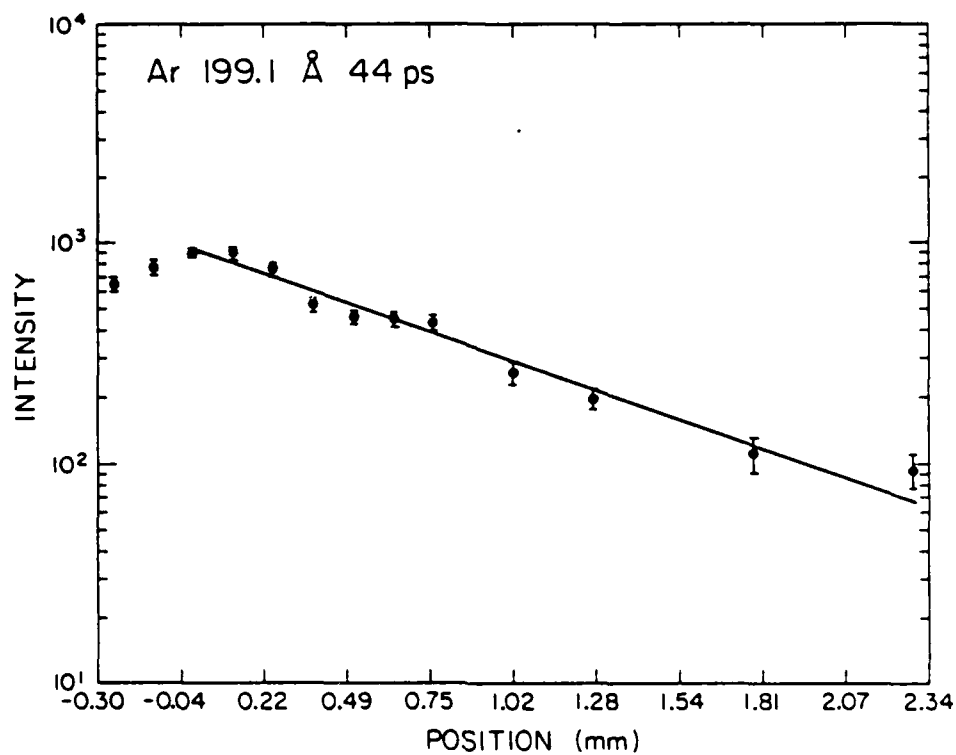


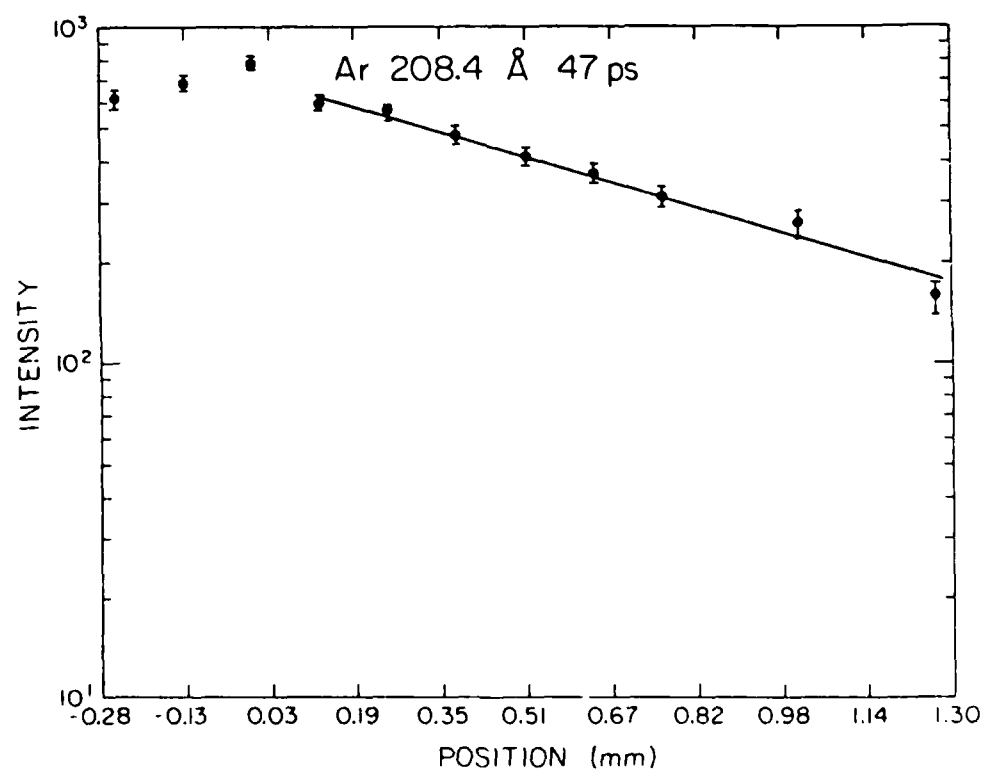
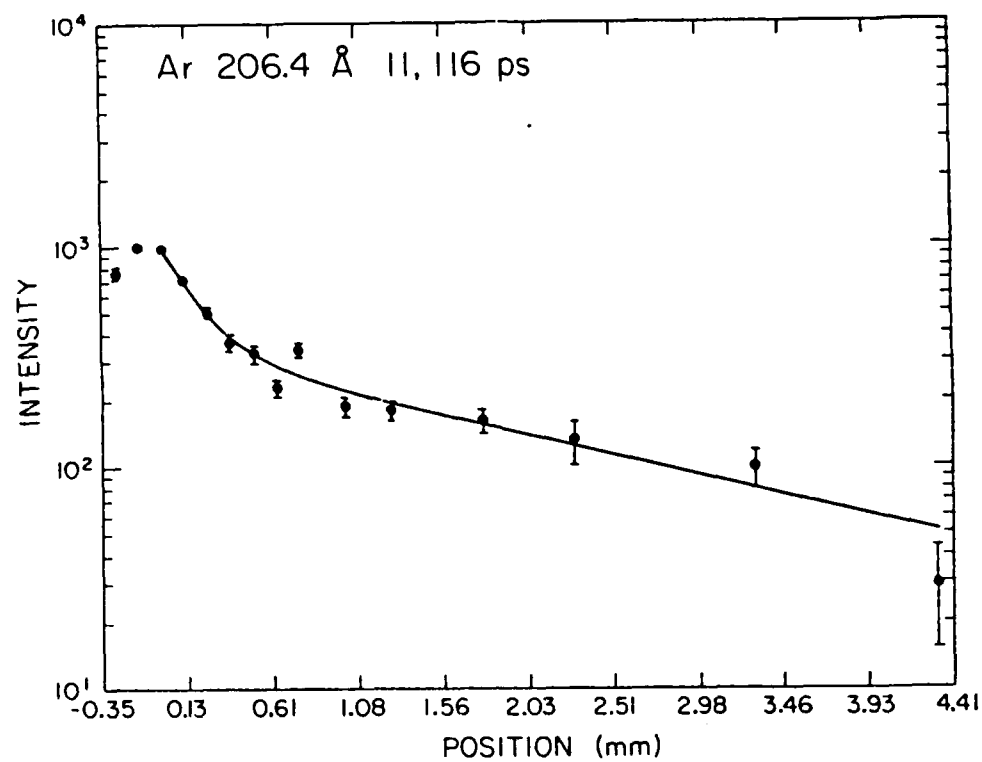


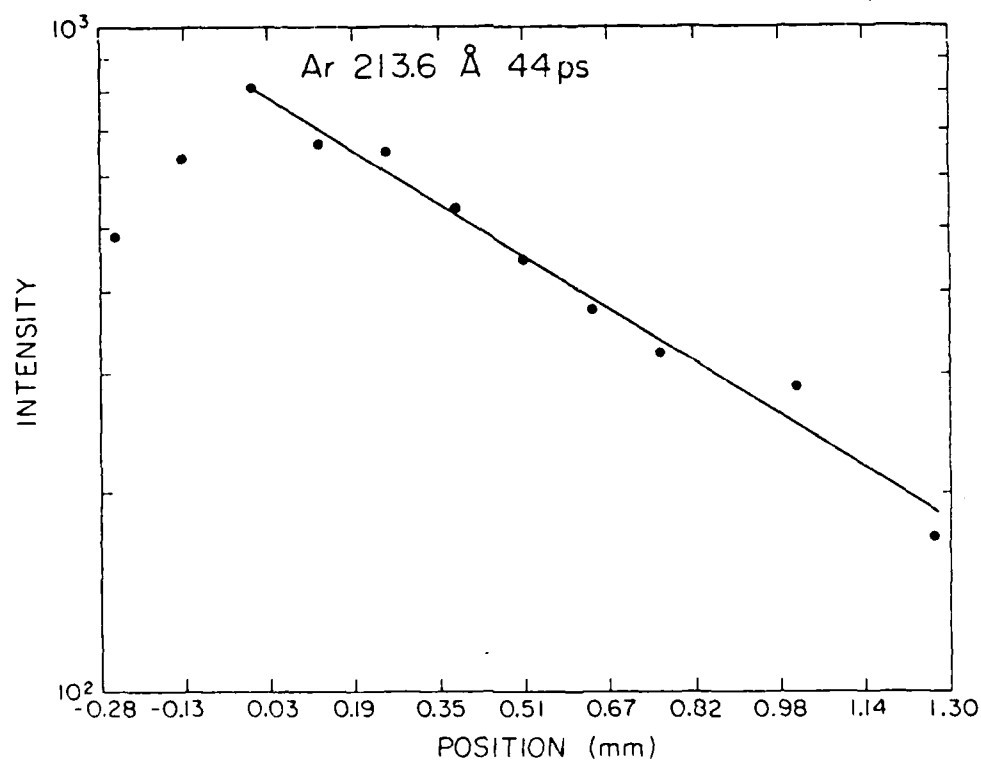
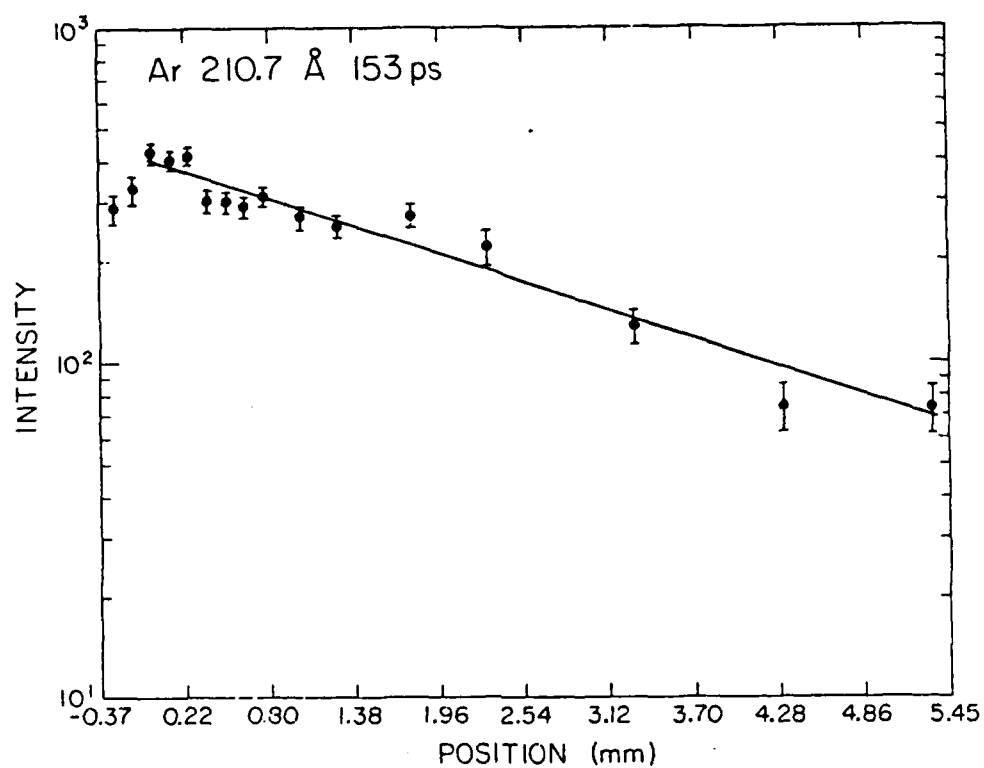


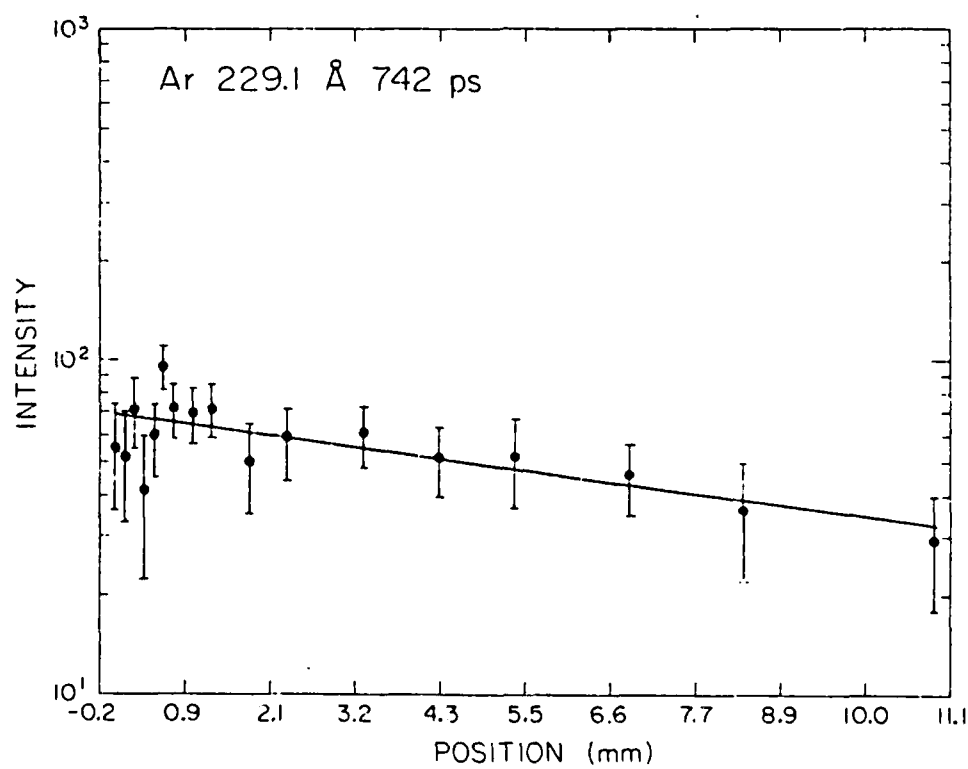
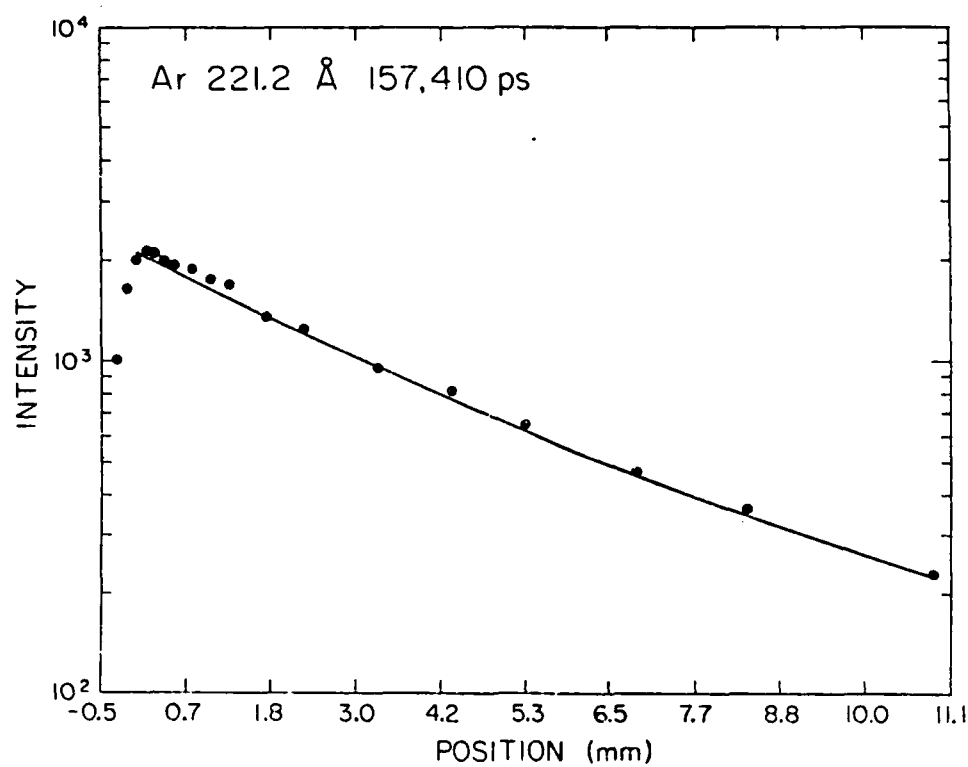


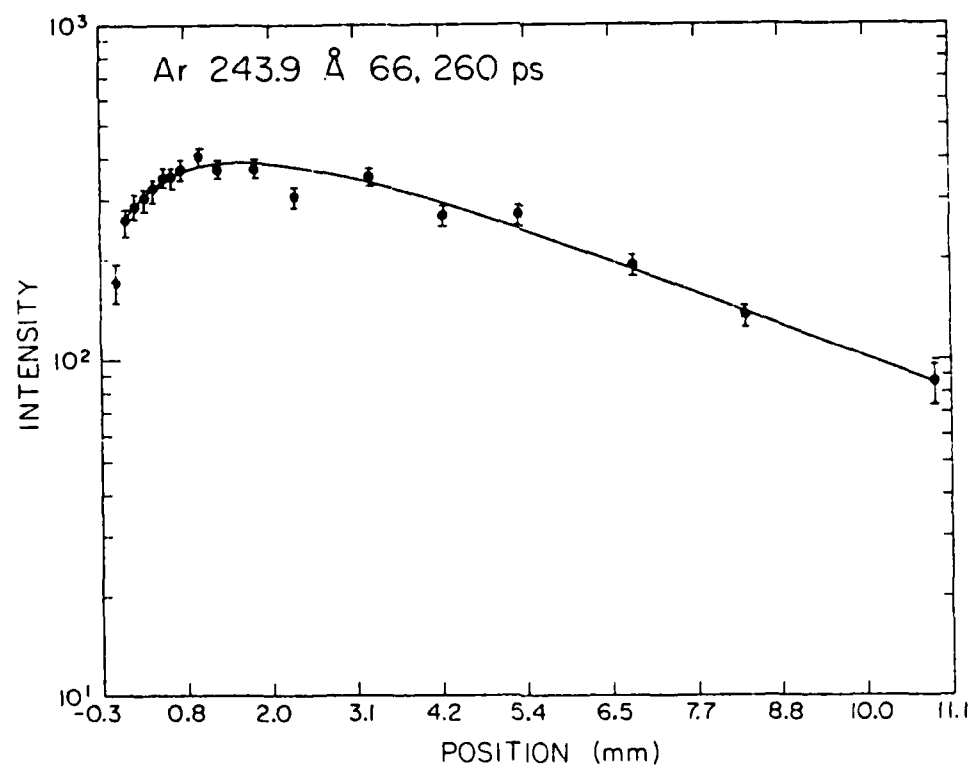
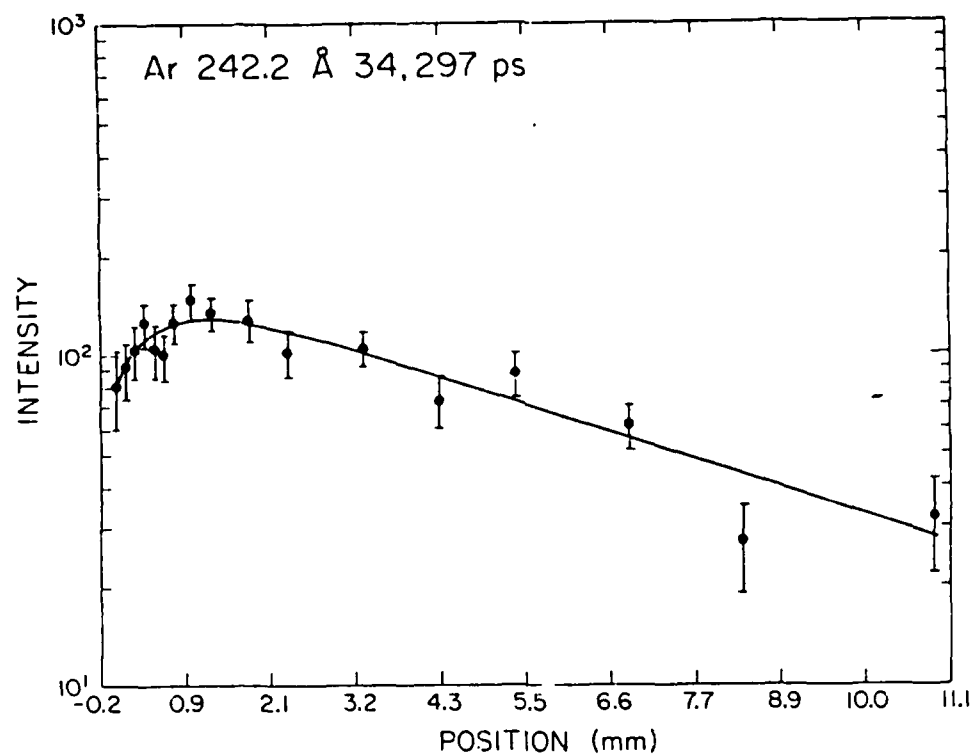


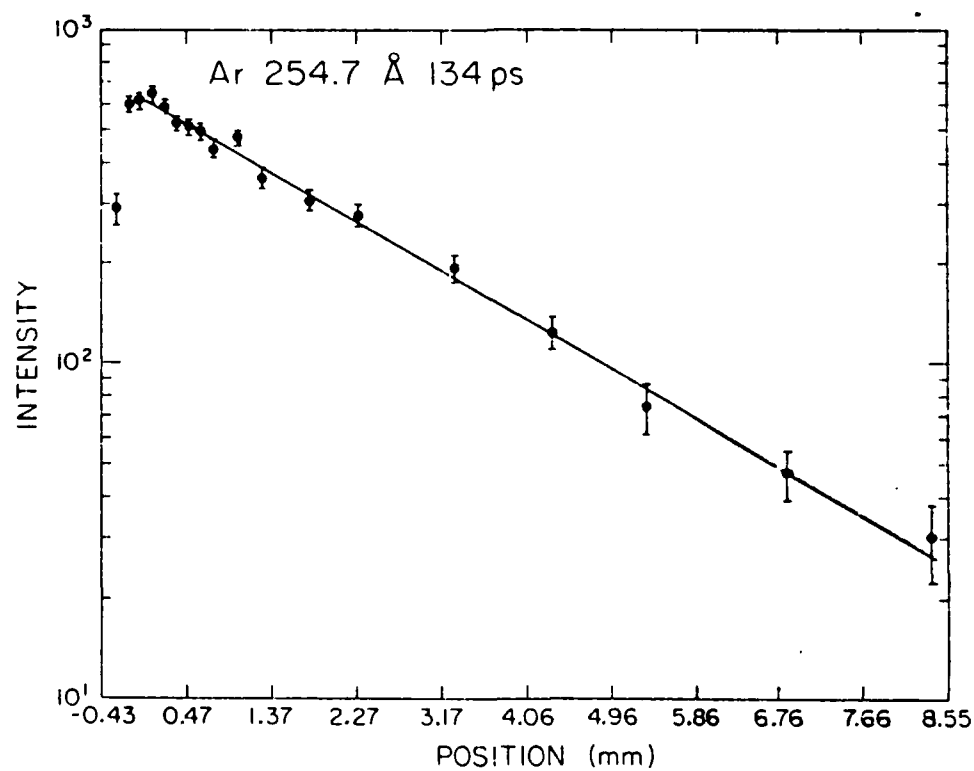
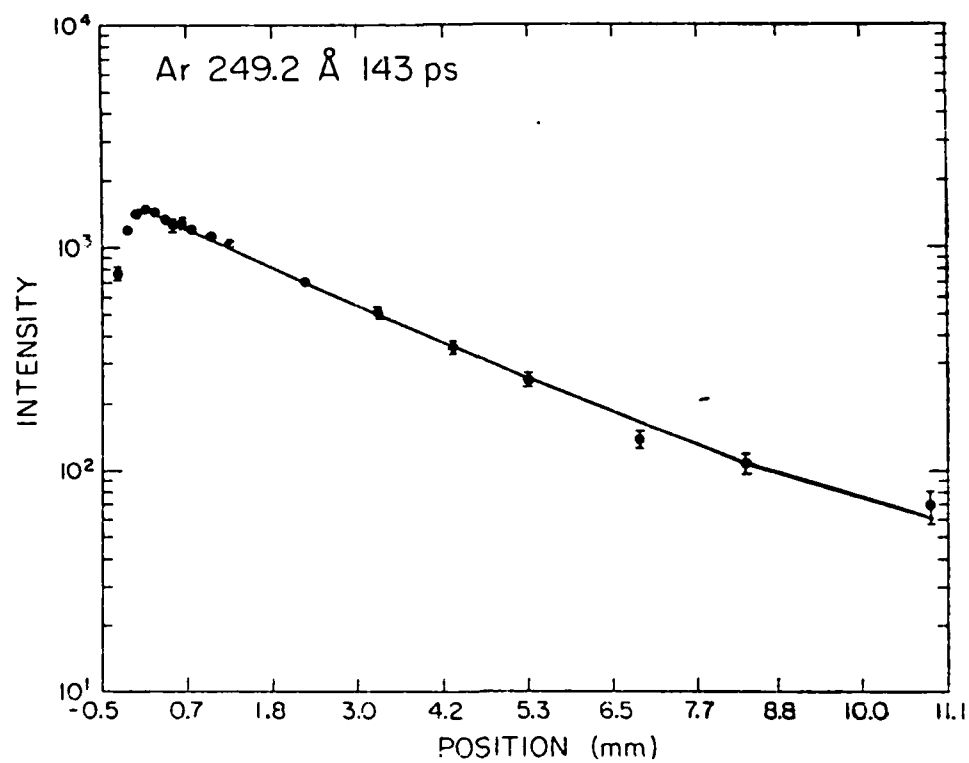


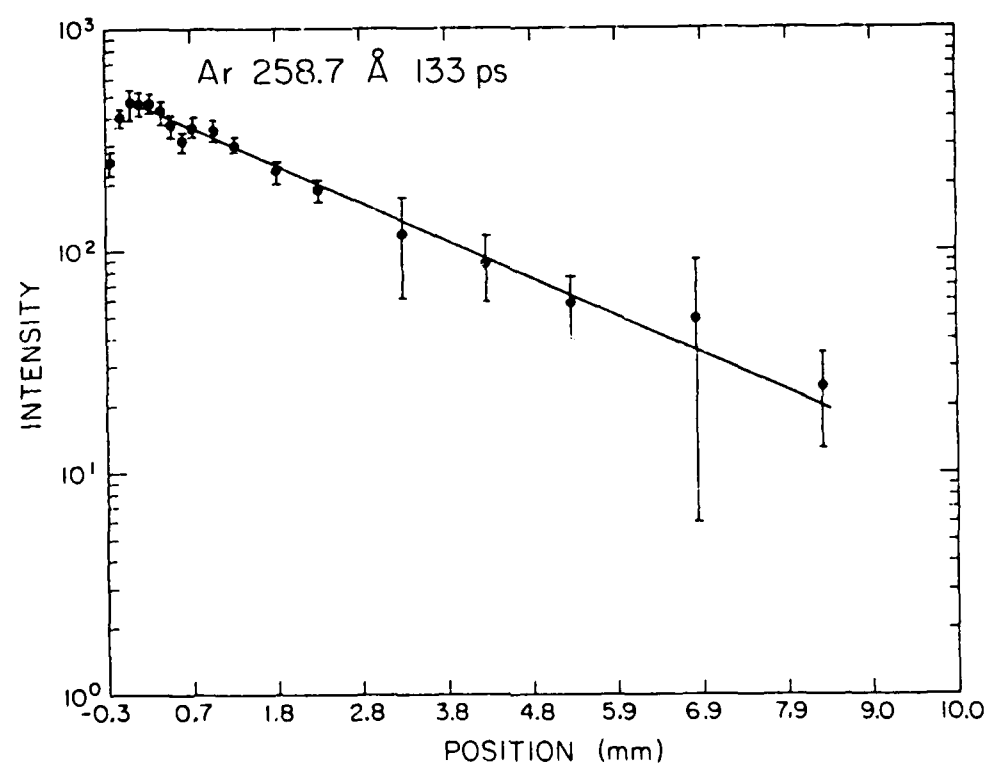
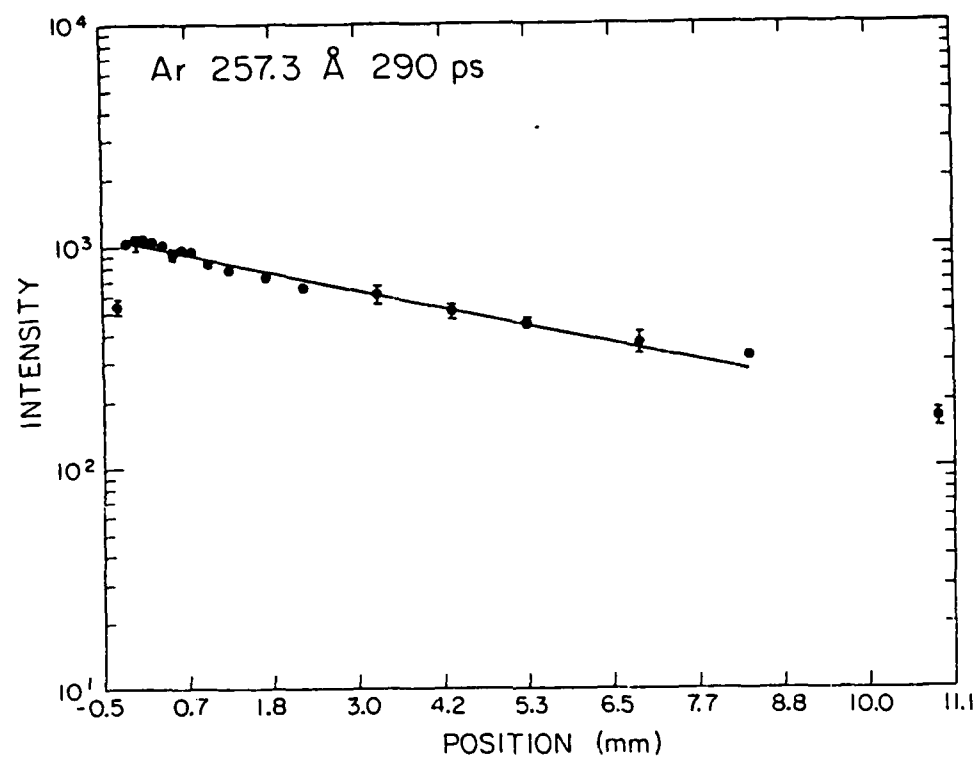


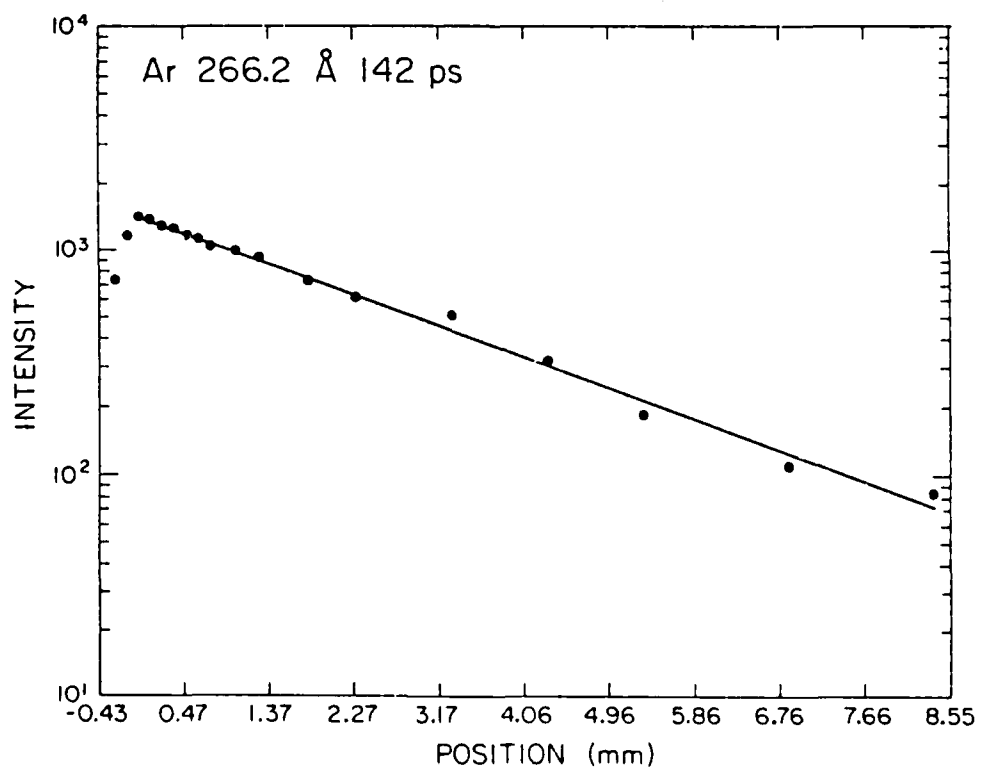
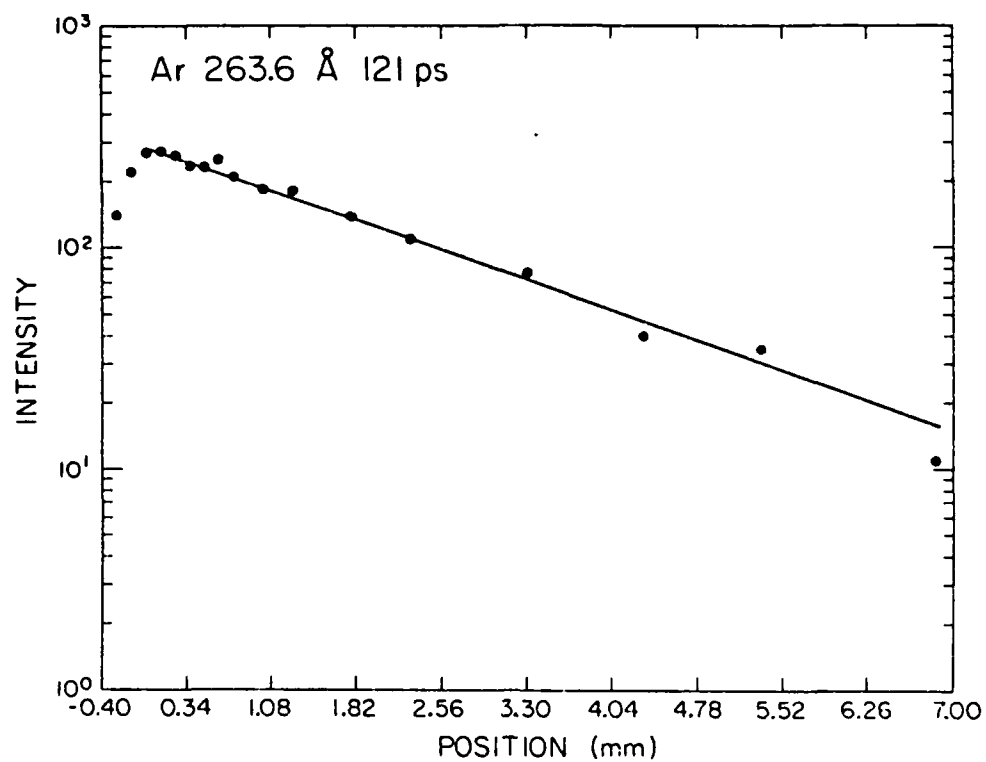


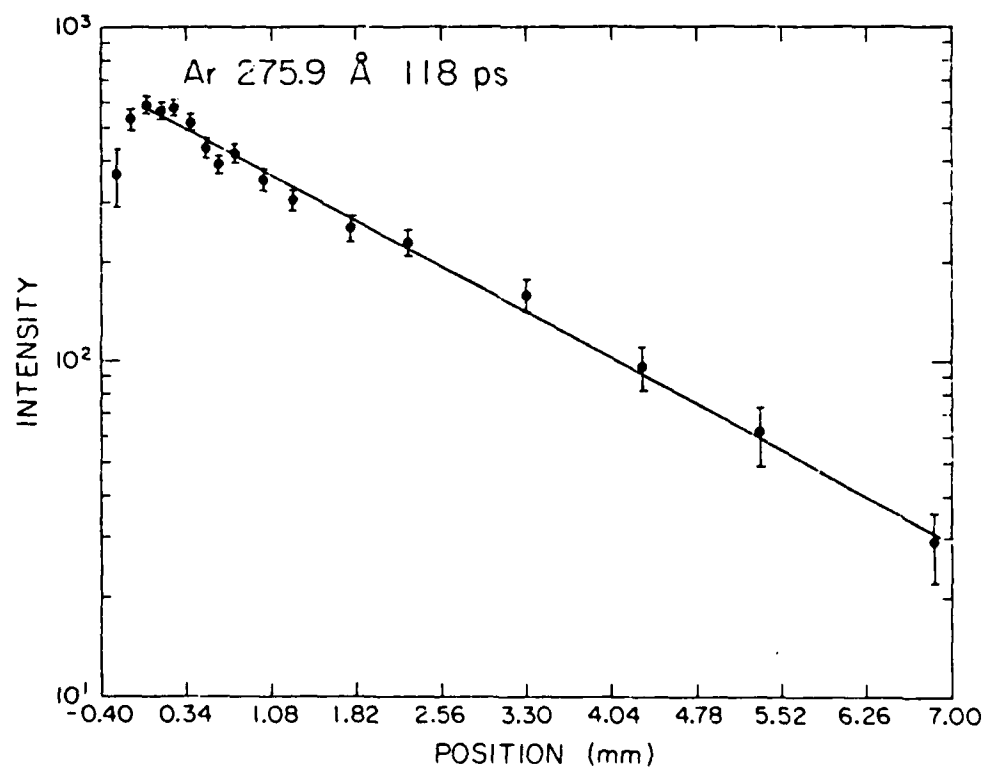
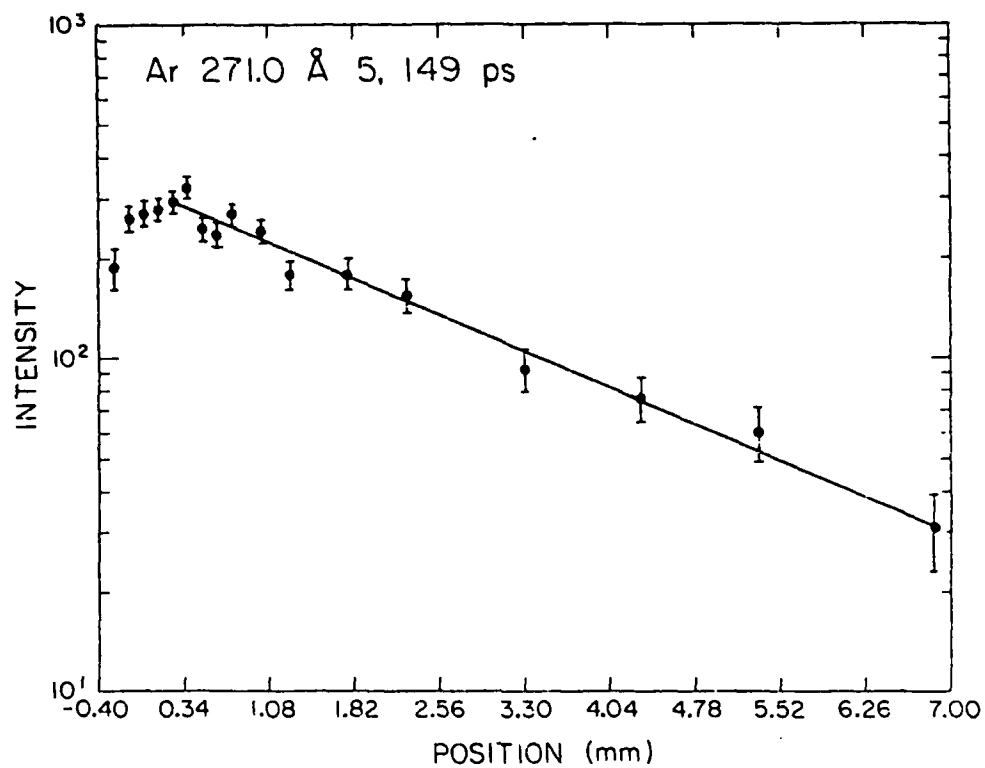


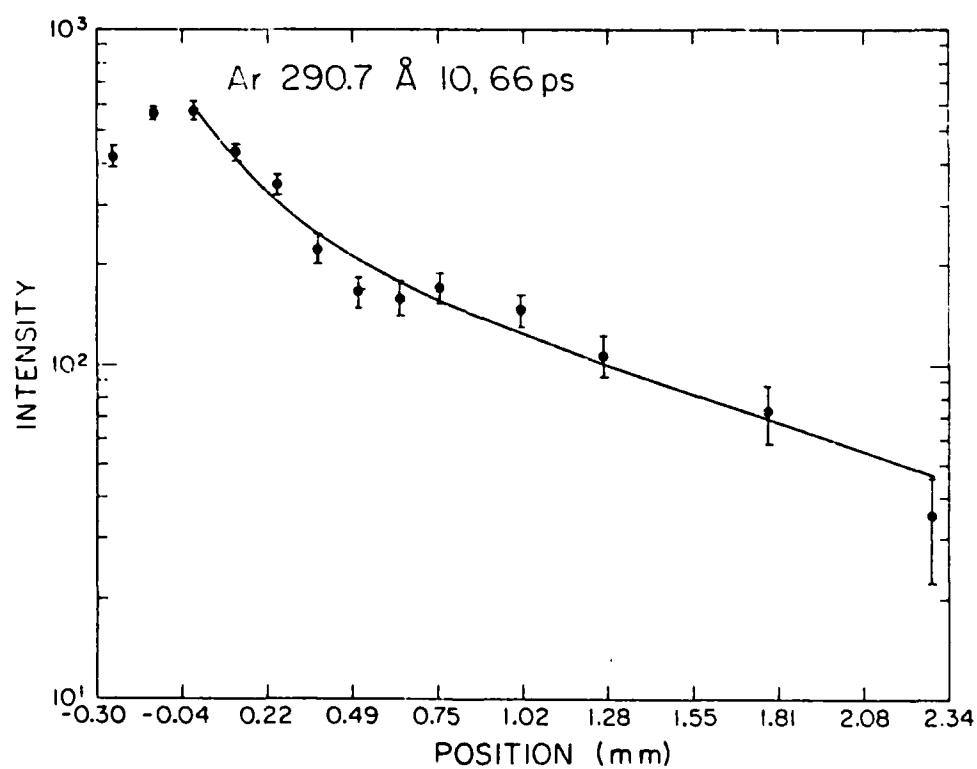
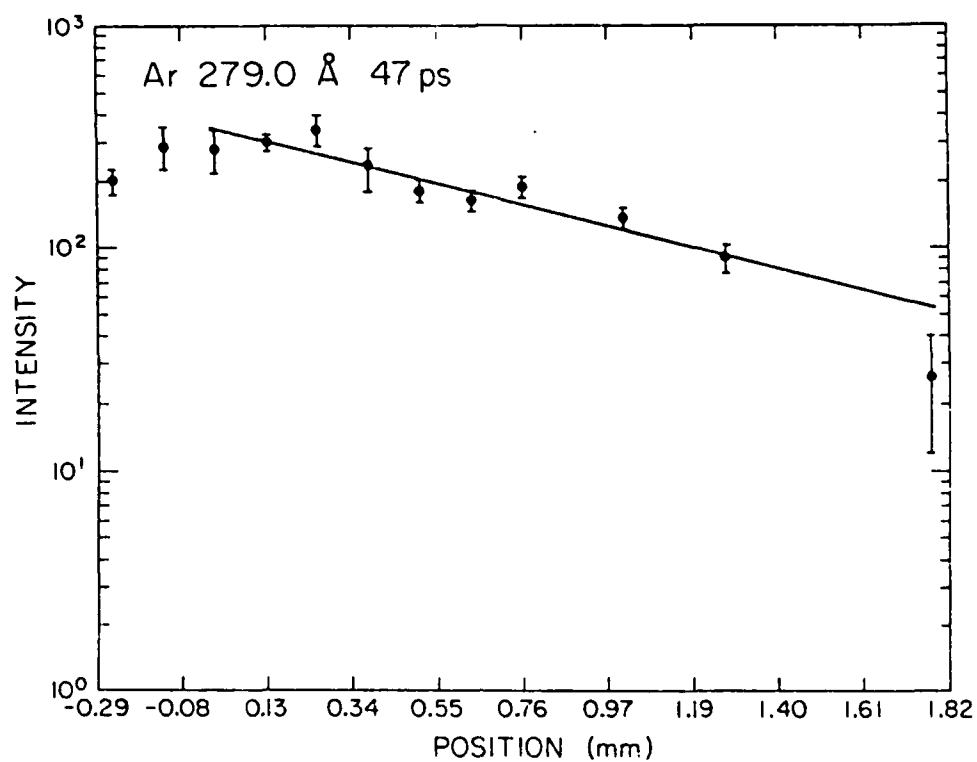












VITA

John Allen Demarest was born in East Chicago, Indiana on June 30, 1945 to Beatrice and Burdette Demarest. He later moved with his family to New Jersey. John graduated third in his class from James Caldwell High School. Upon graduation from Syracuse University in 1967 where he earned a B.S. degree in Chemical Engineering, he was commissioned an officer in the United States Air Force. A distinguished graduate from pilot training, he has flown four different tactical fighter aircraft. In 1971-1972 he flew missions over North and South Vietnam as an F-4E aircraft commander and flight commander.

He was selected in 1975 for an Air Force Institute of Technology (AFIT) program and graduated from Texas A&M University with a M.S. in Nuclear Chemistry. He became a member of the Phi Lambda Upsilon Chemical Honorary Society. In 1978 he was promoted to major and served as Section Chief, Advanced Weapons Concepts, coordinating programs of mutual interest to the Air Force and the DOE laboratories. In 1981, he graduated with an M.B.A. from New Mexico Highlands University.

He was again selected by AFIT for the present doctoral program in Nuclear Chemistry. In 1982, he was promoted to the rank of Lt Col. He was initiated into the Phi Kappa Phi Honor Society in April 1986.

Lt Col Demarest presently resides at 13327 Desert Flower NE, Albuquerque, N.M. with his wife, Teddy, and children, Tina and Stephen. As Deputy Chief, Advanced Technology Division of the Air Force Weapons Laboratory, he plans, budgets, and manages a multi-million dollar per year research program.

END

11-87

DTIC